ADVANCED FIBRE BRAGG GRATING FABRICATION SYSTEMS AND DEVICES

ANDREW MICHAEL GILLOOLY

Doctor of Philosophy

ASTON UNIVERSITY

November 2005

ASTON UNIVERSITY

ADVANCED FIBRE BRAGG GRATING FABRICATION SYSTEMS AND DEVICES

ANDREW MICHAEL GILLOOLY

Doctor of Philosophy

May 2005

This thesis address the creation of fibre Bragg grating based sensors and the fabrication systems which are used to manufacture them. The information is presented primarily with experimental evidence, backed up with the current theoretical concepts. The issues involved in fabricating high quality fibre Bragg gratings are systematically investigated. Sources of errors in the manufacturing processes are detected, analysed and reduced to allow higher quality gratings to be fabricated. The use of chirped Moiré gratings as distributed sensors is explored, the spatial resolution is increased beyond that of any previous work and the use of the gratings as distributed load sensors is also presented. Chirped fibre Bragg gratings are shown to be capable of operating as in-situ wear sensors, capable of accurately measuring the wear or erosion of the surface of a material. Two methods of measuring the wear are compared, giving a comparison between an expensive high resolution method and a cheap lower resolution method. The wear sensor is also shown to be capable of measuring the physical size and location of damage induced on the surface of a material. An array method is demonstrated to provide a high survivability such that the array may be damaged yet operate with minimal degradation in performance.

KEY WORDS

Bragg, grating, sensor, optical, fibre

Dedicated to the memory of Susan Mary Gillooly, Mum.

Acknowledgements

I would like to thank Aston University's Photonics Research Group and the Engineering and Physical Sciences Research Council (EPSRC) for funding the study of this PhD. In particular, I would like to thank Prof. L. Zhang who, as my supervisor, was always available to oversee the direction of study. The PhD studentship was supplemented by a CASE sponsorship from Indigo Photonics Ltd and at a later date by Insensys Ltd. My gratitude is extended to all of the team at Indigo Photonics, who warmly invited me into their work environment and treated me as an equal and to Insensys for their generosity in continuing the studentship. Special thanks must be given to Dr K. Sugden for taking the risk of inviting me into Indigo, Dr K. Chisholm who taught me invaluable techniques for fabricating FBGs and J. Mitchell for introducing me to the direct write system. Other people, who in one way or another, contributed towards this thesis include: S. Kieckbusch, F. Floreani, Dr T. Allsop, Dr X. Shu, Dr E. Turitsyna, Dr W. Zhang, Prof. M. Zervas, Dr K. Kalli and Dr M. Durkin. My final and warmest thanks are aimed towards H. Dobb who acted as my sounding board and emotional support during the write up stage of this thesis.

List of Contents

List of Figures

1

Thesis Overview

The contents of this thesis were studied over the telecommunication industry's most turbulent and troubling times. The late 1990's saw a dramatic rise is the industry which could not be sustained economically, subsequently the market crashed leaving thousands of people redundant worldwide and many technologies unfulfilled. The initial scope of this thesis was to help design and build world class fibre Bragg grating (FBG) fabrication systems which would allow the production of technically competitive FBGs for the telecoms industry whilst on placement with Indigo Photonics Ltd. However, the work was cut short due to the company becoming another casualty of the market crash. The direction of this thesis was consciously redirected towards FBG sensors, where a small commercial environment still existed.

Chapter two introduces the reader to the underlying theory surrounding the topic of fibre Bragg gratings. Attention is paid to the concepts behind fabricating FBGs where apodisation is discussed in detail.

Chapter three presents the work conducted, whilst on placement at Indigo Photonics Ltd. This work included the improvement of a scanning phase mask system, in order to improve the group delay characteristics of the Gires-Tournois Etalon (GTE) product. A direct write system was also worked on, improvements made and the versatility of the system demonstrated through the fabrication of a variety of gratings including chirped, arbitrarily apodised, superstructured and Moiré gratings.

The first sensor chapter, utilising a chirped FBG as a wear sensor, fills chapter four. This novel sensor is presented and thoroughly investigated. The use of chirped FBGs as well as uniform and apodised non-chirped FBGs are compared in order to give the best wear response from the sensor.

High spatial resolution Moiré sensors are demonstrated in chapter five. The sensors are formed from chirped Moiré FBGs with their temperature, strain and loading properties characterised. The temperature sensor is multiplexed with multiple Moiré sensors to gain a two-dimensional thermal profile of a soldering iron. The strain sensor is shown to be capable of measuring a uniform strain across the entire sensor or a strain gradient. For the first time Moiré gratings are used as quasi-distributed load sensors, giving a loading cross section of a weight.

Chapter six consists of an array structure designed to provide the user with a high survivability sensor array. The design is configured to allow sections of the array to be damaged, causing little or no effect to the array's ability to obtain information from the sensing elements. A numerical model is presented for the array and a financial justification for different configurations given.

Chapter seven concludes the thesis by reviewing the work presented within the thesis as a whole. Future work is considered and new avenues of research suggested.

2

Theory of Fibre Bragg Gratings

This chapter aims to give an overview of the properties of fibre Bragg gratings. The theoretical description of FBGs is reviewed, fundamentals behind refractive index changes discussed and current methods of fabricating gratings introduced.

2.1 Diffraction Interaction (or Grating Diffraction)

It is possible to write a diffraction grating into the core of a fibre by exposing the core to a spatially varying pattern of ultraviolet light. This exposure can cause a periodic perturbation of the effective refractive index, n_{eff}, which may be written in the form

$$\delta n_{eff} = \overline{\delta n}_{eff}(z)\left\{1+\upsilon\cos\left[\frac{2\pi}{\Lambda}z+\phi(z)\right]\right\} \qquad (2\text{-}1)$$

Where $\overline{\delta n_{eff}}$ is the dc offset of the average n_{eff}, υ is the fringe visibility of the index change, Λ the period of the perturbation and $\phi(z)$ a term to describe the chirp. For an unchirped FBG $\phi(z)$ is zero. Typical refractive index profiles are shown in Figure 2-1.

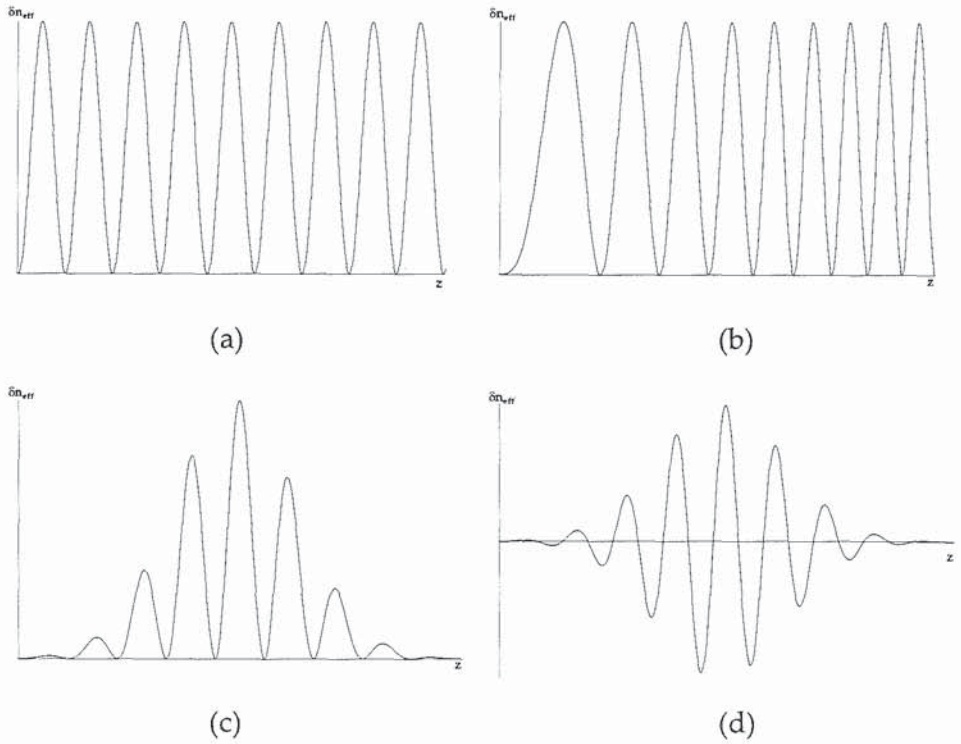

Figure 2-1: Typical refractive index profiles. (a) Uniform with a non-zero δn_{eff}, (b) chirped, (c) Gaussian apodised and (d) Gaussian apodised with a zero δn_{eff}.

This spatially variable perturbation may be considered as a diffraction grating within the core of the fibre. Therefore the effect of the perturbed region on the incident light can be described by the grating equation [1]

$$n_2 \sin\theta_2 = n_1 \sin\theta_1 + m\frac{\lambda}{\Lambda} \qquad (2\text{-}2)$$

where m is the diffraction order and λ is the vacuum wavelength of the incident light. Typically, the first order diffraction dominates in a fibre grating, giving m =-1 as shown in Figure 2-2, where the fibre would be lying horizontal with the diffraction slits along the centre of the core.

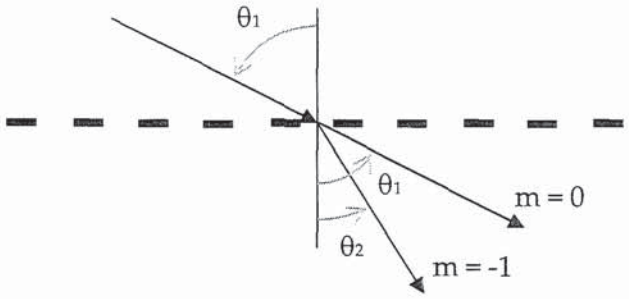

Figure 2-2: Diffraction of light passing through a grating.

Care must be taken when using this methodology to describe the reaction of light within the core since this does not give a full analytical breakdown of all the effects present. However, it does give an accurate description of the angles for which light is diffracted and the resonant wavelength for which light is coupled between the zero and first order diffraction modes.

Gratings may be classed by the periodicity of their perturbation as either Bragg gratings (otherwise known as reflection or short period gratings) or transmission (long period) gratings. The modal coupling properties of these two types of gratings are significantly different. Bragg gratings couple light from the forward propagating core mode to a counter propagating core mode. Long period gratings (LPGs) couple the forward propagating core mode into co-propagating cladding modes.

By using the propagation constant [1]

$$\beta = \frac{2\pi}{\lambda} n_{eff} \tag{2-3}$$

Where

$$n_{eff} = n_{co} \sin\theta \tag{2-4}$$

And n_{co} is the refractive index of the core. Equation (2-2) may therefore be rewritten as

$$\beta_2 = \beta_1 + m\frac{2\pi}{\Lambda} \tag{2-5}$$

Where β_2 and β_1 are the propagation constants after and before the grating, respectively. For a Bragg grating coupling light from the forward propagating core mode to the identical counter propagating core mode; $\theta_2 = -\theta_1$ therefore these angles may simply be rewritten as θ and $n_2 = n_1$. This means that (2-5) can be rearranged to give the resonant wavelength for the counter propagating core mode.

$$\lambda = 2n_{eff,co}\Lambda \tag{2-6}$$

However, a small proportion of this light can be coupled into a counter propagating cladding mode where $n_1 = n_{co}$ and $n_2 = n_{cl}$. In this situation (2-5) becomes

$$\lambda = (n_{eff,co} + n_{eff,cl})\Lambda \tag{2-7}$$

These losses manifest themselves on the short wavelength side of the main Bragg resonance and are often seen within a few nanometres of the Bragg wavelength but with smaller amplitude, Figure 2-3. The multiple sharp peaks observed are due to the radiated mode being reflected at the cladding-air interface and re-entering the core, creating a cylindrical Fabry-Perot effect [1].

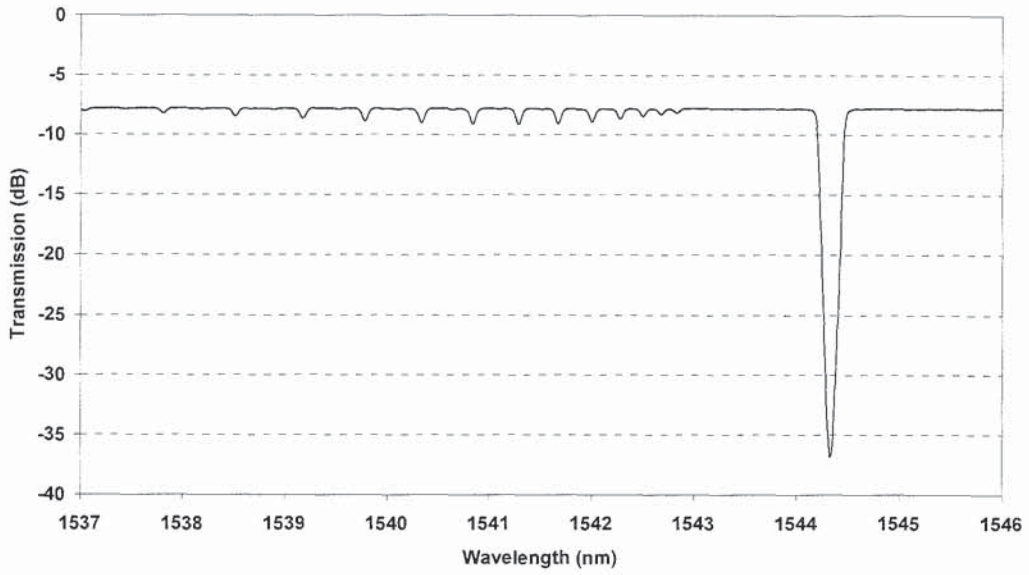

Figure 2-3: Transmission profile of a 25mm long Gaussian apodised FBG demonstrating the resonant Bragg peak at 1544.3nm and short wavelength loss below 1543nm.

Depending on the relative levels between n_{eff}, n_{co} and n_{cl} (refractive index of the cladding) at the perturbation, the modal structure of the supported light can change. For the case where $n_{cl} < n_{eff} < n_{co}$ the light is bound within the core, as is the case with a Bragg grating. Assuming the fibre is surrounded by air, when $1 < n_{eff} < n_{cl}$ the initial core mode can be coupled into the cladding, transferring energy to the cladding modes, as for LPGs. For these cladding modes $\theta_2 \neq \theta_1$, this in essence allows angles less than the critical angle to be obtained and thus the breakdown of TIR within the core. If n_{eff} is less than the refractive index of the surrounding material then energy can be lost through radiation modes if a perturbation exists.

Although the core and cladding modes are defined as being bound within the core or cladding respectively, some of the electric field of the modes protrudes beyond the boundaries. This tail of the electric field is called the evanescent wave, the amplitude of which is far lower than that propagating in the bound regions. These different modal structures are illustrated in Figure 2-4.

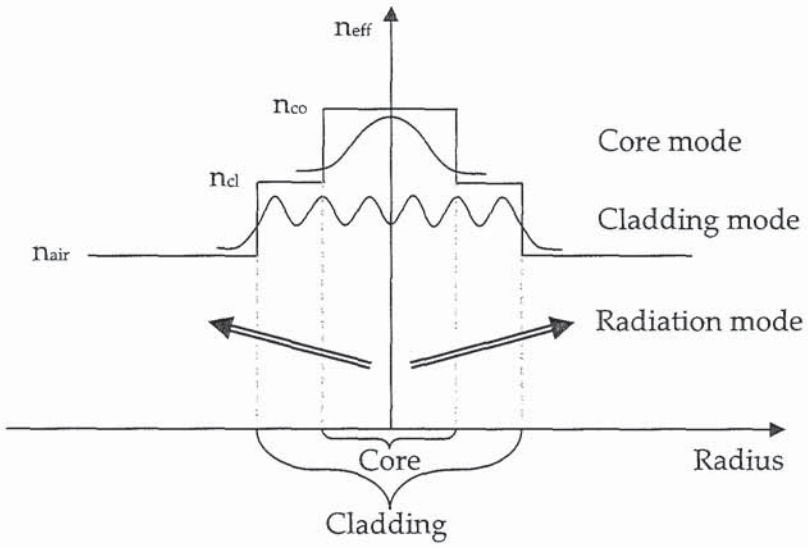

Figure 2-4: Modes supported by an optic fibre.

2.2 Coupled Mode Theory

The information presented in the previous sub-chapter gives a useful qualitative description of how core modes interact with an in-fibre grating. In order to understand these interactions in more detail, attention needs to be turned to more rigorous quantitative techniques. In particular, coupled mode theory is a widely used model due to its ease of use and resolution. The following information will provide a short overview of the important results from coupled mode theory but should a more thorough explanation be required, the reader is directed to the work by Yariv [2].

Two modes may be considered, the forward propagating mode, $A(z)$, and the identical counter propagating mode, $B(z)$. Within an unperturbed medium these two modes are orthogonal and so do not transfer energy from one mode to the other. However, the presence of the grating creates a perturbation thus altering the amplitude of the modes as they transverse the grating. The amplitudes of these two modes, as they propagate through the grating, may be given by R for the forward propagating mode and S for the backward propagating mode [1]

$$R(z) = A(z)e^{i\delta z - \frac{\phi}{2}} \tag{2-8}$$

and

$$S(z) = B(z)e^{-i\delta z + \frac{\phi}{2}} \tag{2-9}$$

where the detuning is given by

$$\delta = \beta - \frac{\pi}{\Lambda} \tag{2-10}$$

The existence of the perturbation causes power to be coupled between $R(z)$ and $S(z)$. In order to maintain power conservation

$$\frac{d}{dz}\left(|R|^2 - |S|^2\right) = 0 \tag{2-11}$$

Therefore

$$\frac{dR}{dz} = i\left(\delta R(z) + \kappa S(z)\right) \tag{2-12}$$

$$\frac{dS}{dz} = -i\left(\delta S(z) + \kappa^* R(z)\right) \tag{2-13}$$

Where the coupling coefficient

$$\kappa = \kappa^* = \frac{\pi}{\lambda}\overline{\delta n_{eff}} \tag{2-14}$$

This evolution of power between the two modes is shown in Figure 2-5.

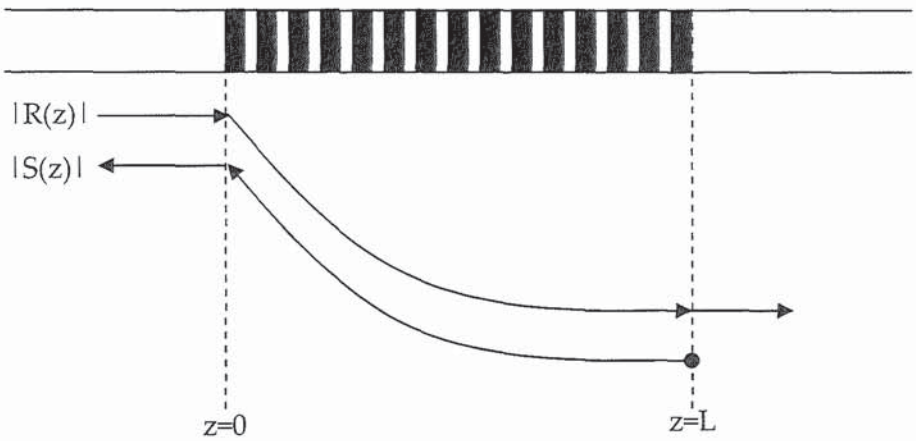

Figure 2-5: Development of the power contained within the forward and backward propagating modes.

Assuming the grating to be uniform along the z-axis, $\overline{\delta n_{eff}}$ and κ are constant, ϕ is zero and the boundary conditions such that the grating extends from –L/2 to L/2, where L is the length of the grating. Also assuming the incident wave approaching from z = -∞ has an amplitude of 1. The amplitude reflection coefficient is given by

$$\begin{aligned}\rho &= \frac{S\left(\frac{-L}{2}\right)}{R\left(\frac{-L}{2}\right)} \\ &= \frac{-\kappa \sinh\left(\sqrt{\kappa^2-\delta^2}L\right)}{\delta \sinh\left(\sqrt{\kappa^2-\delta^2}L\right)+i\sqrt{\kappa^2-\delta^2}\cosh\left(\sqrt{\kappa^2-\delta^2}L\right)}\end{aligned} \tag{2-15}$$

And the reflection coefficient

$$\begin{aligned}r &= |\rho|^2 \\ &= \frac{\sinh^2\left(\sqrt{\kappa^2-\delta^2}L\right)}{\cosh^2\left(\sqrt{\kappa^2-\delta^2}L\right)-\frac{\delta^2}{\kappa^2}}\end{aligned} \tag{2-16}$$

From (2-16) it is clear that when the detuning is zero the maxim reflectivity is given by

$$r_{\max} = \tanh^2(\kappa L) \tag{2-17}$$

Erdogan [1] showed that the bandwidth of an FBG, defined by the first zero points on either side of the resonant peak is given by

$$\frac{\Delta\lambda}{\lambda} = \frac{\overline{\delta n}_{eff}}{n_{eff}} \sqrt{1 + \left(\frac{\lambda_D}{\overline{\delta n}_{eff} L} \right)^2} \tag{2-18}$$

where λ_D is the designed wavelength of the grating. Although this is mathematically a simple solution, experimentally it is irrelevant. The level of the null points would be confused by the noise level of any measurement kit. Russell *et al.* [3] have approximated the full width half maximum (FWHM) bandwidth as

$$\Delta\lambda_{FWHM} \approx \lambda_B s \left[\left(\frac{\delta n}{2n_{core}} \right)^2 + \left(\frac{\Lambda}{L} \right)^2 \right]^{\frac{1}{2}} \tag{2-19}$$

Where $s \approx 1$ for strong gratings and $s \approx 0.5$ for weak gratings and λ_D is the designed wavelength of the grating. This approximation gives a far more experimentally useful value which can easily be measured above the noise floor.

2.3 Refractive Index Change

In order to create the perturbation within the core of the fibre a permanent refractive index change is required. Typically these refractive index changes are created by photosensitivity [4]. However, other methods such as surface relief gratings [5] and micro-bending gratings [6] are less frequently employed.

There are currently many models describing photosensitivity. These models vary with different fibre dopants, inscription wavelengths and laser types. The author

does not intend to give a literature review of these models, but instead to point the reader towards [7,8]. The two strongest models of relevance towards this thesis are the colour centre model [9], the compaction model [10] and the GeH model [11].

During fibre fabrication, a large number of GeO defects are created within the core of the fibre [12]. These defects are introduced during almost all stages of the fabrication procedure, it is impossible to create a perfect chemical reaction during the various stages of preform manufacture and during the fibre drawing process GeE' colour-centre defects can be produced due to the thermoelastic stresses present [12] as well as higher order ring structures [13]. Generally, within germanium doped silica the GeO defects bond with either another Ge or a Si atom to covalently share an electron. This bond has been observed to have an absorption peak at 240nm [14]. Upon photo-excitation by UV light this bond can be broken, releasing the electron freely into the glass matrix and forming part of the conduction band, as shown by Figure 2-6.

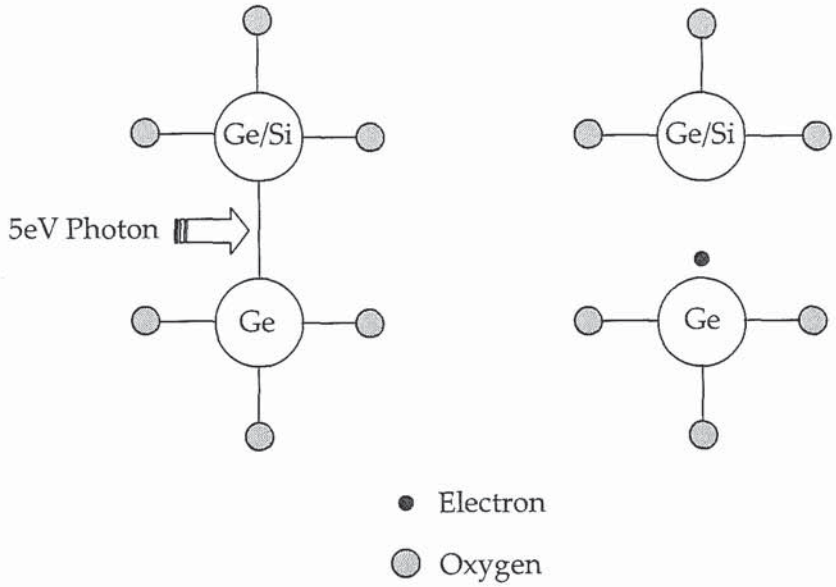

Figure 2-6: GeO defect (left) undergoing UV absorption so causing a break of the Ge-Ge/Si bond and creating a GeE' defect centre (right) and releasing an electron.

The electron may become trapped at the original defect site or at another GeE' hole site creating a change to the absorption characteristics of the molecule, which

in turn leads to a change in the refractive index through the Kramers-Kronig relationship [15]

$$\Delta n_{eff}(\lambda) = \frac{1}{2\pi^2} P \int_0^{\infty} \frac{\Delta \alpha_{eff}(\lambda)}{1 - \left(\lambda / \lambda'\right)^2} d\lambda \tag{2-20}$$

Where P is the principal part of the integral, $\Delta \alpha_{eff}(\lambda)$ is the effective change in the absorption coefficient of the defect, λ the wavelength of the absorbed light and λ' the wavelength for which the refractive index is calculated.

The colour centre model gives a good approximation for the effects of the photosensitivity in SiGe fibres, but cannot fully account for all observed effects. It has been observed [10] that compaction of the physical structure of Si can occur when exposed to light at 248nm. This compaction leads to an increase in the refractive index of the material. The proposed model to create the densification derives from the collapse of higher order ring structures whilst under UV irradiation.

One simple method of increasing the photosensitivity of a fibre is to soak it in hydrogen, a method known as hydrogenisation or hydrogen-loading. The UV light is thought to induce the formation of GeH and generate GeE' centres [11]. As the formation of GeH changes the band structure in the UV region and considering the extra GeE' centres, the refractive index of the fibre is increased in accordance with (2-20) due to a change in the absorption coefficient, thus allowing stronger FBGs to be written within the core of a fibre [16]. This technique is widely used throughout the research community as it provides a cheap alternative to highly photosensitive fibre with co-dopants such as boron [17]. Boron itself has little effect on the photosensitivity, instead it reduces the refractive index of the core of the fibre thus allowing more germanium to be introduced. This extra concentration of Ge leads to a higher photosensitivity of

the fibre whilst maintaining a near identical refractive index profile to before introducing the boron.

The three processes previously mentioned can be combined to give a good overall view of the photosensitivity mechanism present in Ge doped Si fibres. There is continued disagreement within the research community as to the exact mechanisms responsible for the observed effects. This will probably forever be the case as the fabrication processes are incapable of creating microscopically homogonous fibres which would allow certain theories to be discredited. As long as there are complications in the fibre structure there will be difficulty in understanding the photosensitivity effects.

2.4 Thermal Annealing

The induced refractive index caused by the UV illumination can be subsequently erased by the process of thermal annealing, as shown in Figure 2-7.

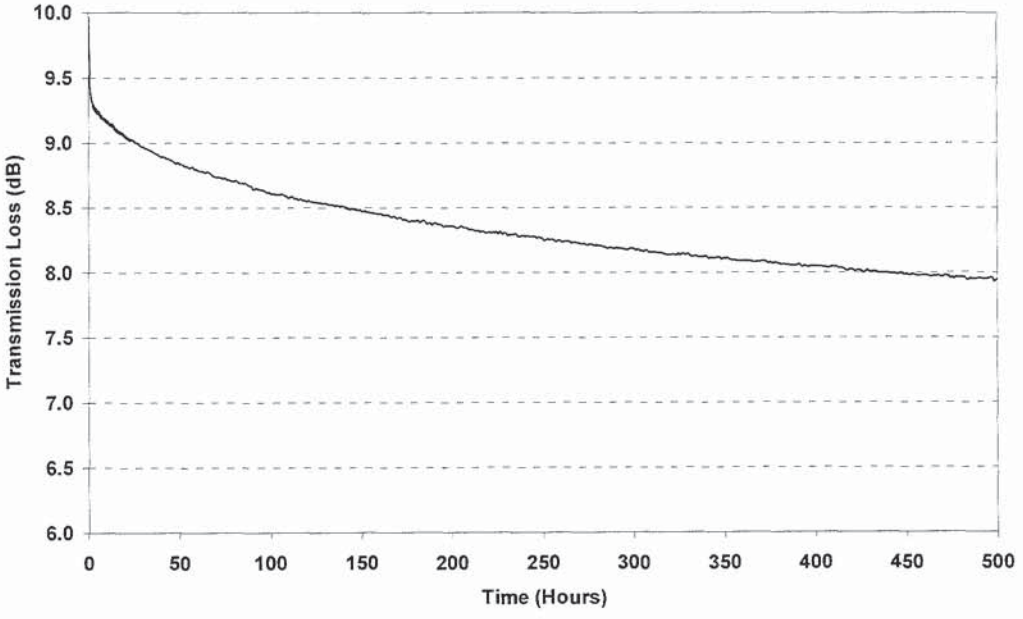

Figure 2-7: FBG undergoing annealing at 95°C.

This degradation in the transmission loss of the grating can have detrimental effects on the performance of a system which an FBG is embedded within.

Therefore a broad understanding of the causes and effects of annealing is required to predict how the grating may respond at some later time.

Erdogan *et Al* [18] demonstrated that the electrons caught in GeE' traps may escape back into the conduction band if they are able to obtain enough energy, as shown in Figure 2-8. This energy may come from a thermal annealing process, having implications over the lifetimes of FBGs.

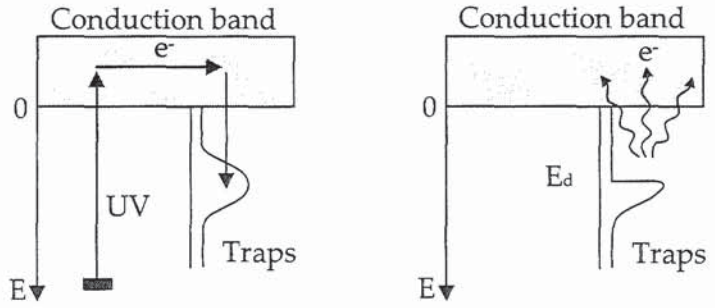

Figure 2-8: Electrons excited by UV irradiation and trapped by a GeE' trap (left). Thermal depopulation of the traps (right).

These trapped electrons distribute themselves in a Gaussian form across the energy range, divided by a demarcation energy, E_d. For energy states where $E<E_d$ the electrons are in thermal equilibrium with the conduction band and so at any later time may escape from the trap and return to the conduction band. For energy states where $E>E_d$ the traps are too deep to be thermally excited so maintaining the trapped population. This methodology leads to the power law of thermal annealing where the normalised refractive index change of Ge doped silica fibre may be given by [18]

$$\eta = \frac{1}{1+\exp\left[\left(E_d - \Delta E\right)/k_B T_0\right]} \tag{2-21}$$

Where k_B is the Boltzman constant and T_0 is an experimentally determined temperature related constant. The demarcation energy level is not defined by a

specific energy value. There would be a probability distribution that the electrons could escape the traps beyond the demarcation energy.

The use of hydrogen to increase photosensitivity complicates the thermal annealing process. It is thought that the trapped states in hydrogen loaded fibre have a wider energy distribution. This allows more states to be closer to the conduction band hence requiring less energy to decay. This would lead to a more rapid decay of the hydrogenated fibres at low temperatures in comparison with the non-hydrogenated fibres. Baker *et al* [19] experimentally proved this point, showing that hydrogen loaded fibres did not obey the power law. They proposed a log time model for the decay of the gratings under thermal annealing. This log time model states that

$$\begin{aligned} \eta &= 1 - K\log\left(\frac{t}{\tau}\right) && \text{for } t > \tau \\ \eta &= 1 && \text{for } t \le \tau \end{aligned} \tag{2-22}$$

Where K is a constant, τ is temperature dependant and t is time. The values of K and τ are calculated by fitting curves to data obtained during annealing experiments.

2.5 Fabrication Methods

FBGs were accidentally invented by Hill during an experiment to investigate the non-linear effects within a length of optical fibre [20]. During the experiment the back reflections from a flat end cleave of the fibre caused the incident beam and the reflected beam to interfere, causing localised regions of high intensity. At these regions it was found that the refractive index had changed due to the natural photosensitivity of the fibre to the incident 488nm light. Thus the transmitted light was seen to be attenuated and actually back reflected along the fibre. These gratings became known as self-organised gratings due to their ability to form by themselves. Despite the enormous potential of the technique, this spontaneous formation did not allow much flexibility over the wavelengths

reflected or the exact location of the reflective element due to these properties being fundamentally linked to the incident wavelength. Other methods of exploiting this newly discovered photosensitivity were therefore required.

2.5.1 Holographic FBG Fabrication

The holographic technique involves splitting a coherent laser beam into two, directing the beams along different paths and then recombining the beams at some arbitrary angle. As these beams recombine, the wave fronts create a periodic intensity profile which can be projected onto a fibre as shown in Figure 2-9.

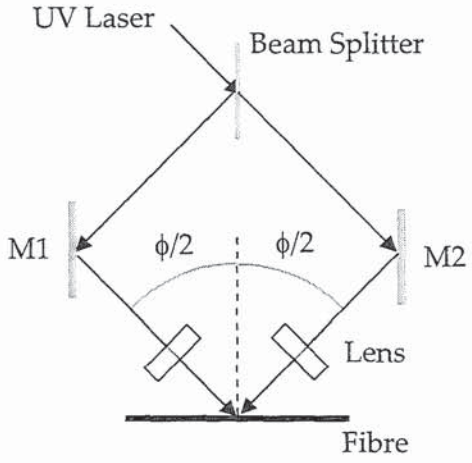

Figure 2-9: Holographic set-up for fabrication of FBGs. M1 and M2 are mirrors.

Such a set up requires the beam to be split, preferably with a 50:50 beam splitter then passed along two identical but opposite optical paths and then recombined after passing through cylindrical lenses. The cylindrical lenses are required to focus the beam down to the size of the core to give a higher power density, allowing stronger FBGs to be written. The fringe pattern written across the core of the fibre is given by

$$\Lambda = \frac{\lambda_w}{2\sin\phi} \tag{2-23}$$

And subsequently

$$\lambda_B = \frac{n_{eff}\lambda_w}{\sin\phi} \tag{2-24}$$

Where λ_w is the wavelength of the UV laser. The major advantage presented by holographic techniques is their ability to write fringes of any arbitrary period. This then allows a Bragg grating of any wavelength to be written, giving huge flexibility to the user. However, the free space nature of the system requires a very stable set-up in order to maintain perfect interference of the two beams over a number of minutes. Instabilities can be introduced from laser pointing drift as well as mirror, lens and fibre movement. These instabilities are ultimately magnified as the two beams take different paths so movement on one mirror will cause a relative movement between the two beams, causing an imperfect interference pattern. Beyond the high tolerances required of the mechanical set-up, there is a hugely variable human factor to include. To have a high level of repeatability, the operator needs to perfectly place the fibre in the same place time after time in relation to the two incident beams. Something that is particularly difficult due to the judgemental nature of optical free space alignment. Subsequently, holographic set-ups tend to create low quality gratings. A simplistic holographic set-up also suffers from the problem of having a fixed FBG length, ultimately fixed to the area of overlap of the two beams. This reduces the utility of the holographic system due to the small length of the FBG resulting in a grating with a large bandwidth, as defined by (2-18) and (2-19).

2.5.2 Phase Mask FBG Fabrication

An alternative method of creating the interference pattern to allow grating writing is to use a phase mask [21]. The phase mask technique involves passing the laser beam through a surface relief diffraction grating, splitting ~40% of the incident into each the +1 and -1 diffraction orders. A majority of the remaining light is transmitted through the zero diffraction order with a small fraction passing through the higher diffraction orders. The +1 and -1 diffraction orders from different positions along the phase mask interfere, the fibre is then placed

within this interference region, as shown in Figure 2-10. Typically, this interference zone is within a millimetre of the phase mask.

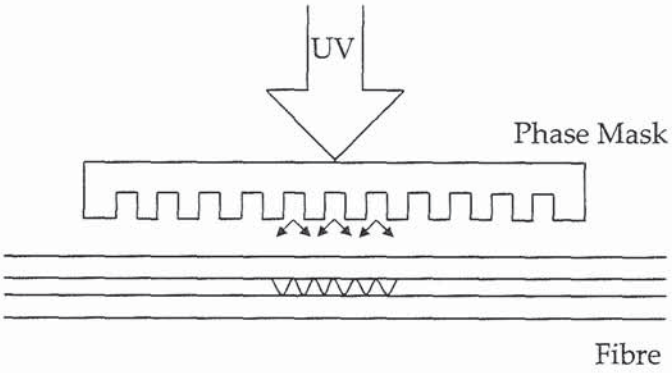

Figure 2-10: Phase mask technique for fabricating FBGs.

The phase mask technique writes fringes with a period of

$$\Lambda = \frac{\Lambda_{PM}}{2} \tag{2-25}$$

Where λ_{PM} is the period of the phase mask. The Bragg wavelength is then given by

$$\lambda_B = n_{eff}\Lambda_{PM} \tag{2-26}$$

The phase mask technique is a far more stable set-up due to a lower level of free space alignment required. There is no need to align the two beams relative to each other, as with the holographic set-up, only a need to align the incident beam perpendicular to the fibre and phase mask. In addition to this stability benefit there is the added advantage that the beam may be scanned relatively along the length of the fibre allowing longer FBGs to be written [22,23]. Despite these benefits, there are a few draw backs with the phase mask technique. The area of interference where an FBG can be written behind a phase mask is relatively small, as shown in Figure 2-11. An example of a fringe pattern written into a piece of SMF-28 using a phase mask technique and a 244nm laser is shown in Figure 2-12.

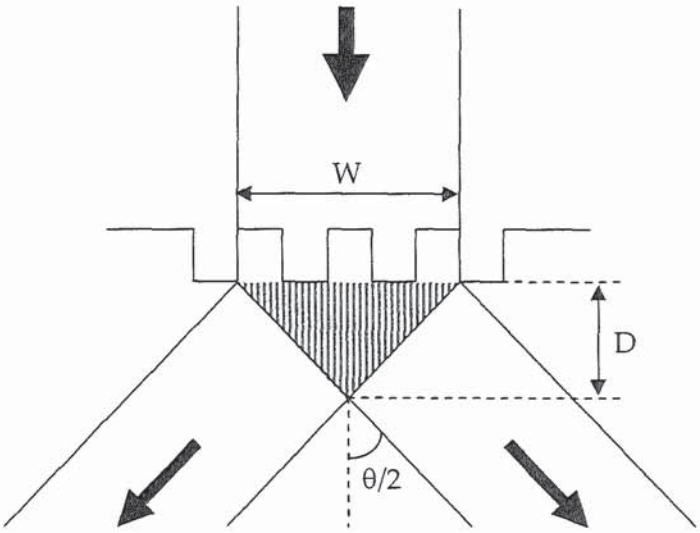

Figure 2-11: Close up of the phase mask, showing the interference pattern from the +1 and -1 diffraction patterns in the grey striped triangle.

Figure 2-12: Fringe pattern written into the core of a piece of SMF-28, viewed under a microscope using an immersion lens.

The intensity pattern behind the phase mask is given by [24]

$$I_{0,\pm1}(x,z) = 4\left\{\begin{array}{l} C_1^2\cos^2\left(2\pi x/\Lambda_{PM}\right) + C_0^2 + 2C_0C_1\cos\left(2\pi x/\Lambda_{PM}\right) \\ \times\cos\left[2\pi z\left(1-\sqrt{1-\left(\lambda/\Lambda_{PM}\right)^2}\right)/2\right] \end{array}\right\} \qquad (2\text{-}27)$$

Where x is the position along the phase mask, z the distance from the phase mask, C_1 the amplitude of the ±1 order, C_0 the amplitude of the 0th order and λ the wavelength of the incident light. A cross-section of the intensity pattern formed by the phase mask is shown in

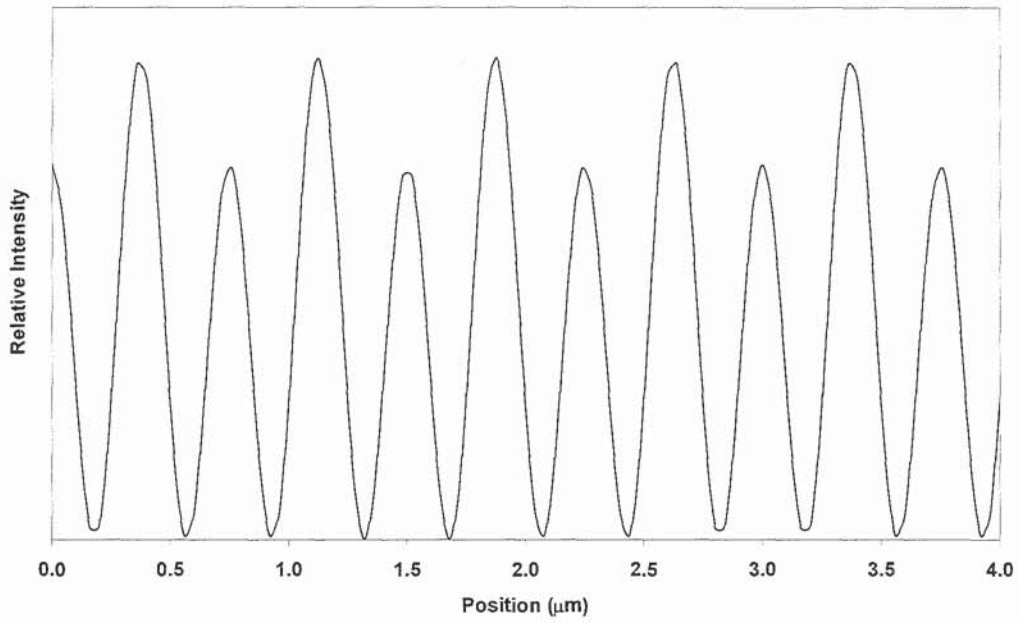

Figure 2-13: Intensity pattern formed 200μm behind a phase mask by 244nm light passing through a phase mask with a period of 750nm, 40% of light in the ±1 orders and 3% in the 0th order.

The variation in fringe heights in Figure 2-13 is defined by the magnitude of light in the 0th order, the greater the magnitude the worse the uniformity of the fringe pattern. A high quality phase mask will have about 3 – 5% of the diffracted light in the 0th order. The higher the visibility of the fringes the stronger the grating, thus a poor quality phase mask limits your FBG writing efficiency.

The maximum depth of the interference pattern, D is given by [8]

$$D = \frac{W}{2\tan\left(\theta/2\right)} \tag{2-28}$$

Where W is the width of the incident laser beam and θ/2 the angle defined in Figure 2-11. The length of the grating can be limited to the length of the phase mask when using a scanning beam or scanning phase mask technique. Also, any stitching errors on a phase mask will directly print themselves into the refractive

index pattern of the grating. These stitch errors manifest as large sidelobes either side of the main grating peak.

2.5.3 Apodisation

Uniform fibre Bragg gratings (FBGs), when viewed either side of the main Bragg resonant peak, display a high level of oscillations which appear to continue on to infinity. These oscillations are known as sidelobes. With the high demands of modern day communications and sensing systems, these sidelobes cause problems due to crosstalk. In order for a neighbouring channel to create negligible crosstalk the sidelobes need to be of minimal amplitude, preferably below -60dB at the point of the next channel. By employing uniform FBGs in a wavelength division multiplexed (WDM) system, this would be near impossible. Subsequently, the idea of apodisation can be applied to an FBG, where the refractive index at the beginning and end of the grating is tapered as in Figure 2-1 c) and d). This causes a drop in the amplitude of the sidelobes but also creates an increase in the bandwidth due to the grating having a shorter effective length, as shown in Figure 2-14. This figure was calculated using IFO Gratings which uses a transfer matrix approach to create the spectra. This approach requires the operator to specify the number of segments and total number of data points that the calculations are performed on. If the number of segments or the total data points are too low then a low resolution and incorrect spectra may be displayed.

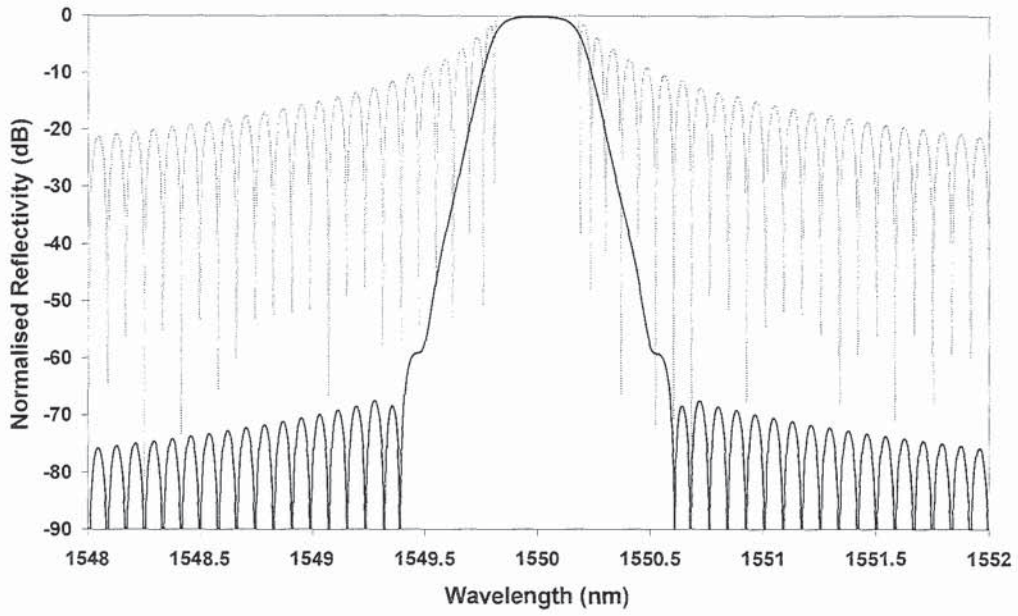

Figure 2-14: Theoretical reflection profiles of a uniform FBG (grey) and a Gaussian apodised FBG (black).

The simplest way to understand the response of the sidelobes is to consider the FBG as a Fourier element and employ Fourier transforms to the shape of the grating as the grating is effectively a filter. This methodology holds as an input signal will, over time, trace out the profile of the FBG as it is reflected from different points along the grating, as shown in Figure 2-15.

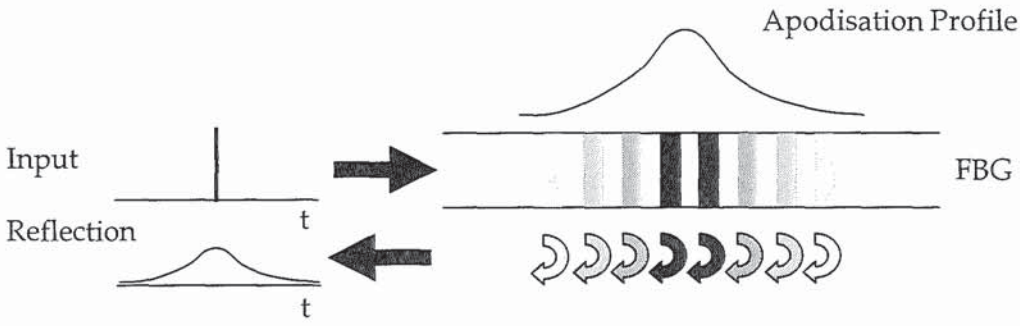

Figure 2-15: Schematic of reflections in time within an FBG.

In order to take the reflected time domain signal into the frequency domain, as required to gain spectral information, the Fourier cosine transformation is required. If the filter was an infinitely long sinusoidally varying perturbation in

the refractive index, similar to Figure 2-1(a), then a single frequency peak would occur at the resonant frequency. However, as the filter is a truncation of this infinite series it corresponds to a multiplication with a rectangular window of length T_{span}. The Fourier transform then assumes that the signal is a succession of versions of this truncated signal in the time domain, leading to a spectrum with harmonic components at frequencies equal to multiples of $\Delta f=1/T_{span}$ [25]. This is demonstrated with Figure 2-16 and Figure 2-17, T_{span} for the uniform profile is 2, giving Δf as 0.5. The sidelobe minima in Figure 2-17 therefore occur with a frequency period of 0.5. By applying an apodisation profile to the truncated signal the amplitudes of the harmonic components are reduced. Such an apodisation profile reduces the amplitude of the two ends of the FBG by tapering them down to zero. Two such apodisation profiles are shown in comparison with a uniform non-apodised profile in Figure 2-16.

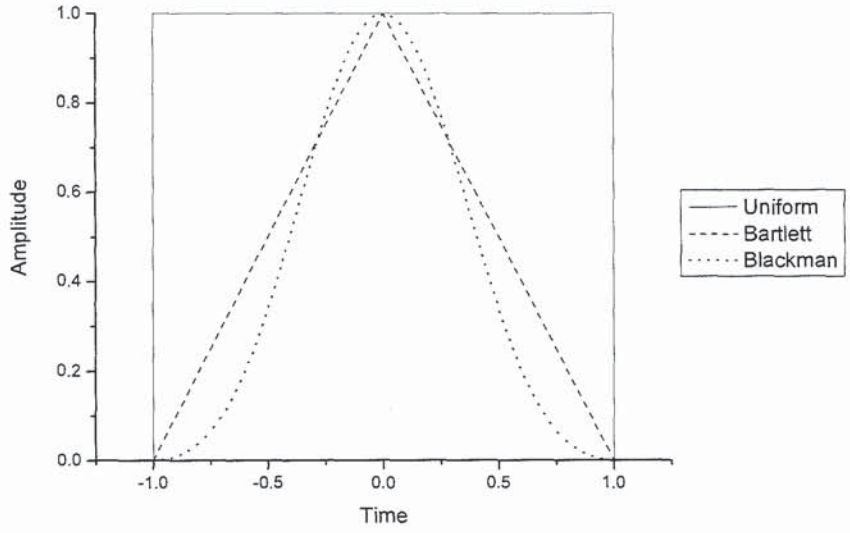

Figure 2-16: Three apodisation profiles; uniform, Bartlett and Blackmann apodisation.

By taking the Fourier cosine transformation of these apodisation profiles, the response of the profile, otherwise known as the instrument function I(f), is given by [26]

$$I(f) = \int_{-a}^{a} \cos(2\pi ft) A(t) dt \tag{2-29}$$

Where a is the half-width of the profile, f is frequency, t is time and $A(t)$ the apodisation profile. By applying this Fourier cosine transformation to the profiles in Figure 2-16 their responses are shown in Figure 2-17.

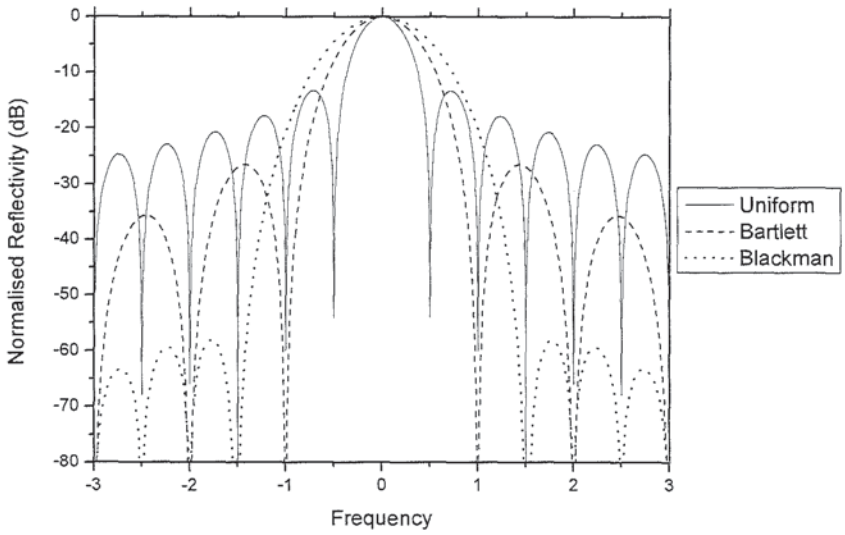

Figure 2-17: Instrument functions for the uniform, Bartlett and Blackmann apodisation profiles, shown on a logarithmic scale.

By tapering the edges of the apodisation profiles to zero, as is the case for the Bartlett and Blackman profiles, the side lobes are suppressed. The magnitude of this suppression depends on how rapidly the tapering takes place. The Bartlett profile has no gradual introduction to the slope of the side of the profile, unlike the Blackman profile. This coupled with the sharp peak causes the Bartlett profile to have higher sidelobes than the Blackman profile. A good rule of thumb is: the smoother the profile, the lower the sidelobes.

Although the Fourier technique can give a good understanding and a relatively accurate reflection spectra from an apodisation profile there is one major limitation. This technique can only be used in the weak grating regime. If the grating is strong, the input signal is unable to reach the end of the grating due to

being totally reflected by the initial fringes. This means that there is no frequency component contributed from the far end of the grating, thus any Fourier transformation will give an incorrect representation. For strong gratings more complex techniques, generally based on the coupled mode theory, need to be considered such as the Runge-Kutta method or the transfer matrix approach [27].

The fabrication of arbitrarily apodised FBGs is difficult to achieve, numerous methods for intrinsically apodised gratings have been proposed [28,29] but these give little control over the refractive index profile of the gratings. Certain methods of using variable scan speeds across the FBGs have also been approached [30] where the grating is scanned at a lower speed towards the centre of the grating and at a faster speed at either end. This technique and all intrinsically apodised refractive index profiles have a variable effective refractive index across the length of the grating, as shown in Figure 2-18 (left).

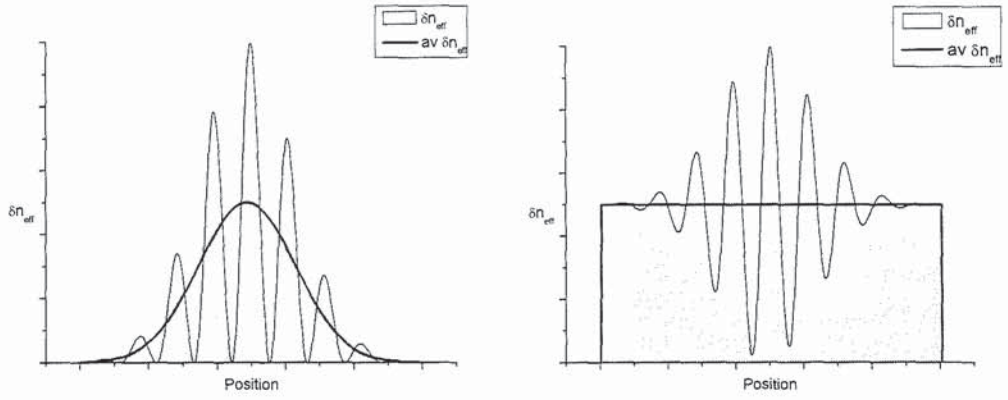

Figure 2-18: Refractive index structure of an FBG with a variable effective refractive index (left) and one with a constant effective refractive index (right).

This variation in the average index causes asymmetry in the spectral profile of the grating as shown in Figure 2-19. The short wavelength sidelobes are due to the centre of the grating providing the reflection for higher wavelengths than either side of the grating. The low average index of the two ends support identical low wavelength reflection, however the two ends are spatially separated therefore a

Fabry-Perot cavity is set up between these wavelength reflections, causing the low wavelength sidelobes.

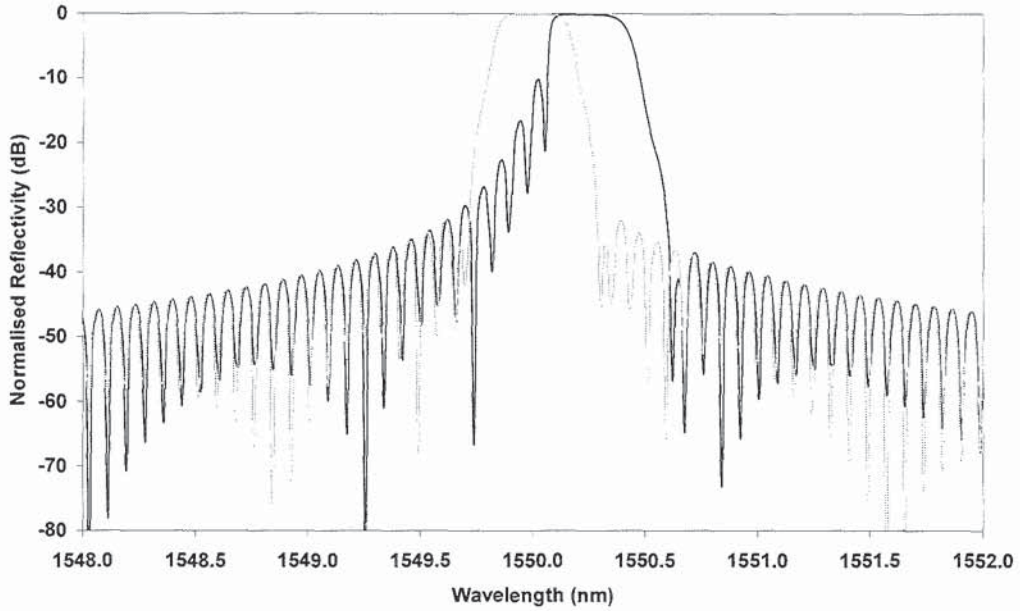

Figure 2-19: Two modelled Gaussian apodised FBGs showing one with a uniform average index (grey) and one with a variable average index (black).

The two FBGs are offset in wavelength due to the modelling maintaining the same transmission strength for both gratings. As the variable average index grating is effectively shorter than the uniform one, a larger maximum δn_{eff} is required, thus pushing the resonant peak to a higher wavelength.

2.7 Summary

The theories behind a majority of the physics involved in FBG fabrication are well known with the exception of photosensitivity where a number of knowledge gaps still exist. These difficulties are hampered by the complexity in directly measuring the atomic scale changes that are attributed to the formation of the gratings. The high level of definition in the grating theory allows fabricated FBGs to be accurately modelled and any deviations away from the perfect profile to be analysed. This information can be directly fed back to improve the quality of a fabrication system.

3

Advanced FBG Fabrication Systems

The author's CASE sponsorship required a period of employment at Indigo Photonics. This work involved helping to improve the quality of a scanning phase mask FBG fabrication system and to characterise and exploit the abilities of a direct write system. A majority of the work was conducted alongside Dr Karen Chisholm (now Dr K. Carroll) for the scanning phase mask technique and John Mitchell for the direct write system. Due to the commercial nature of the work conducted, the focus of the work was to achieving high quality results rather than conducting highly detailed explorations of all aspects studied. This chapter therefore presents a large number of results, with appropriate explanations, over a broad range of topics.

3.1 Scanning Phase Mask System

3.1.1 Introduction

From the telecoms boom a large number of dispersion compensation devices were invented and subsequently deployed in long haul transmission systems

[31]. A large number of these devices were passive including lengths of dispersion compensating fibres [32], giving little flexibility to the end user. As the technology matured, tuneable dispersion compensation devices were invented [33], one of which was designed by Indigo Photonics [34,35]. The concept behind the dispersion compensator was based on a Gires-Tournois etalon (GTE). Such etalons operate by having two mirrors, the first one partially reflective and the second completely reflective. This creates a cavity where a signal is trapped until it escapes out of the cavity at some later time, Figure 3-1. The partially reflective mirror is able to control the dispersion properties of the cavity by moving its position relative to the highly reflective mirror.

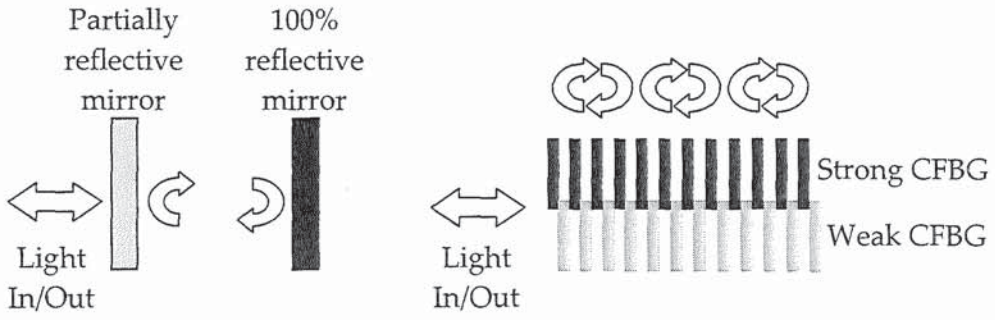

Figure 3-1: Free space Gires-Tournois etalon (left) and a FBG based GT etalon (right).

A similar device may be fabricated within an optic fibre by interlacing two chirped FBGs of different strengths, giving a spatially distributed fibre based GTE. This combines the capabilities of the free space GTE with the advantages of an FBG. A free space GTE would have high coupling losses if such a device was used in conjunction with fibre optics, hence the advantage of making an all fibre device. The interleaved CFBGs create a Fabry-Perot effect causing amplitude modulation in the dispersion of the grating, shown in Figure 3-2. By strain or thermal tuning the grating, the dispersion value at any specific wavelength may be increased or decreased, as indicated by the ball and arrow.

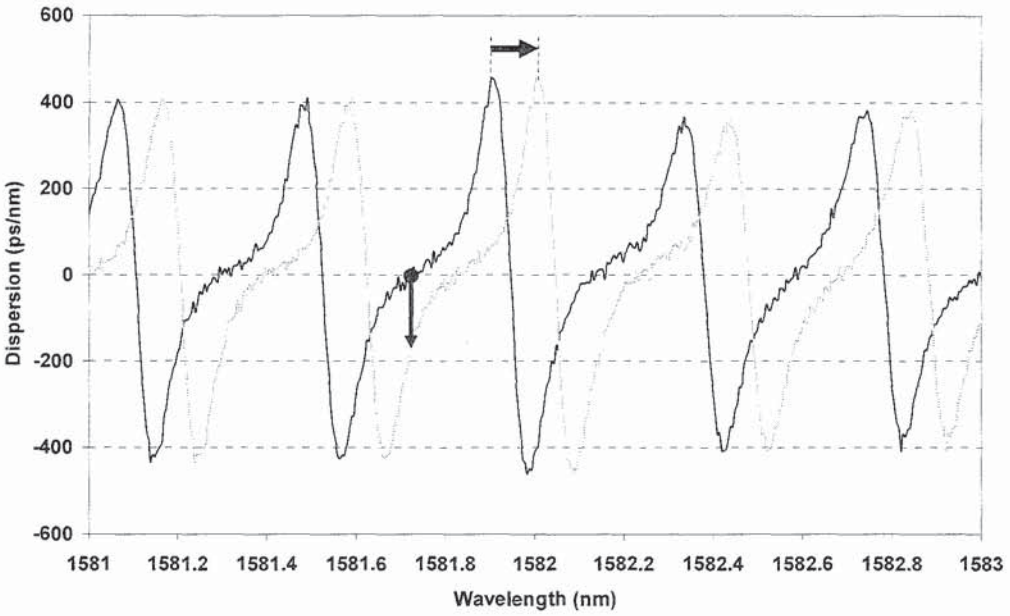

Figure 3-2: Dispersion of a fibre based GT etalon, showing the effect of tuning on the dispersion.

The dispersion takes the hyperbolic form as it is the differential of the group delay, see Figure 3-19. The group delay shape may be qualitatively described by the 'effective medium picture'. This suggests that the edges of the grating act as a Fabry-Perot resonator. The large delay sections are due to the frequency of light becoming trapped within the resonator for a number of round trips, creating a larger delay. However at the centre of the spectral response of the grating, the delay is low as the frequency of the light is equal to that of the periodic perturbation of the grating and so is less susceptible to the Fabry-Perot effect.

Using a single GTE in this fashion has a drawback, when operating within an ITU grid the channels have a limited width. This compensating scheme would then give significantly different dispersion compensation to the short wavelength end of the channel in comparison with the centre of the channel. In order to overcome this issue, two GTEs can be cascaded via a circulator. If the second GTE is written weaker with a negative dispersion then when tuning, a roughly flat region is created which increases or decreases its dispersion value, as shown in Figure 3-3.

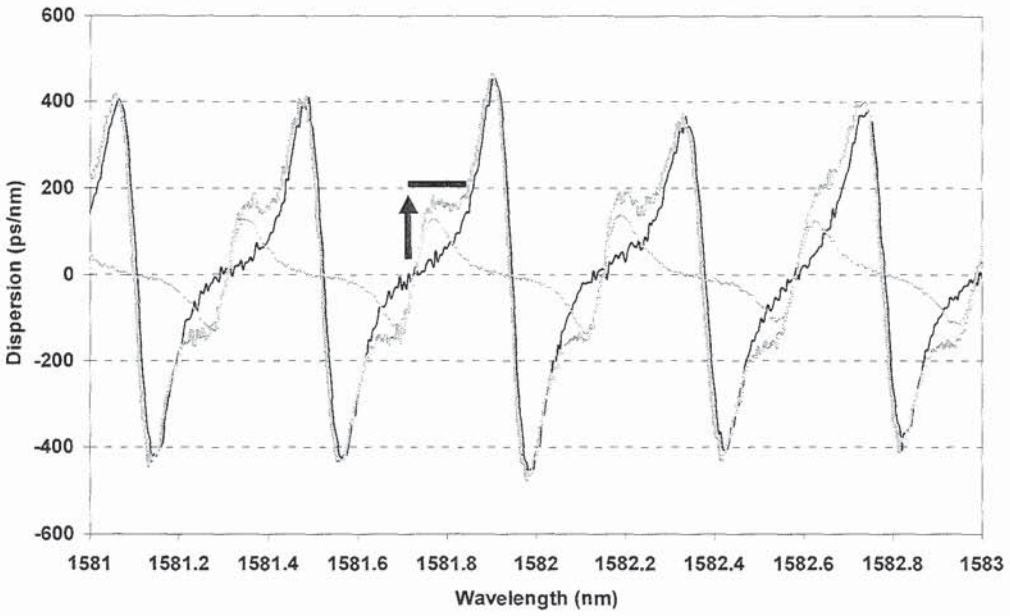

Figure 3-3: Dispersion of two GT etalons (thin grey and black lines) and showing the summation of the two dispersions (thick grey). The arrow and flat line indicates how the dispersion in a set region is raised and flattened.

In order to create even dispersion compensation across each channel, the amplitude of each consecutive peak needs to be equal. This can be strongly effected by the profile of the grating used. If a CFBG is not apodised at the edges the dispersion forms a wavelength dependant oscillation, as shown in Figure 3-4. A point to note is that this oscillation is not the same as the oscillation within the GTE, it is caused by a Fabry-Perot effect between individual points along the CFBG and the edge of the grating profile where the refractive index steps up sharply. If two such dispersion patterns were interleaved to create a GTE then each consecutive dispersion peak would be different.

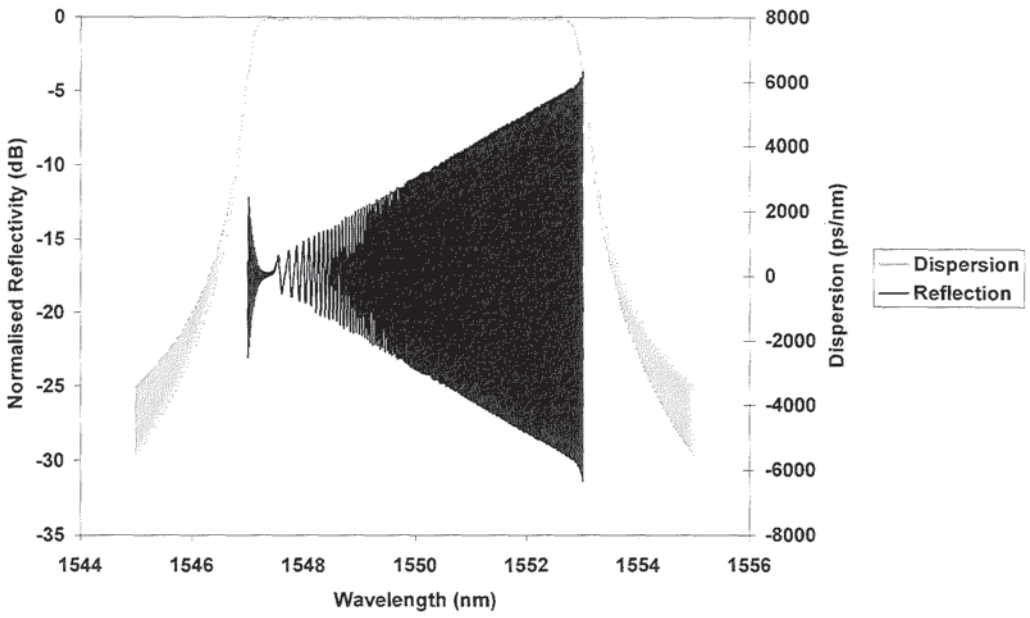

Figure 3-4: Theoretical reflection and delay profile of a 5cm long non-apodised chirped grating.

In order to reduce this ripple the edges may be apodised, eliminating the Fabry-Perot effect and thus the ripple [36]. The subsequent outcome is a flat dispersion within the band of the grating, shown in Figure 3-5.

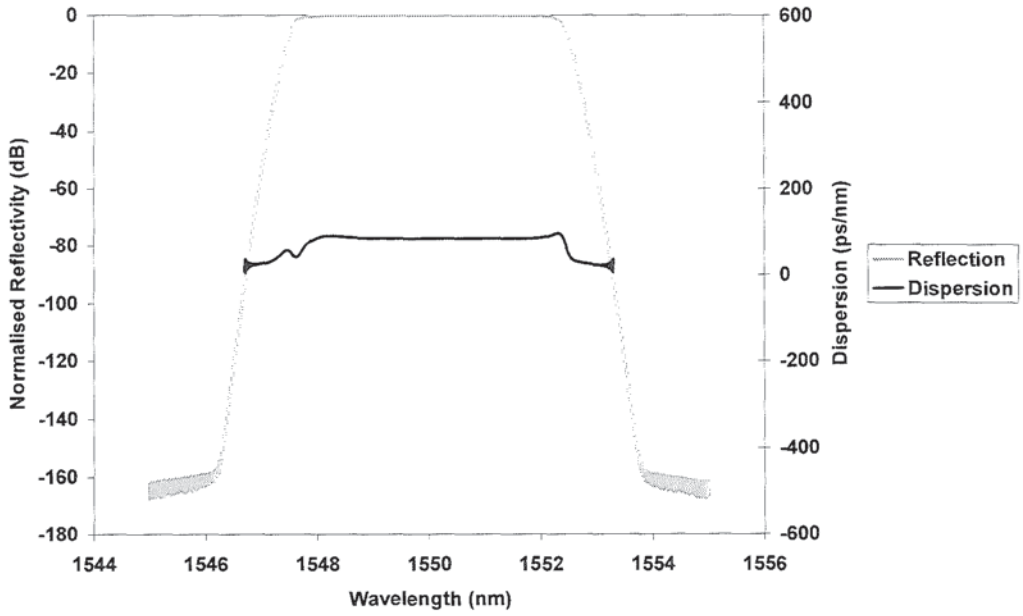

Figure 3-5: Theoretical reflection and group delay profile for a second order, super-Gaussian apodised grating.

The design of the grating was chosen by balancing the total length of the grating, the effective bandwidth coverage, the sidelobe levels and the availability of phase masks. Subsequently a second order super-Gaussian was used.

Practically, it is impossible to create a perfectly apodised FBG so a flat dispersion will never be realised. The slightest deviation away from the perfect profile will cause significant effects on the dispersion and spectra of the gratings. Feced and Zervas [37] have shown how random phase and amplitude errors in the refractive index of a grating negatively effect the sidelobe suppression and the time delay, thus effecting the dispersion. The conclusion was that a grating fabrication system is required to have a "long coherence length" or in other words: have a long distance over which dephasing, with respect to the perfect grating, occurs in order to keep the standard deviation of the time delay low. Such random amplitude and phase errors can be induced by numerous aspects of a fabrication system. These can include: air currents, vibrations on optics, laser stability (both in power and pointing) and stage resolution. These random effects, coupled with systematic inaccuracies from the control system, dramatically increase the difficulty of fabricating high quality FBGs. The following sections explain ways to reduce these effects for the fabrication of commercial devices.

3.1.2 Optical Design

The scanning phase mask setup [38] consisted of a 244nm Coherent Innova frequency doubled (FreD) laser, a translation stage mounted scanning mirror, a phase mask mounted on a piezo block and two clamps to hold an optical fibre in front of the phase mask. The piezo is used to allow apodisation of the grating. Dithering the phase mask, parallel to the fibre, causes the visibility of the diffraction pattern to be blurred out, reducing the visibility of the grating. The entire setup was placed within a transparent Perspex laser safety cage which was located on top of an air supported optical table.

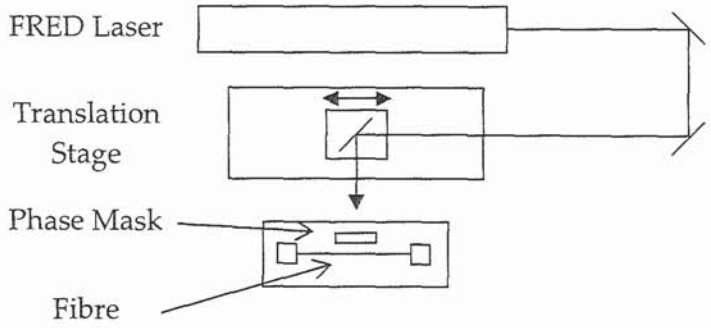

Figure 3-6: Schematic of the scanning phase mask setup employed at Indigo Photonics.

3.1.3 System Improvements

The system was initially optimised to fabricate high quality, uniform period, apodised FBGs. The initial problem was that when apodising chirped FBGs, the amplitude of oscillation on the piezo needed to vary depending on the wavelength being written. Quantifying the quality of apodisation also proved problematic, theory will show that the better apodised an FBG, the lower the sidelobes, see section 2.5.3. However, theoretical modelling shows the sidelobes dropping below the measurement range of any test kit, as demonstrated in Figure 3-5. A typical measurement kit will have difficulty measuring signals below -60dB.

To quantify the quality of the gratings written, the concept of "phantom gratings" was invented by the team at Indigo. This is a process where an FBG is inscribed by applying a continuous apodisation with zero δn across the entire length of the grating. When measuring such a grating in reflection there should be no reflected power across the band of the FBG. The larger the reflection, the more inaccurate the apodisation. This concept was used to see how well the initial system could apodise a CFBG before any improvements were made. The results showed that a phantom grating was written with about 20dB amplitude above the noise floor, with a dip around 1550nm, Figure 3-7 middle trace. This dip demonstrates the most efficient wavelength for which the apodisation occurred. The previous work

at Indigo Photonics was based around 1550nm, consequently the most effective apodisation was in this region. The wavelength for which the dip occurs depends on the voltage applied to the piezo. For perfect apodisation the phase mask was dithered by ±1/4 phase mask period. The signal to apply this dithering was provided by a signal generator using, where the voltage applied at the peaks and troughs would move the phase mask in the positive or negative direction. The phase mask displacement was not varied in a linear fashion relative to the apodisation envelope. In order to recreate the apodisation envelope correctly the fringe shape needs to be considered as well as the envelope. The refractive index profile of a grating can be represented by:

$$A(z)F(z) = \frac{\Lambda}{\pi}\left[\cos\left(\frac{2\pi}{\Lambda}\right)\cos\left(\frac{2\pi a(z)}{\Lambda}\right)\right] \tag{3-1}$$

Where $A(z)$ is the apodisation envelope, $F(z)$ describes the UV fringe pattern, Λ the grating period, z the distance along the fibre and $a(z)$ is the amplitude of the piezo oscillation. The refractive index pattern which the phase mask imprints into the fibre may be described by

$$F(z) = \cos\left(\frac{2\pi z}{\Lambda}\right) \tag{3-2}$$

Therefore the amplitude of the piezo oscillation, as a function of position, may be written as

$$a(z) = \frac{\Lambda}{2\pi}\cos^{-1}\left(\frac{\pi}{\Lambda}A(z)\right) \tag{3-3}$$

This methodology was directly applied to the apodisation system at Indigo.

The greater the voltage applied, the larger the phase mask movement. In order to characterise this voltage-wavelength dependency, five phantom gratings were written with a variety of voltages. As the voltage increased so did the wavelength for which the dip occurred, as shown in Figure 3-7.

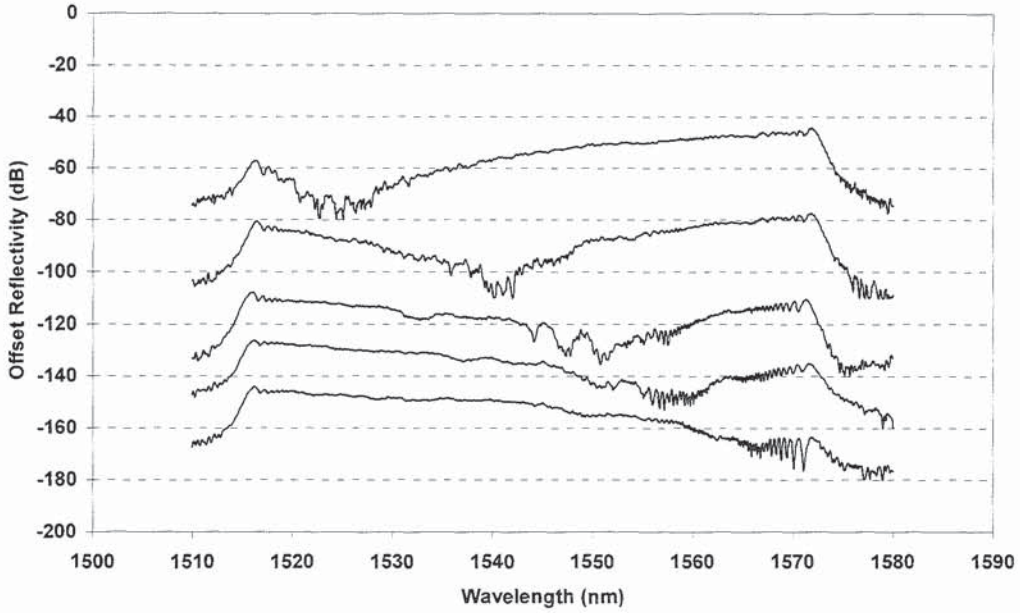

Figure 3-7: Phantom gratings written with variable piezo apodisation voltage, lowest voltage at the top progressing towards highest voltage at the bottom. Top trace presented in its original position, each subsequent trace offset for clarity.

This voltage-wavelength information was used to calibrate the system and the author wrote a LabVIEW program to actively detect which wavelength was being written which then fed back the corrected voltage to the piezo. With the new program installed the phantom grating was repeated, Figure 3-8.

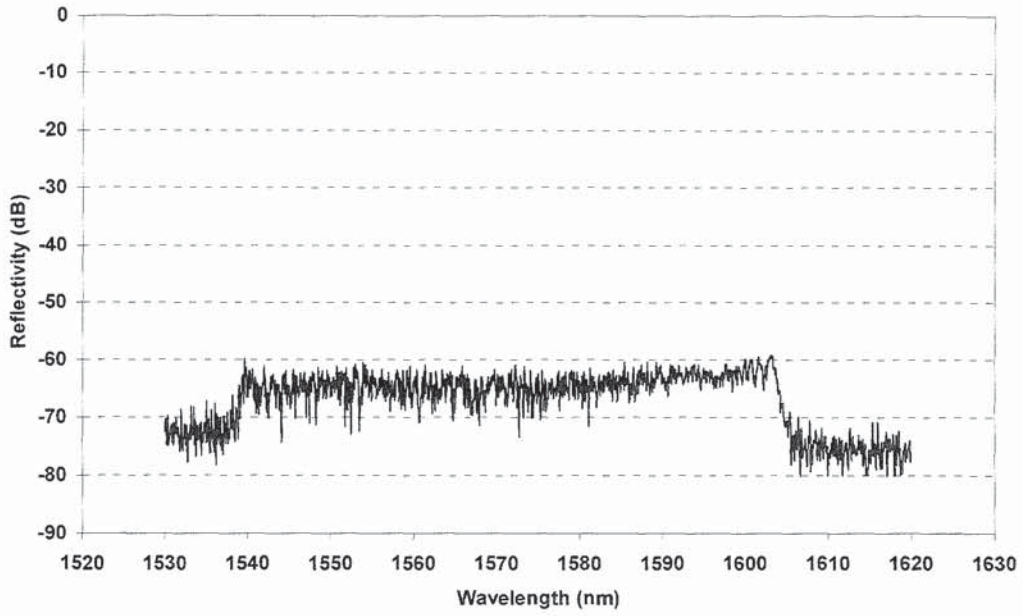

Figure 3-8: Phantom grating written by apodising the entire grating 100%.

By actively varying the voltage across the entire length of the grating the amplitude of the phantom grating was reduced by about half, giving an amplitude of 10dB above the noise floor uniformly across all wavelengths.

The resolution of the apodisation in a chirped grating is proportional to the beam size. A static beam will support the writing of a small range of wavelengths for which the apodisation is only tuned to perfectly apodise one wavelength. To reduce the beam size, a 1 meter focal length cylindrical lens was put into the system to focus the beam in the horizontal axis. The preferred technique would have been to use a telescope to reduce the beam size, however time and financial constraints required an easy and rapid solution. Typically during phase mask based FBG fabrication, horizontal focusing lenses are not used since they can alter the wavelength of the grating written. The 1 meter focal length lens was used as the beam waist is not only small but also the working distance is long. Thus there would be negligible alteration in the wavelength written since the beam can be approximated as being collimated over the distance between the phase mask and the fibre. The phantom grating was repeated again, with the long focal length lens in the system, the results are shown in Figure 3-9.

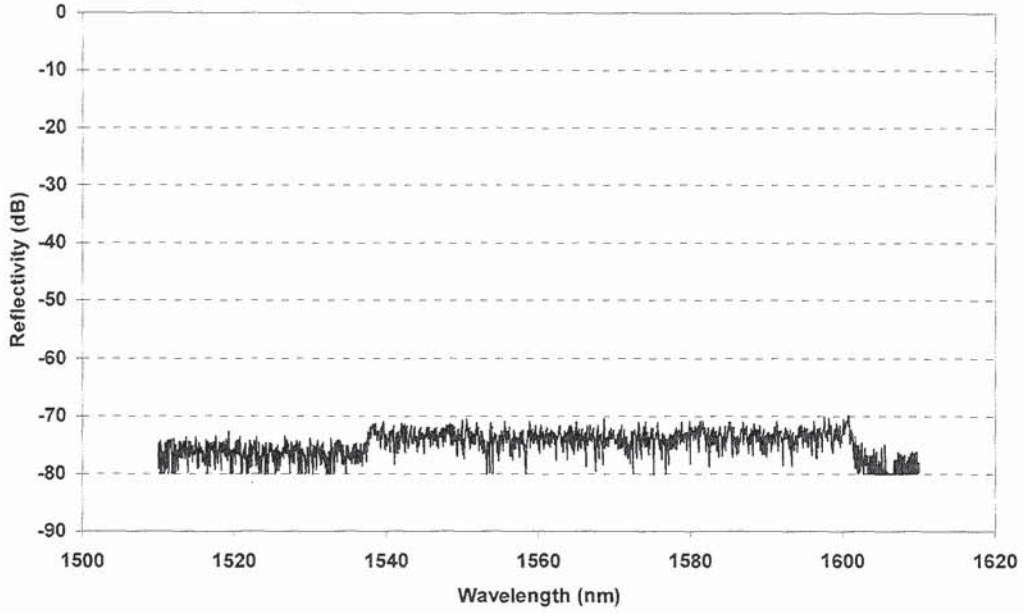

Figure 3-9: Phantom grating written by apodising the entire grating 100% after adding a 1m focal length lens.

The amplitude of the phantom grating reduced with the introduction of the lens, giving an amplitude value of about 5dB above the noise floor, indicating extremely high resolution to the apodisation.

With the improvements made to the apodisation control software the systematic errors in the FBG fabrication were greatly reduced. Attention was therefore turned to more random effects, specifically vibrations causing random amplitude and phase noise. To check the effect of the floating optical table, two identical Gaussian apodised, uniform period FBGs were written, one with the optical table floating and the other with the table sunk, results shown in Figure 3-10.

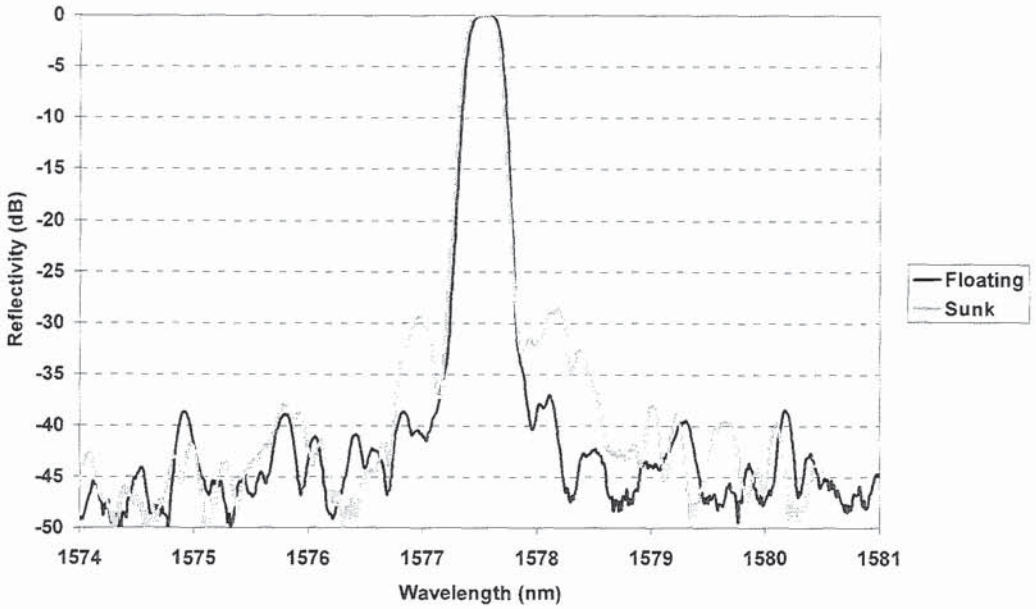

Figure 3-10: Comparison of two Gaussian apodised uniform period FBGs written, one with the optical table floating and one with the optical table sunk.

As predicted by [37] the vibrations coming from the floor passed through the optical table when sunk, causing random phase and amplitude noise, ultimately resulting in higher sidelobes either side of the FBG's Bragg wavelength. The difference of about 7dBs in the sidelobes indicated that the difference in sidelobe suppression could be used for major changes (such as floating the table) but that more subtle changes would probably not be measurable. A large number of FBGs would need to be fabricated to collect a statistically meaningful result. The random nature of the noise can create single non-repeatable variations in the reflection spectra, causing the sidelobe measurements from only one FBG to show behaviour which may not be common amongst a larger number of gratings.

The cause of the random amplitude and phase noise needed to be identified. Consequently, a Fabry-Perot cavity, which is extremely sensitive to external effects, was created by fabricating two FBGs separated by a distance of 2mm in a length of fibre. This fibre was then suspended between the fibre clamps of the FBG fabrication system, where any vibrations experienced by the fibre result in changes to the Fabry-Perot oscillations. A narrow line width laser was set on the

slope of one of the Fabry-Perot spectrum and the amplitude recorded. This temporal amplitude variation was recorded under a number of different scenarios and the Fourier transform taken to give the frequency domain information.

A number of different factors were suspected to cause vibrations on the fibre during the writing process. These factors included the air conditioning system, vibrations from the cooling water entering and leaving the laser and localised air currents around the fibre. Different permutations of having the air conditioning system off, the water off and a box over the fibre clamps (to reduce air currents) were tried and the vibrational information analysed, Figure 3-11.

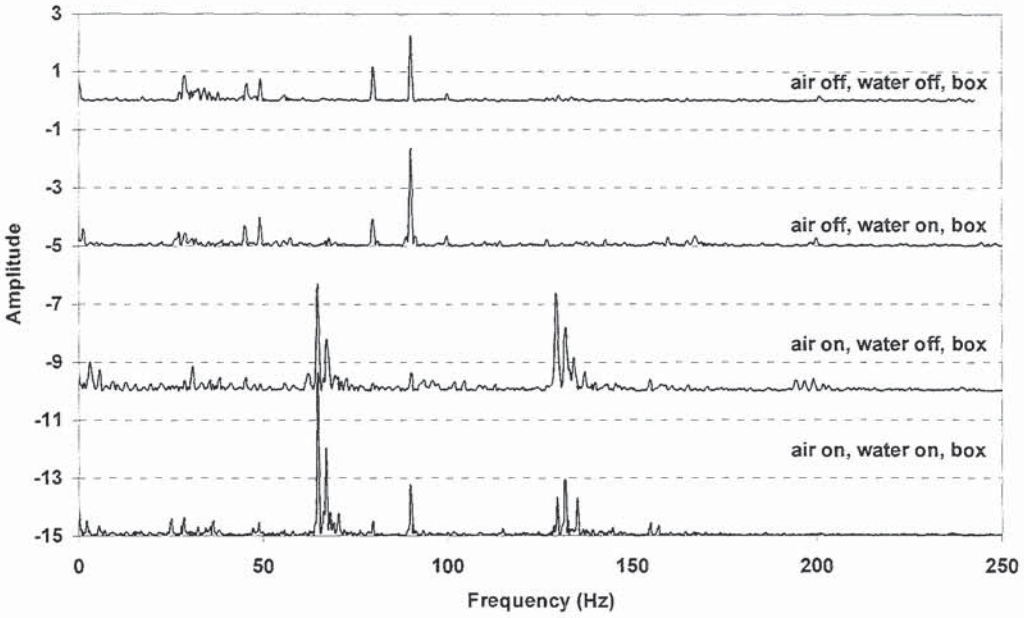

Figure 3-11: FFT from the Fabry-Perot response of a twin grating cavity being held in the fibre clamps.

No obvious effects were shown on the fibre when the water system was switched on and off. When the air conditioning system was switched on and off with the enclosure on, peaks at 65Hz and 130Hz were observed. These were amplified by removing the enclosure; Figure 3-12 shows that the amplitude of the frequency components at 65Hz, 130Hz, 195Hz and 240Hz dramatically increased. The

130Hz and 195Hz peaks are probably second and third order effects from the fundamental peak at 65Hz. This strongly indicates that there are localised air currents around the fibre caused by the air conditioning system. Although the fabrication system had a laser safety enclosure around the outside, it did not fully enclose the table therefore not providing an air tight seal. Any FBGs written would subsequently require a enclosure placed over the fibre.

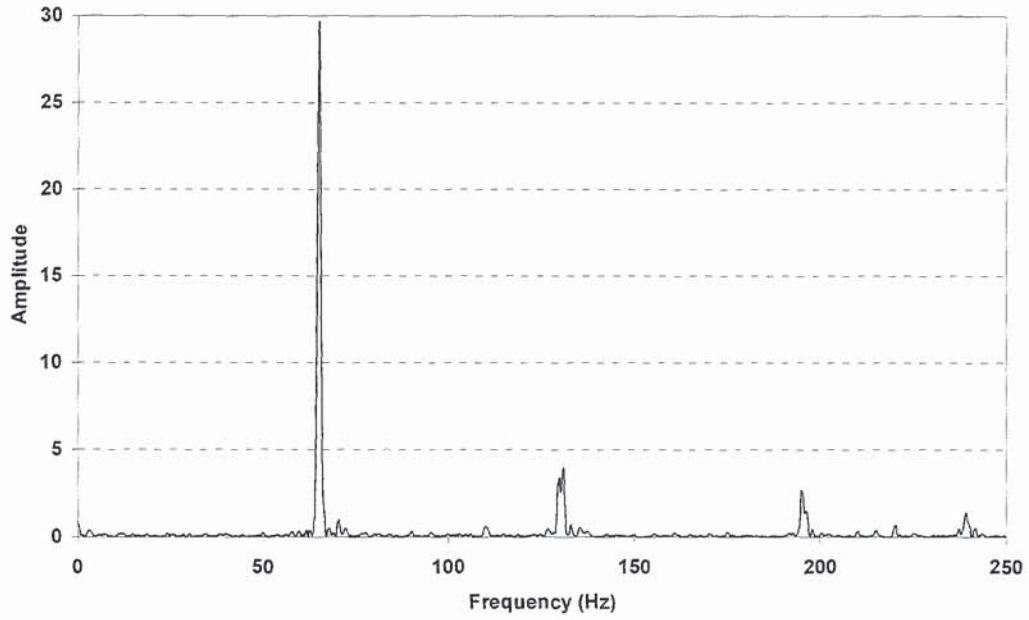

Figure 3-12: FFT from the Fabry-Perot cavity, showing the effect of having the water and air con on but removing the enclosure. Amplitude of the fundamental peak is too large to show on Figure 3-11.

Although the fibre is hugely sensitive to air currents, the optical mounts supporting the mirrors and lenses in the fabrication system are not particularly sensitive to weak vibrations that can be easily damped. Instead, the optical mounts are far more susceptible to vibrations from the optical table which may be amplified by the mount's own structure. In order to detect the sources that can affect the stability of these optical mounts, a Michelson interferometer was set up on the optical table, shown in Figure 3-13.

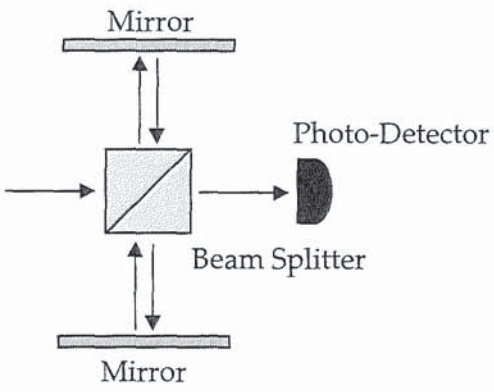

Figure 3-13: Michelson interferometer used to measure vibrations on optical mounts. The three arms of the interferometer were positioned about 25cm from the beam splitter.

Similar experiments to those conducted for the Fabry-Perot system were repeated with the Michelson interferometer setup. The most significant results were detected when switching the water supply to the laser on and off, as shown in Figure 3-14.

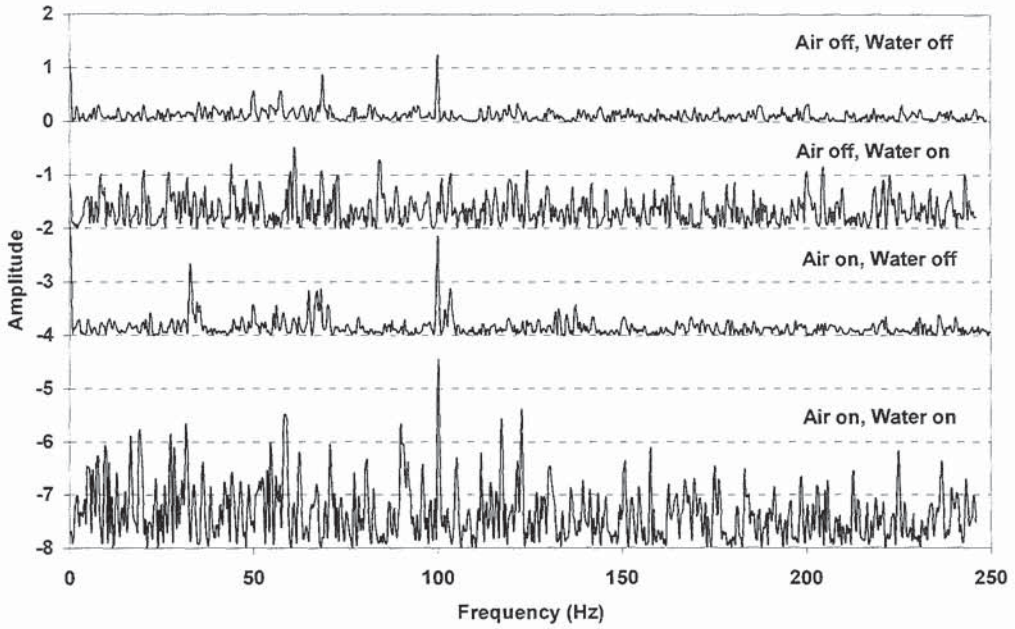

Figure 3-14: FFT from the Michelson interferometer.

These results show that the vibrations induced by the water flowing through the laser caused substantial vibrations on the optical mounts which would directly

affect the beam pointing of the laser onto the fibre. It is also shown that the air conditioning system gives little or no contribution to the vibrations on the optical mounts. The peak at 100Hz was present during all Michelson experiments, suggesting either a natural harmonic of the optical table or measurement system. The broad band nature of the vibrations, due to the water system, is of interest. This suggests that the vibrations were not produced at one point along the table nor by a cyclic device, ruling out any vibrations directly from the water pump. These vibrations are suggested to originate from all positions along the water path including the tubing and routing within the laser. To give a general feeling for the magnitude of these vibrations, Figure 3-15 shows the effect of lightly tapping the optical table with a finger.

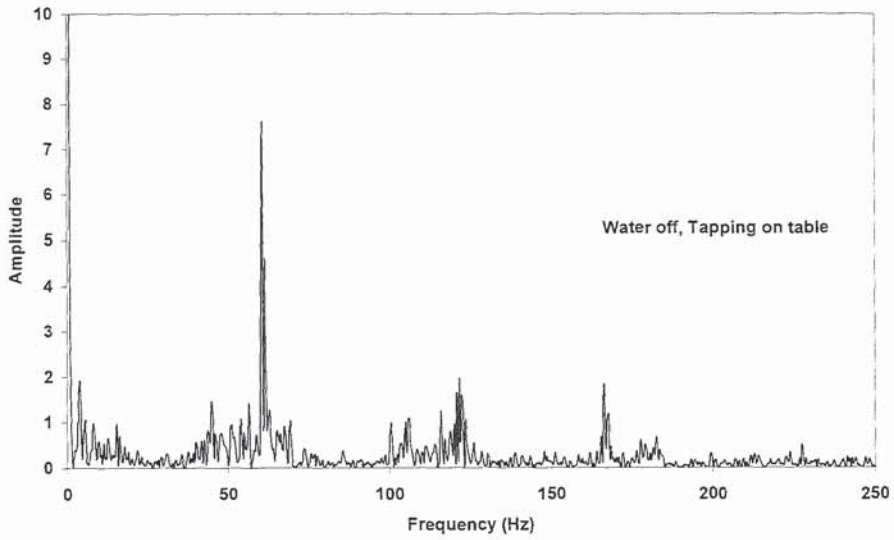

Figure 3-15: FFT from Michelson interferometer, showing the effect of tapping the table. [Amplitude of fundamental harmonic to large to plot on Figure 3-14.]

After the Michelson interferometer results were analysed, it was decided to place the laser on rubber feet to damp the vibrations from the water system within the laser. The experiment was repeated, results shown in Figure 3-16.

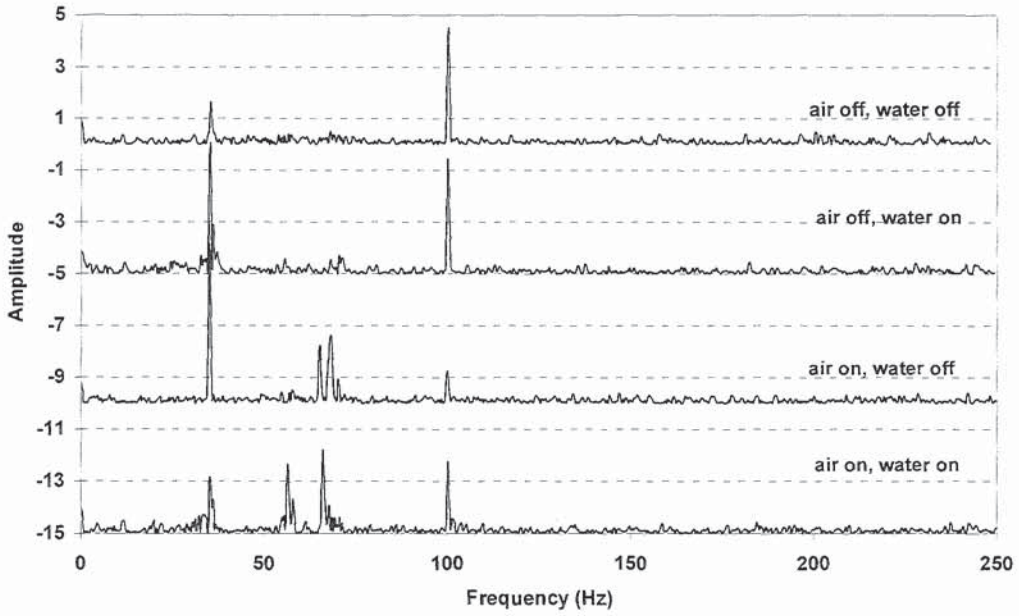

Figure 3-16: FFT of Michelson interferometer after installation of rubber feet under the laser.

After inserting the rubber feet, little vibrational difference was seen with the water system on or off. However, now that the noise level was reduced, peaks could be seen due to the air conditioning system albeit of a relatively low intensity.

Since any vibrations ultimately affect the beam pointing of the laser in reference to the fibre, it was a natural requirement to look at the beam pointing stability of the laser. A four segment photo-detector, shown in Figure 3-17, was used to trace the route of the beam over a similar time it takes to write a GTE.

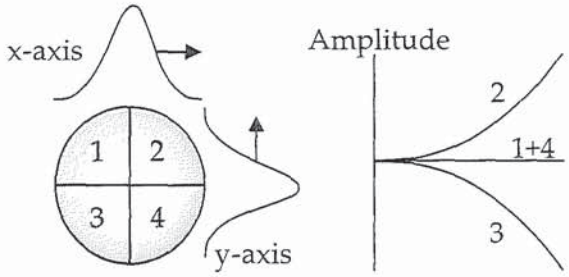

Figure 3-17: Four segment photodetector used to trace the beam pointing of the laser, showing the response of the four quadrants if the beam was to drift up and to the right of the detector.

As the beam tracked across the face of the photo-detector, the amplitude response of each quadrant changed relative to the intensity of light incident across the quadrant area. The change in amplitude response of each quadrant, relative to one another, can be used to trace out the route of the laser beam. The laser came with two control options, 'Power Track' and 'Light Regulation', which manage the laser so that the output power of the laser cavity is maintained. Power Track optimises the position of the laser cavity mirrors for maximum power output at a set laser cavity current. Light Regulation automatically varies the current on the cavity to give a stable power. Both of these settings can effect the pointing of the laser. The beam was monitored over a period of 60 seconds with different combination of Power Track and Light Regulation activated, as shown in Figure 3-18.

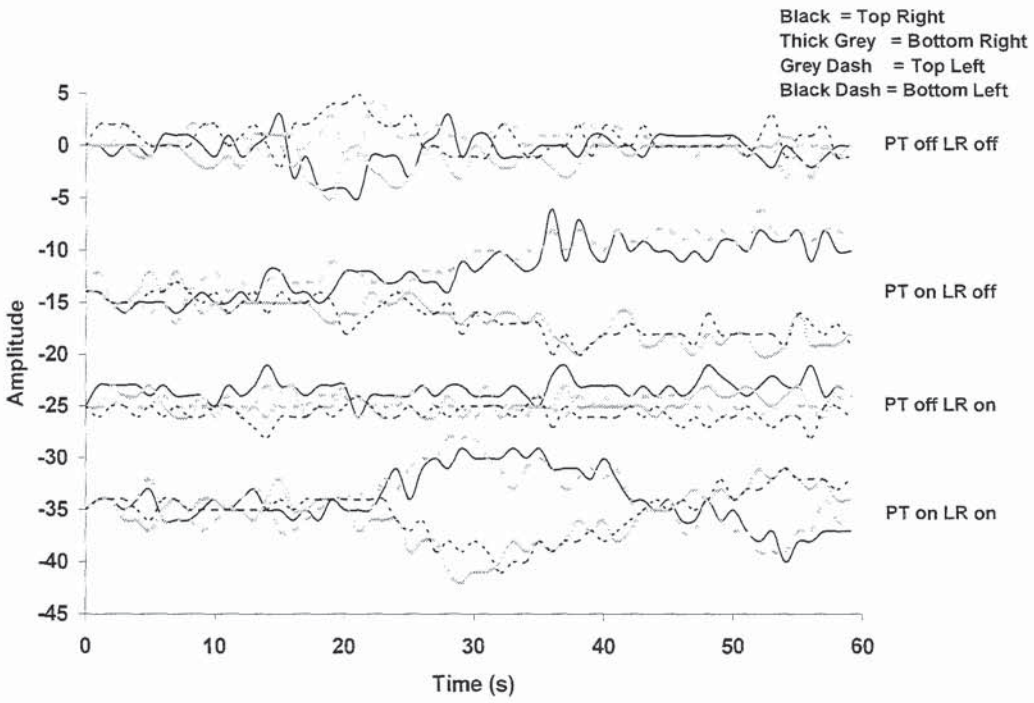

Figure 3-18: Relative amplitudes of the photo-detector quadrants as the beam pointing drifted under different Power Track (PT) and Light Regulation (LR) combinations.

The results showed that the best combination was to have the Power Track switched off and the Light Regulation on. PT creates beam instabilities due to the alterations of the cavity path. The technique of turning off the PT and leaving on the LR was not adopted since the laser could ramp the current to dangerous levels, potentially damaging the laser. Subsequently, despite the beam pointing stability, LR was not used for fabricating FBGs beyond this study.

In order to quantitatively compare the different improvements, a number of GTEs were fabricated after each improvement. The requirement for a high quality GTE was to have each consecutive dispersion peak of the same amplitude when measured from the zero point of the localised dispersion. Although the peaks are simplistic to detect, the turning points are difficult to detect accurately due to a small level of noise. Therefore the group delay traces were used instead, as shown in Figure 3-19.

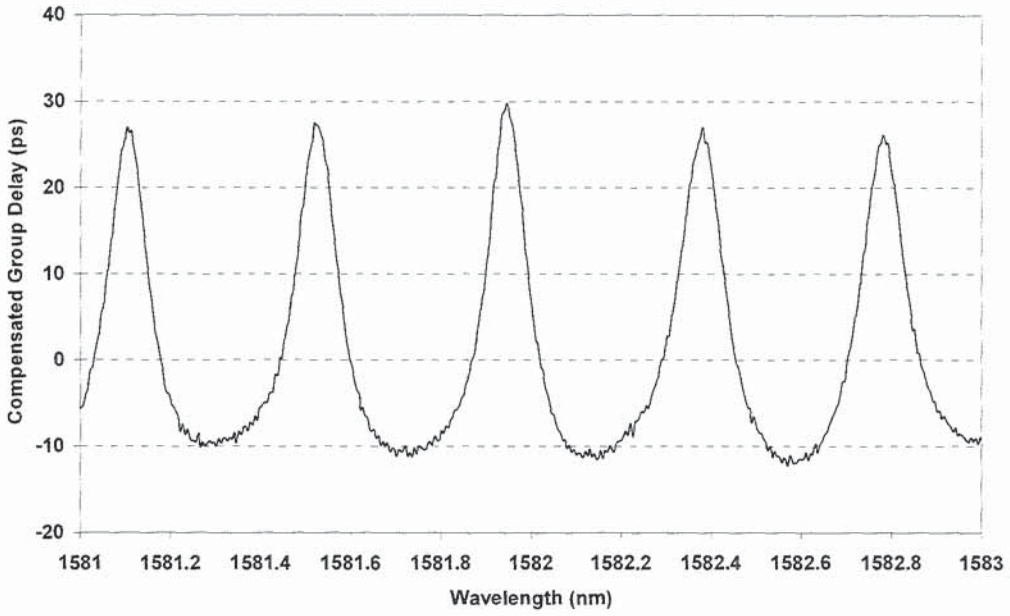

Figure 3-19: Group delay for a GTE after slope compensation.

These measurements were made using an Agilent Dispersion Measurement kit, the gratings were measured in reflection from the short wavelength end.

The group delay of a GTE has a specific slope related to the chirp rate of the grating. To accurately compare the peaks at every wavelength this slope was compensated for when analysing the data. The amplitude of the peaks and the troughs were recorded over the entire bandwidth of the GTE and converted to a histogram. The histogram was set up so that the number of data points at each peak or trough amplitude was recorded, in bin sizes of 1 unit. From this histogram a normal distribution could be fit to give the standard deviation of these peaks and troughs, the lower the value the higher the quality of the grating. They show the cumulative effect of applying each improvement in turn. These histograms are displayed from Figure 3-20 to Figure 3-24.

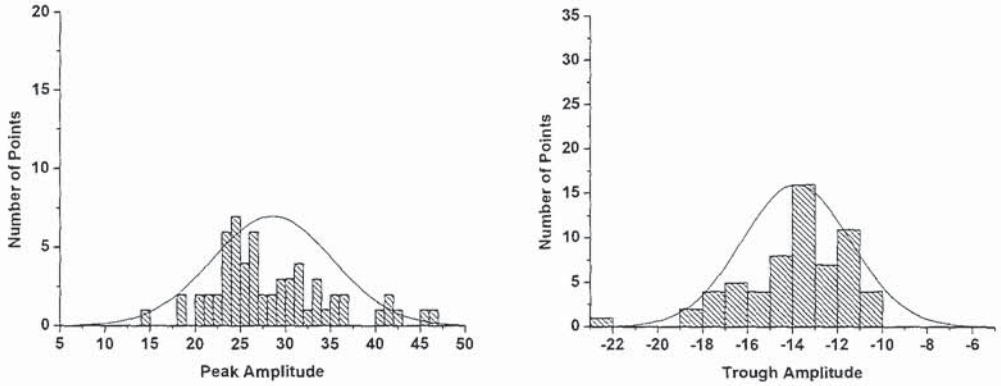

Figure 3-20: GTE analysis prior to system improvements.

The trough amplitudes have a higher number of data points per bin than the peak amplitudes as the trough has a slower turning point. The wide spread of peak amplitudes for the GTEs prior to system improvements is a good indication of the lack of control over the random phase and amplitude fluctuations induced in the refractive index of the fibre.

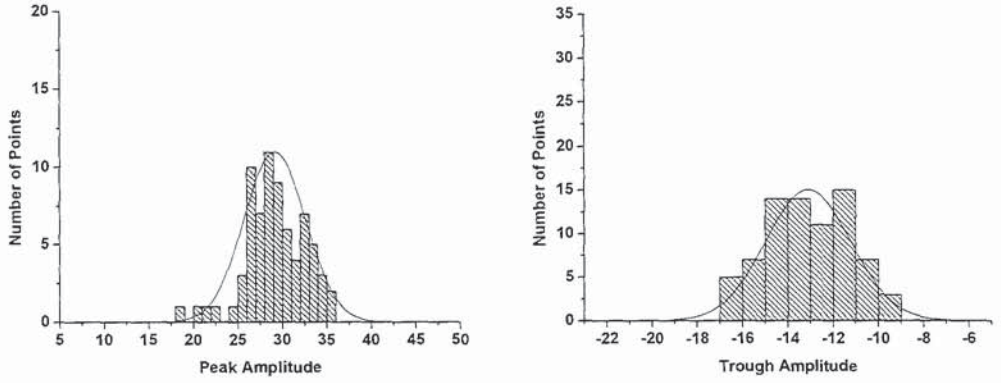

Figure 3-21: GTE analysis after the piezo control software was updated.

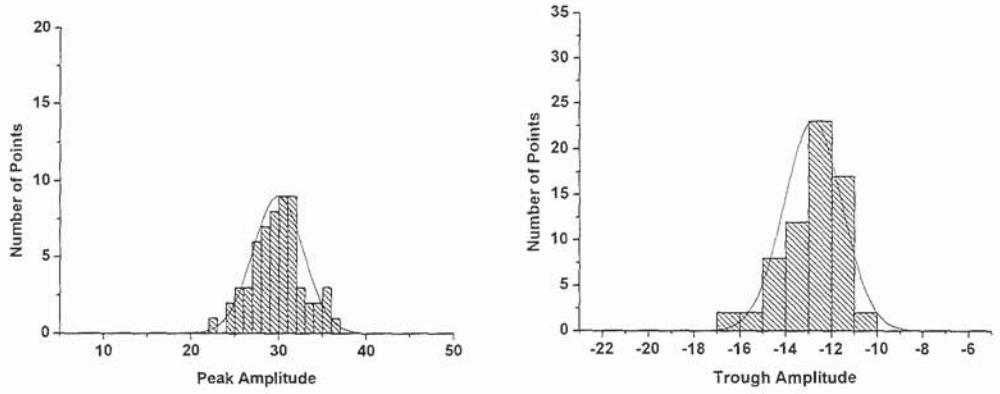

Figure 3-22: GTE analysis after the long focal length lens was inserted.

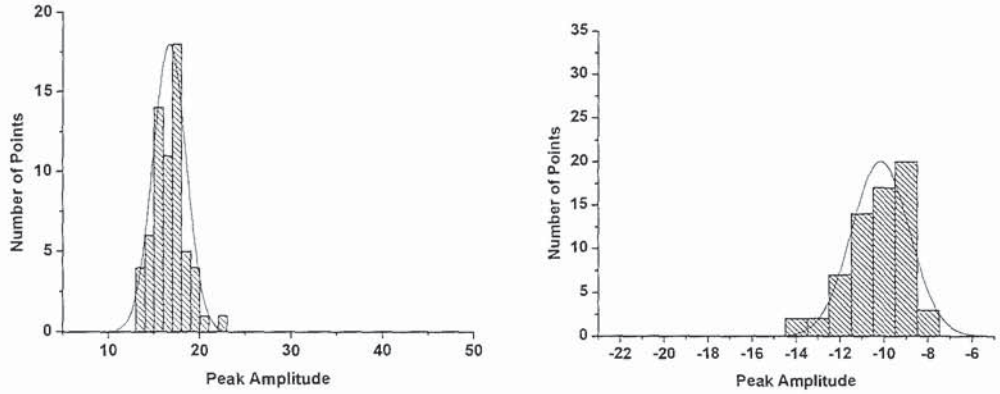

Figure 3-23: GTE analysis after the rubber feet were placed under the laser.

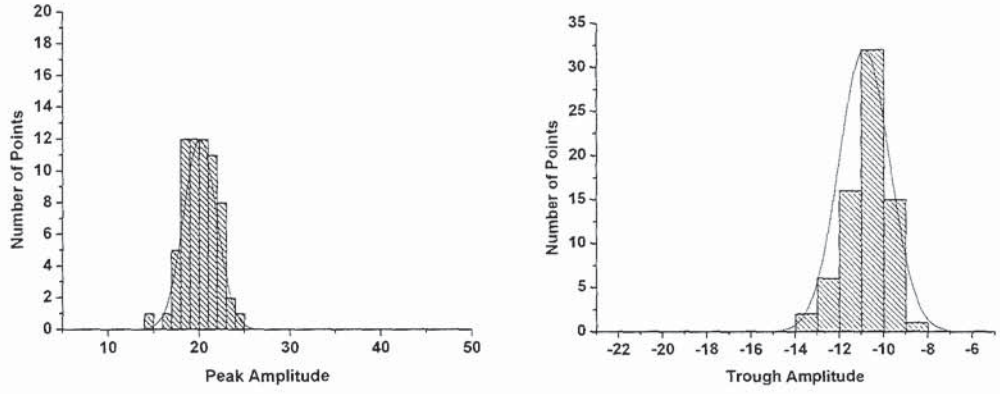

Figure 3-24: GTE analysis after writing gratings with Power Track off and Light Regulation on.

The standard deviation of each normal data fit was recorded in order to directly and quantitatively compare each improvement, as shown in Figure 3-25.

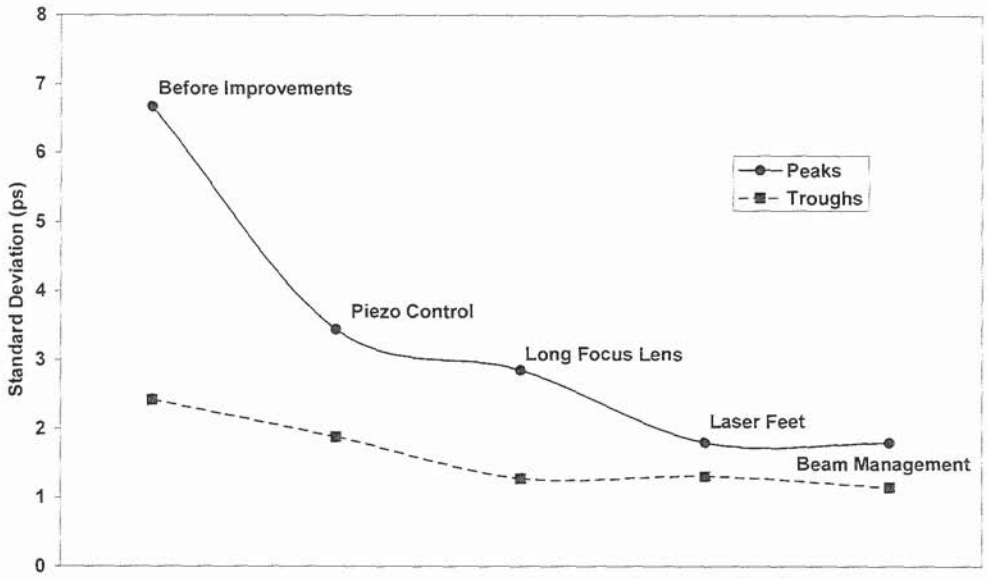

Figure 3-25: Reduction in standard deviation of group delay peaks and troughs as improvements were applied to the fabrication system. Points plotted in chronological order.

The largest single improvement was obtained from improving the voltage feed back for the piezo control system followed by the laser feet, long focus lens and then the beam management. These results are slightly skewed as the improvements are shown in chronological order. As time progressed the general understanding, knowledge and handling of the GTEs increased thus naturally allowing marginal improvements to be introduced.

The quality of grating fabrication has been demonstrated to be grossly reliant on the control system, laser beam and environmental factors. Through systematic elimination of these factors, the grating quality was shown to improve significantly, enabling a professional quality telecommunications device to be produced. All of the improvements, for the exception of the beam management suggestions, were applied to the fabrication of the GTEs. The team at Indigo managed to manufacture a GTE module which was capable of compensating dispersion between ± 300ps/nm over a majority of the C- and L-band with a group delay bandwidth of 25GHz.

3.2 Direct Write System

3.2.1 Introduction

Despite the impressive results gained from the scanning phase mask system, a different type of FBG manufacturing system was also required by Indigo. As telecoms systems grew, the channel spacing became more squeezed, requiring narrower bandwidth gratings to perform add/drop and mux/demux applications. The scanning phase mask technique has one fundamental flaw; the length of the FBG is ultimately limited by the length of the phase mask. In order to fabricate ultra narrow FBGs they potentially need to be up to 10cm in length. Although it is possible to purchase long phase masks, their quality reduces due to limitations in the holographic methods used to fabricate the masks. Naturally, the cost of a phase mask also rapidly increases with length. In order to overcome these limitations a highly versatile system was designed, termed a direct write system, allowing 10cm FBGs to be written with any arbitrary apodisation function. The technique was based on that proposed by [39] where a number of small identical FBGs are stitched together by modulating the beam passing through a static phase mask and moving the fibre. By carefully controlling the motion of the fibre, nanometre position resolution is possible, allowing the FBGs to be stitched together on a fringe by fringe basis maintaining a constant phase. Control down at this level allows the relative phase of each peak to be adjusted, resulting in the possibility of reduced visibility and increased fringe, ultimately leading to apodisation and chirping of the grating.

The direct write system was primarily set up and developed by John Mitchell, from Indigo Photonics. A large amount of development had been completed before my involvement with the fabrication system. My role was to help incorporate and quantify any improvements learnt from the previous work on the scanning phase mask system and to then exploit the full capability of the system.

3.2.2 Optical Design

To achieve a rapid modulation of the beam, an acousto-optic modulator (AOM) was inserted into the beam path of the laser, Figure 3-26. The AOM sends an acoustic wave through the material within the modulator as the laser beam passes through it. Diffraction is caused by the interaction between the light and the acoustic wave, splitting the beam. Along with the AOM, the optical system also used a 244nm Coherent Sabre FreD laser, static phase mask and a translation stage holding the fibre. The Sabre FreD was required rather than a standard FreD laser since it can provide up to 500W output. This extra power is required as the AOM reduces the amount of power available on the fibre, partly due to the duty cycle effect and also due to the splitting efficiency of the beam through the AOM. The translation stage was a high precision air bearing stage provided by Danaher Precision Systems. Due to the high stability required to stitch together sub-micron fringes, the air bearing stage was essential to provide not only the position control but also the vibration isolation from the table. In order to aid the alignment and reduce human error, a camera system was placed over the phase mask to monitor the distance between the fibre and the phase mask. This ensured that there was no distance variation between the two when scanning the fibre, which could otherwise result in a weaker section of the grating towards one end.

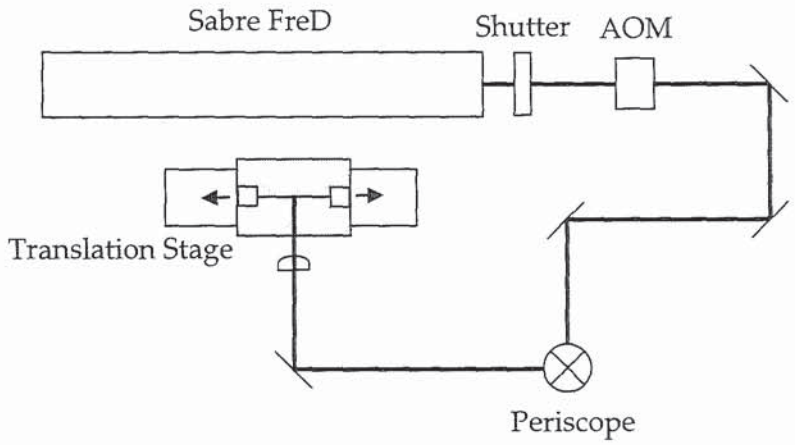

Figure 3-26: Schematic of the direct write setup.

The system was designed so that the operator could use a graphical user interface (GUI) on a PC and load up an ASCII data file. The file would contain information on the FBG profile, including the required apodisation shape with distance along the grating and the chirp rate. On the GUI the operator could then choose the required stage scan speed and the phase mask period being used. The system could then be aligned by the camera system for fibre-phase mask alignment and by eye for beam-fibre alignment. Upon execution, the GUI downloaded a data file to a single board computer (SBC) which then monitored and controlled the stage and AOM. The reason for the SBC was to prevent any background operations on the PC from interfering with the AOM modulation timings. Such interference would result in slight time jitters creating lower quality gratings.

The direct write system is fundamentally different to the scanning beam/phase mask technique. As the phase mask and the beam are static the beam needs to be modulated to allow sub-gratings to be 'stitched' together. If the modulation did not occur, the refractive index profile would be blurred out, giving a uniform profile and thus no grating. Therefore the duty cycle required to give a specific refractive index response is important to calculate. Assuming the interference profile behind the phase mask, $i(z)$, to be

$$i(z) = A\cos\left(\frac{2\pi}{\Lambda}z\right) \tag{3-4}$$

Where A is the amplitude of the profile. The visibility of the grating fringes will be defined by the intensity pattern which the fibre is exposed to over the exposure period. If α is the duty cycle, varying between 0 and 1 then the exposure period can be stated as $\alpha\Lambda$. Thus the refractive index, $n\ z$, at any point along the grating my be given by

$$n(z) \propto \int_{\beta=0}^{\alpha\Lambda} A\cos\left(\left(\frac{2\pi}{\Lambda}\right)(z-\beta)\right)d\beta \tag{3-5}$$

Which may be rewritten as

$$n(z) \propto \frac{A\Lambda}{\pi}\sin(\pi\alpha)\cos\left(\frac{2\pi}{\Lambda}\left(z-\frac{\alpha\Lambda}{2}\right)\right) \tag{3-6}$$

To get a maximum fringe visibility α, the duty cycle, should be set to 0.5 and for the minimum visibility set to 1. This therefore shows how the method can be used to apply an apodisation profile to the grating. The apodisation is achieved by printing consecutive sets of fringes out of phase with one another. When the fringe amplitudes are summated the peak to trough amplitude visibility is reduced, leading to a lower reflectivity of the grating and a higher level of apodisation. In order to ensure that the phases of the summated peaks are all in phase across the length of the grating, both positive and negative dephasing must take place. If an initial fringe is written, then the next two fringes must be imprinted with a certain positive and negative phase offset, as shown in Figure 3-27.

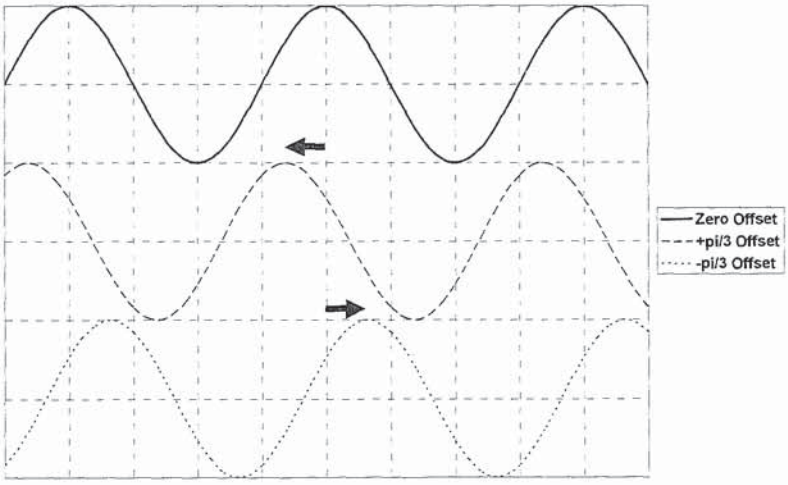

Figure 3-27: Relative phase positions of three fringe patterns to allow apodisation.

The opposite phases allow the peak, of the summated fringe pattern, to be maintained in the original phase, as shown by Figure 3-28. The level of apodisation is directly given by the amplitude of dephasing, if the fringe pair is written $\pm\pi/2$ out of phase then the reflection contribution from that fringe pair will be zero.

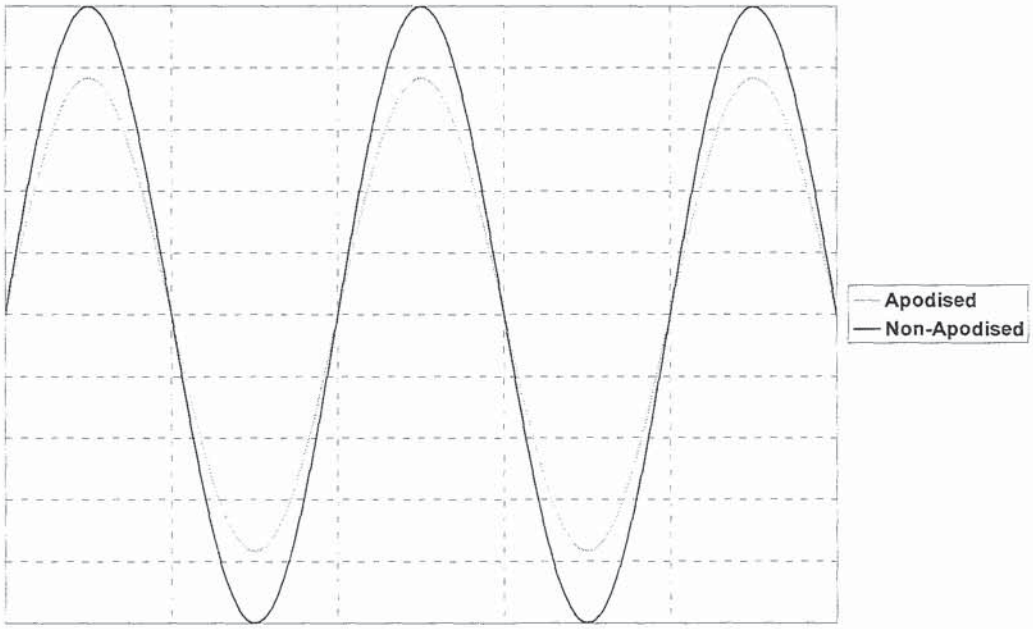

Figure 3-28: The effect of summating the three dephased fringe patterns shown in Figure 3-27, allowing a higher apodisation. The non-apodised graph is summated over three in-phase fringe patterns.

If this technique of negative and positive phase compensation is not applied and instead the phase is allowed to progress in a linear fashion, as in Figure 3-29, then a chirp effect will be introduced.

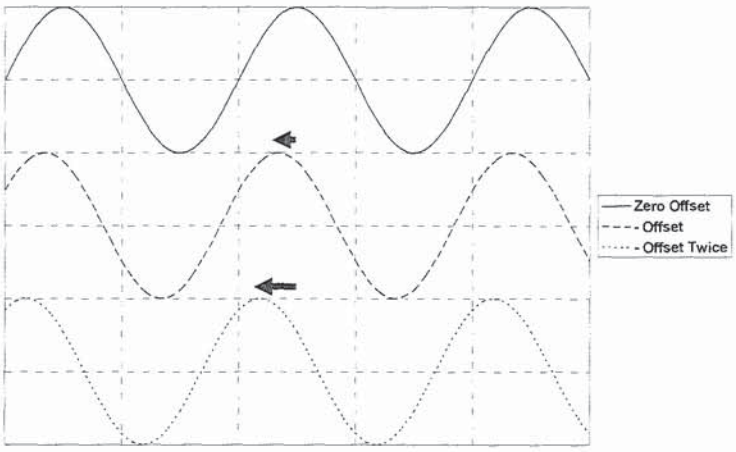

Figure 3-29: Linear dephasing of the fringe patterns.

As the phase progresses, the fringes at the start of the grating will be written with a different phase to those at the end. The fringes are linearly dephased as the grating is written, giving a positional dependency to the phase. This ultimately leads to a chirp effect where the fringes at the beginning of the grating will support higher wavelength reflections than those at the end. Figure 3-30 demonstrates how this phase progression alters the relative phase of the summated fringes.

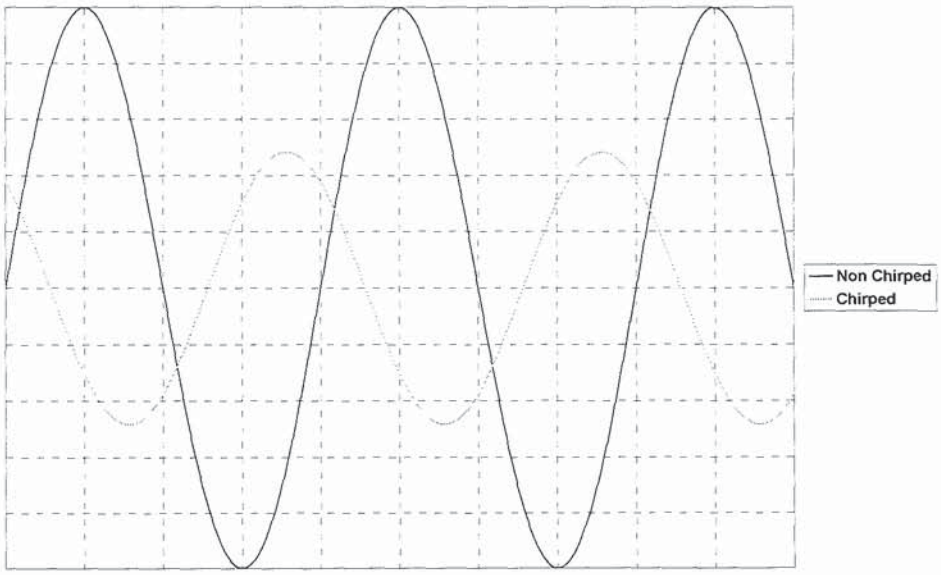

Figure 3-30: The effect of linearly dephasing three fringe patterns, in comparison with the summation of three in-phase patterns. The dephasing leads to a chirp effect.

As with the apodisation method, the effect of the phase progression leads to a lower fringe visibility. Subsequently, the larger the chirp effect, the higher the level of intrinsic apodisation. This strongly limits the effective range for which chirping can occur.

Both the apodisation and the chirp are strongly affected by the beam size. The direct write method writes thousands of fringes per shot, so a central section's fringe visibility will be made up by the summation from thousands of shots as the beam progresses across that area. This summation causes the localised resolution of the apodisation or chirp to be reduced since there will be numerous other phases present at each position, effectively creating a blurring of the refractive index profile. The minimum distance to progress from zero to maximum apodisation would be equivalent to the width of the beam. This therefore feeds errors into the grating profile, moving it away from the perfect spectra. For more information on apodisation refer back to chapter 2.5.3.

3.2.3 System Improvements

As improvements to the direct write system were implemented, a series of uniform period, 25dB strong, Gaussian apodised FBGs were fabricated. These gratings were analysed by looking at the sidelobe suppression in their reflection spectra. Previously, the concept of using sidelobe suppression as a measure of improvement had been discounted; the phantom gratings had been used instead. Due to the chronology of the work conducted, the concept of using the phantom gratings had not been conceived until half way through the direct write development, resulting in sidelobe analysis being conducted in this section.

Two major improvements were made to the system, the Sabre FreD laser was placed on rubber feet, effects shown in Figure 3-31 and a enclosure was placed around the translation stage, encompassing the final mirror, phase mask and fibre as shown in Figure 3-32.

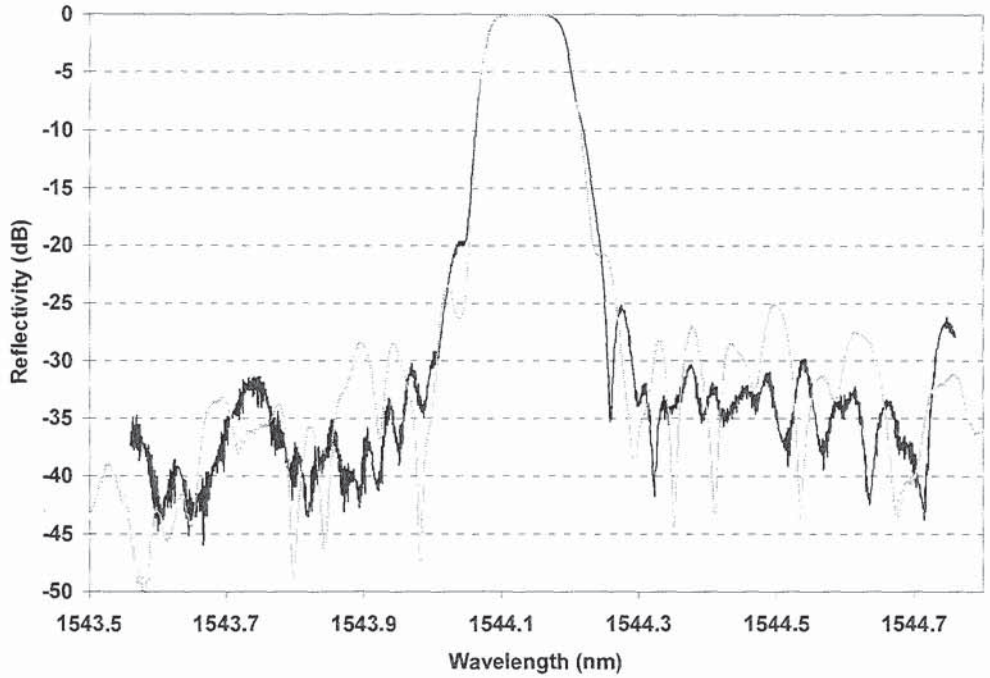

Figure 3-31: Comparison of two 25dB strong, identically Gaussian apodised FBGs, one written before the rubber feet were inserted below the laser and the other after the installation. Grey line showing the FBG before the laser feet and black line after.

The installation of the laser feet showed a general improvement of the sidelobe level of around 5dB. Due to the fibre being mounted on the air bearing stage these improvements are probably due to reducing the vibrations on the mirror and lens mounts instead of reducing the vibrations on the fibre. The air bearing stage damps many vibrations from the table. The vibrations on the fibre were reduced by introducing a large enclosure around the translation stage. The preference would be to have as small a enclosure as possible to reduce any air currents but the fibre mounted to the stage required a large enclosure to be used. The disadvantage is that the stage will create air currents by its movements; however any thermal convection currents from the laser and any currents due to the air conditioning system are decoupled from the fibre.

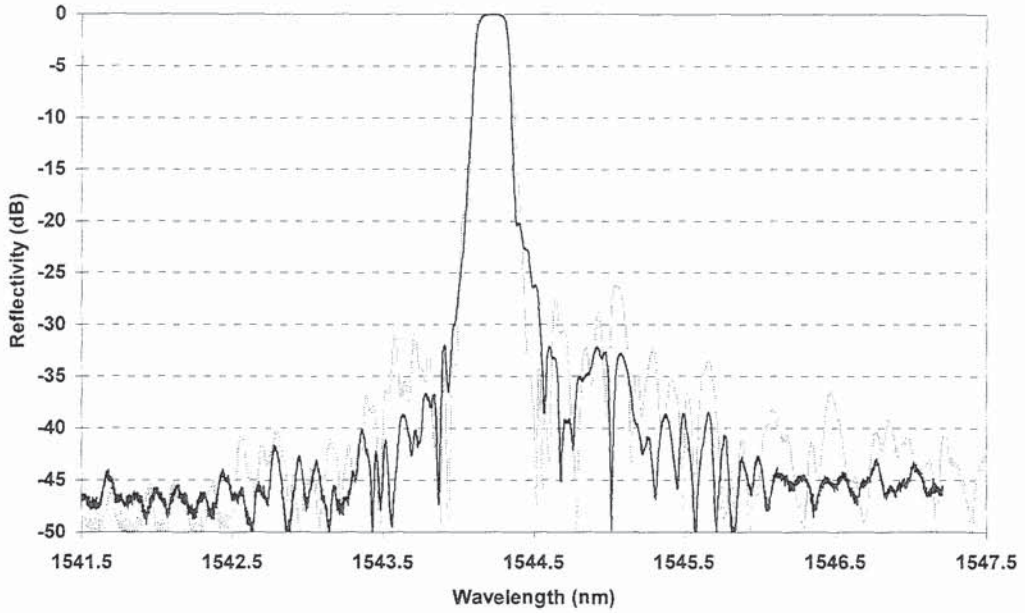

Figure 3-32: Comparison of two 25dB strong identically Gaussian apodised FBGs fabricated before and after an enclosure was installed around the translation stage.

Despite the size of the enclosure significant improvements were observed, a further 5dB sidelobe suppression was obtained. The more rapid drop of the sidelobes towards the noise floor of around -45dB (after trace normalisation) is also indicative of a higher quality grating.

3.2.4 System Capability

To investigate the range of operation for the direct write system, a matrix of gratings at certain lengths and scan velocities was initiated. Gratings were fabricated between 10 and 300μm/s and lengths of 5 to 95mm long. The gratings were fabricated with a Gaussian apodisation then the transmission and reflection spectra were measured after fabrication. The transmission strengths for these FBGs are recorded in Figure 3-33.

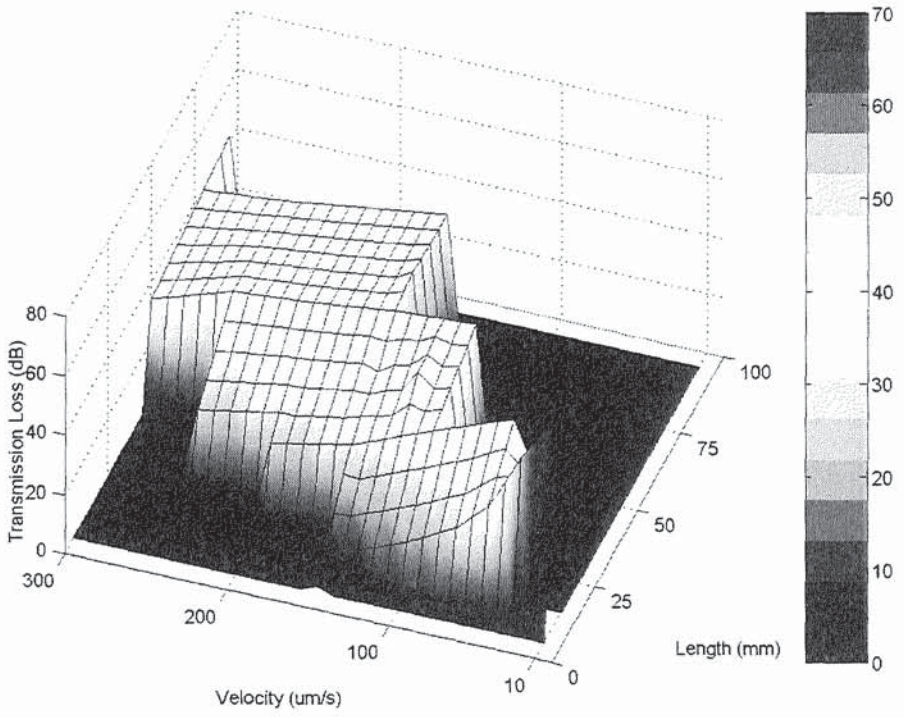

Figure 3-33: Matrix of capability for the direct write system.

The matrix results clearly show that at slow velocities and at long lengths, the grating strength increases. The length was limited to 95mm by the distance between the fibre holding posts mounted on the translation stage. It would have been possible to extend these further but at the sacrifice of grating quality, longer fibre lengths would have allowed the fibre to move more due to sag in the fibre.

Chirped Gratings

Chirped gratings were fabricated to see how much the roll-off in the amplitude, due to dephasing, would affect the gratings. Two different chirp rates were written, one to give a 2.5nm wide FBG and one to give a 5.5nm FBG as shown in Figure 3-34 and Figure 3-35 respectively. Neither grating was apodised so that the roll-off from the dephasing was not confused with any smoothing due to apodisation.

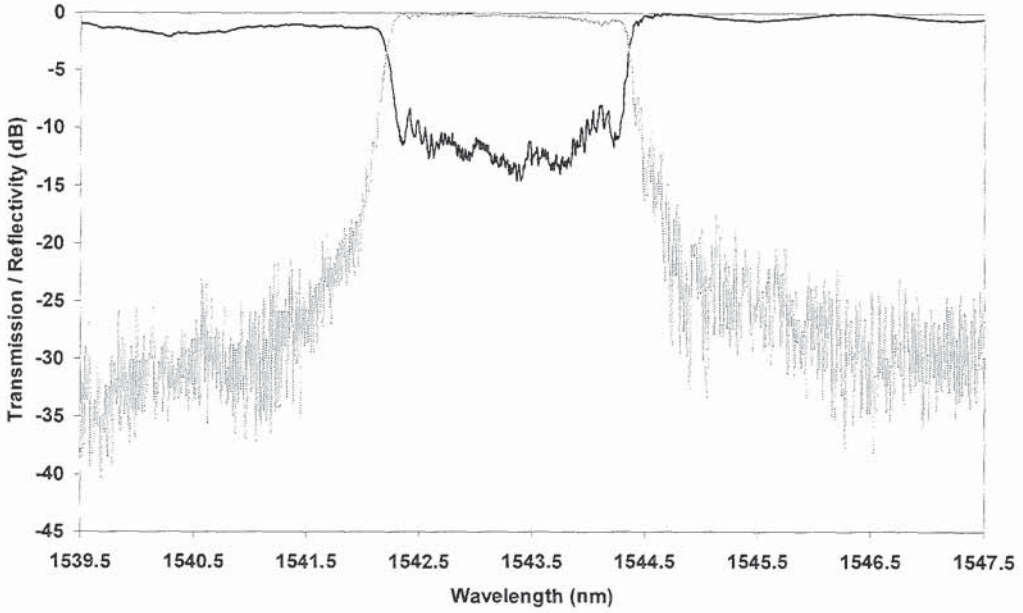

Figure 3-34: 2.5nm wide non-apodised chirped FBG.

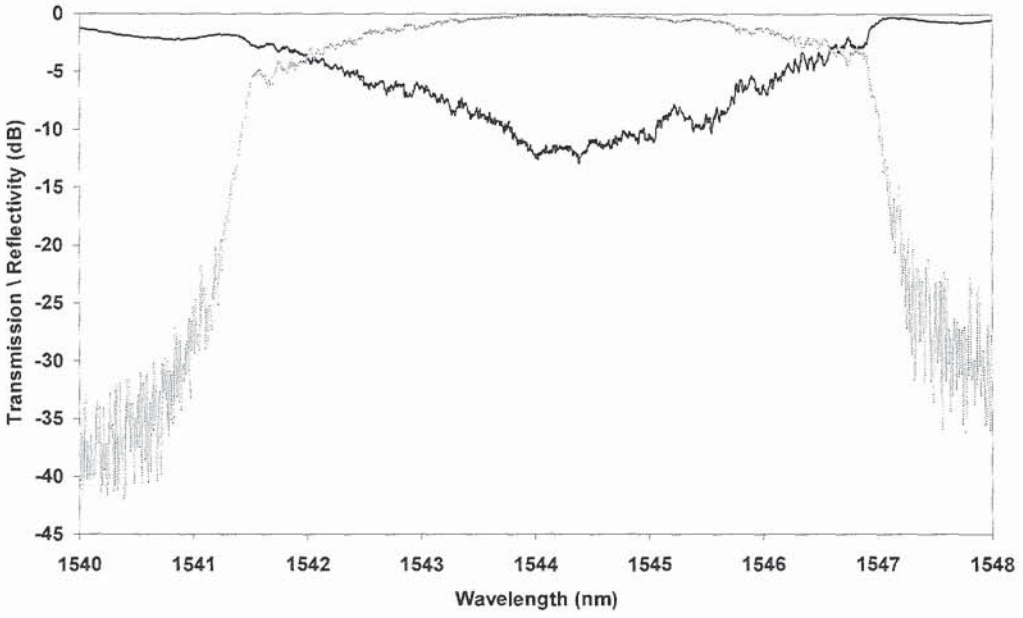

Figure 3-35: 5.5nm wide non-apodised chirped FBG displaying roll-off due to dephasing.

The loss in amplitude due to the detuning is shown to be significant in Figure 3-35. The reflectivity of the grating drops from a peak of greater than 90% to about 68% reflectivity at ±2nm from the peak. Such a drop would not be acceptable in a commercial product where uniformity can be a key factor. Subsequently, the system's practical chirp limit is about ±1nm. The drop off in

reflectivity can be compensated by scanning the grating slower at the edges. However, there was not enough time to calibrate and rewrite the control software to account for this. Although this limitation is a hindrance, it can act favourably for apodised chirped structures. Dr T. Allsop from the Photonics Research Group at Aston University required a novel grating structure which formed a two-peaked chirped sinusoid in the reflection spectra, as shown in Figure 3-36, for a heterodyne sensing technique[40]. The detuning roll-off aided the apodisation outside of the main grating regions which helped reduce the sidelobes.

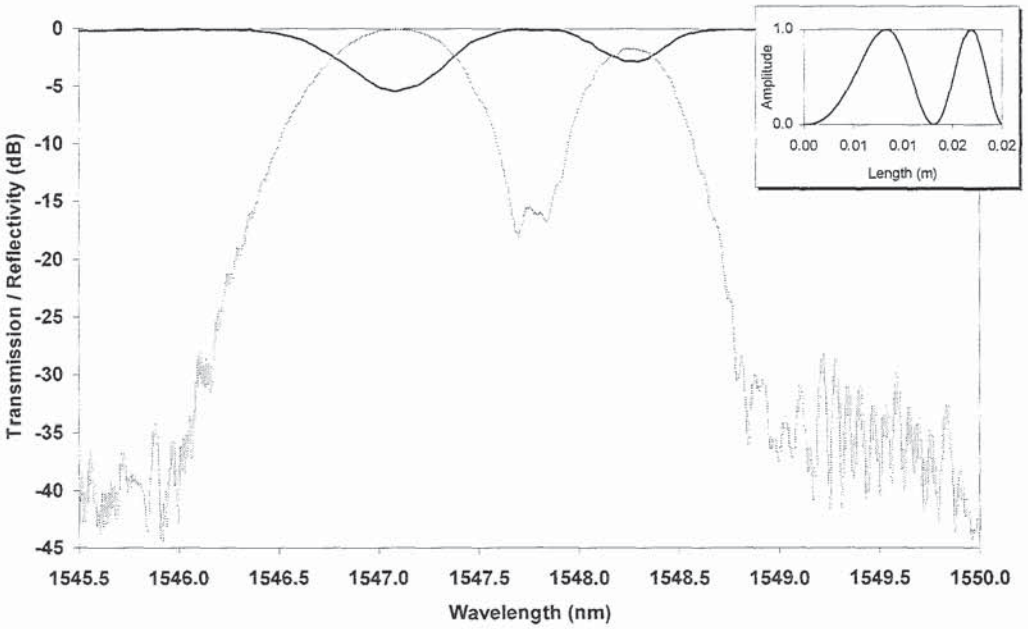

Figure 3-36: Chirped sinusoid reflection spectra fabricated from an apodised FBG. The apodisation profile is shown in the top right-hand corner.

This grating utilised both the chirp and the apodisation capabilities of the system. The region between the two peaks is due to sidelobe interference between the two grating structures. The chirp rate was high enough to avoid any significant Fabry-Perot oscillations between the two structures.

Moiré Gratings

The system incorporated a strain gauge on the fibre holder, allowing not only highly repeatable strains to be applied to the fibres but also to allow strain tuning of gratings. One example of this is the fabrication of a chirped Moiré FBG, Figure 3-37.

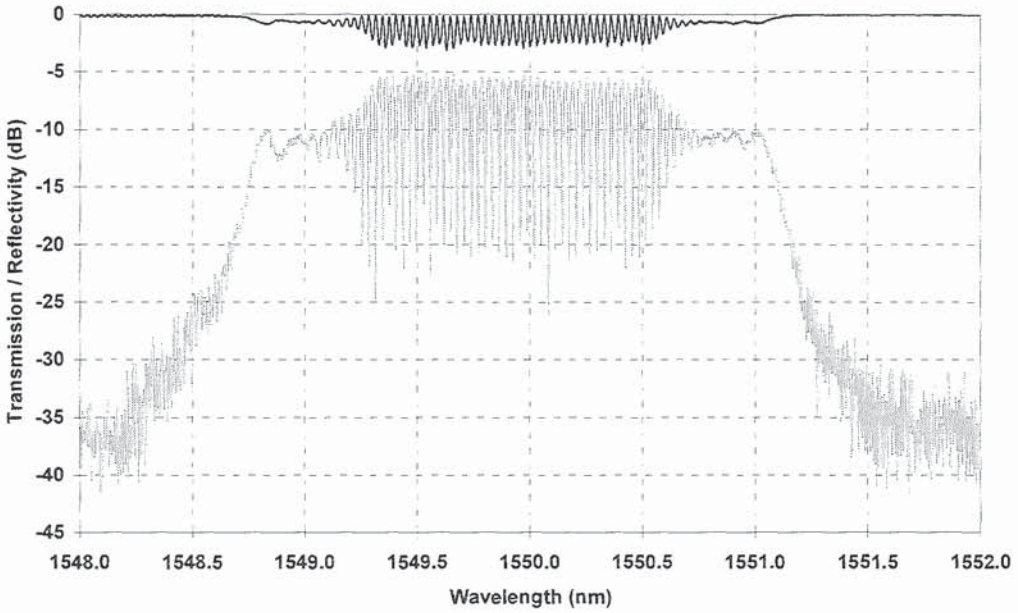

Figure 3-37: 100mm long chirped Moiré FBG, written with a double pass-strain method.

Moiré structures can be made by fabricating one FBG, straining the fibre then writing an identical FBG over the initial one. This technique is known as a double pass technique, Everall [41] showed that this technique could also be used with two chirped FBGs. There are numerous uses for such gratings; this shall be discussed in detail in Chapter 5.

Arbitrarily Apodised Gratings

The strongest advantage of the direct write system is the ability to write any arbitrary apodisation function. One manifestation within the system is that if a refractive index profile is provided that passes from a positive to a negative

value, or vice versa, a localised phase shift is created. This is caused by the zero amplitude being created by the consecutive exposure positions being perfectly out of phase with one another. The sinusoidal fashion of the refractive index being written is effectively flipped at a zero amplitude point, giving a phase shift between the segments before and after the flipping point. A sinc refractive index profiled grating, with a Gaussian envelope was fabricated to emphasise a grating made up of phase shifted elements, as shown in Figure 3-38.

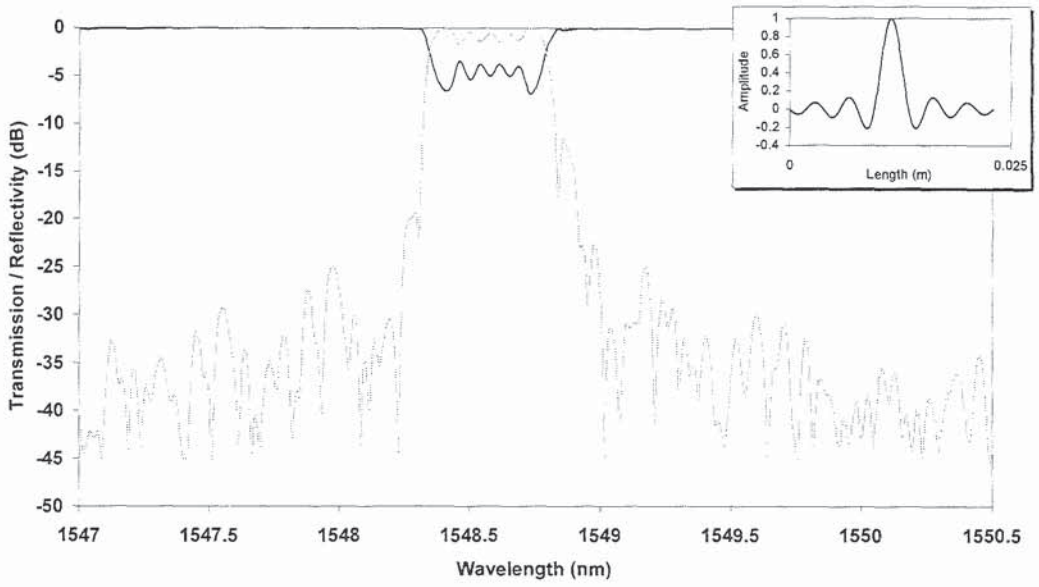

Figure 3-38: 23mm long Gaussian-sinc apodised FBG. The apodisation profile is shown in the top right-hand corner.

These phase shifted elements allow greater manipulation of the FBG spectra than non-phase shifted gratings. The response of the gratings can be made to be squarer and the dispersion across the grating flattened [42]. Effectively, the individually phase shifted elements each give a different spectral and temporal response to the incident light. When this response is integrated over the full length of the grating, the individual responses interact to give a certain output. This form of operation is particularly useful for DWDM gratings in communications systems, where each FBG is required to have a minimal effect on the overall dispersion of the system. A non-phase shifted FBG would give a variable group delay across the band gap region; by optimising the design of a phase shifted FBG, this group delay may be reduced to a low level, as shown in

Figure 3-39. The design of such gratings is not an arbitrary task so requires a theoretical grating design approach such as the inverse scattering algorithm [43] or a layer peeling method [44].

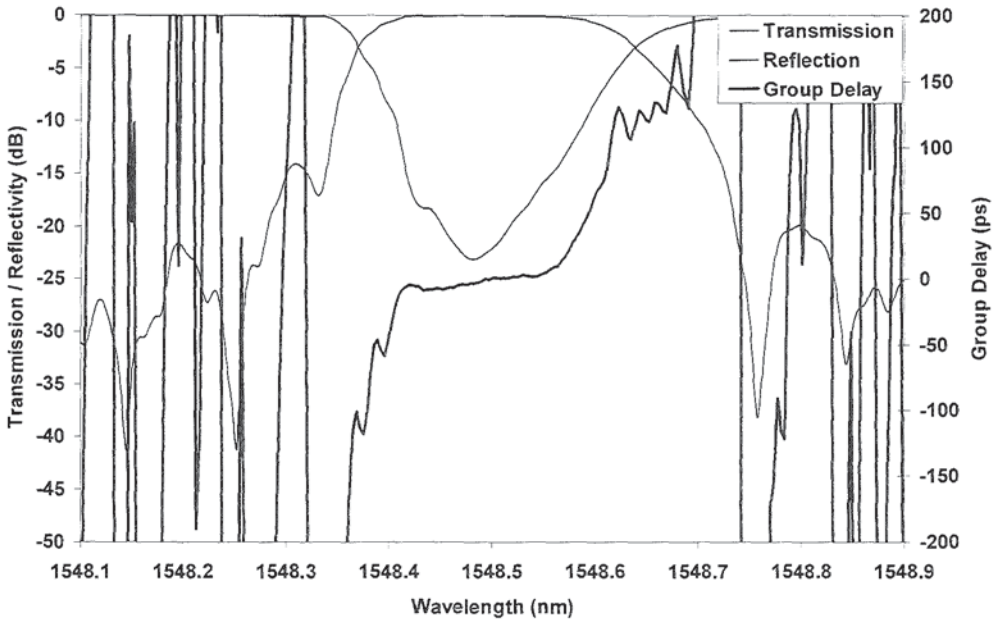

Figure 3-39: Transmission, reflection and group delay spectra of a phase shifted FBG designed by the company ADC and fabricated on the direct write system, to create a flat dispersion.

Similar gratings were fabricated for Elena Turitsyna from the Photonics Research Group at Aston University to demonstrate how asymmetrical vestigial side band filters with a flat group delay could be used to create a trade off between the cross talk and waveform distortions in an 8x40Gbit/s DWDM transmission system [45].

Due to the complexity of the phase shifted gratings, resolution is of an utmost importance. A slight positional error in the location of the phase shift will cause degradation in performance of the grating. One method of analysing the quality of the system, to create these complex structures, is to employ an optical frequency domain reflectometry (OFDR) method [46]. This allows the coupling coefficient along the grating to be measured. The FBGs in Figure 3-38 and Figure

3-39 were sent to Sven Kieckbusch at the Technische Universität Hamburg-Hamburg (TUHH) via Filip Floreani of the Photonics Research Group, the results are shown in Figure 3-40 and Figure 3-41.

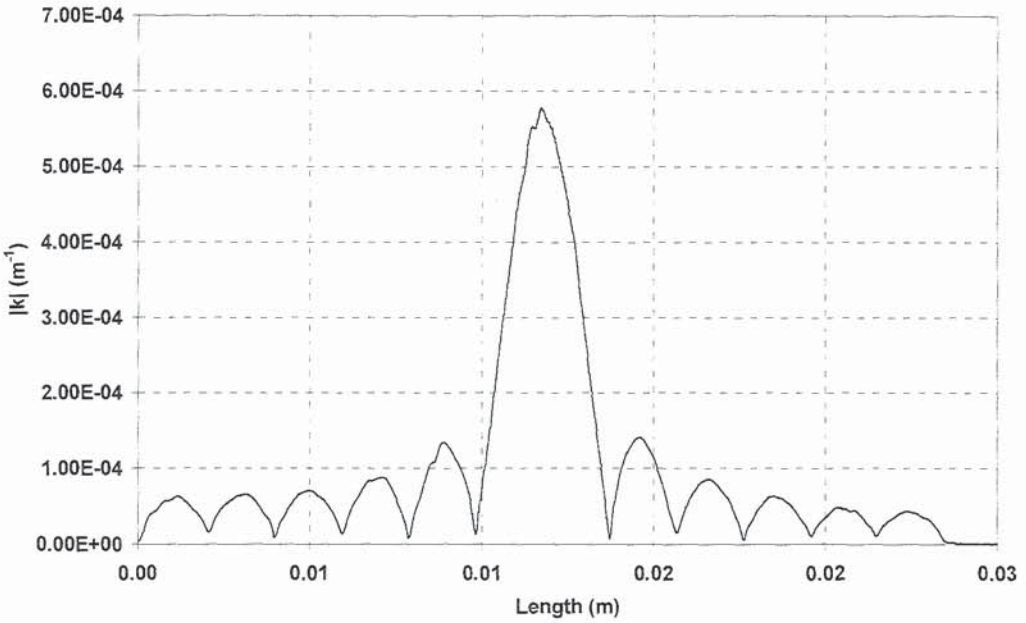

Figure 3-40: Measured coupling coefficient of a 23mm long Gaussian-sinc apodised FBG.

The sinc profile is clearly shown with 10 phase shifts along the length of the grating. An important feature to note is that the phase shift amplitudes do not drop to zero. This indicates that the visibility of the fringes is not perfect. Due to the averaging effect of the beam size, a perfect visibility would not be expected. Therefore for each phase shift there is a certain δn offset.

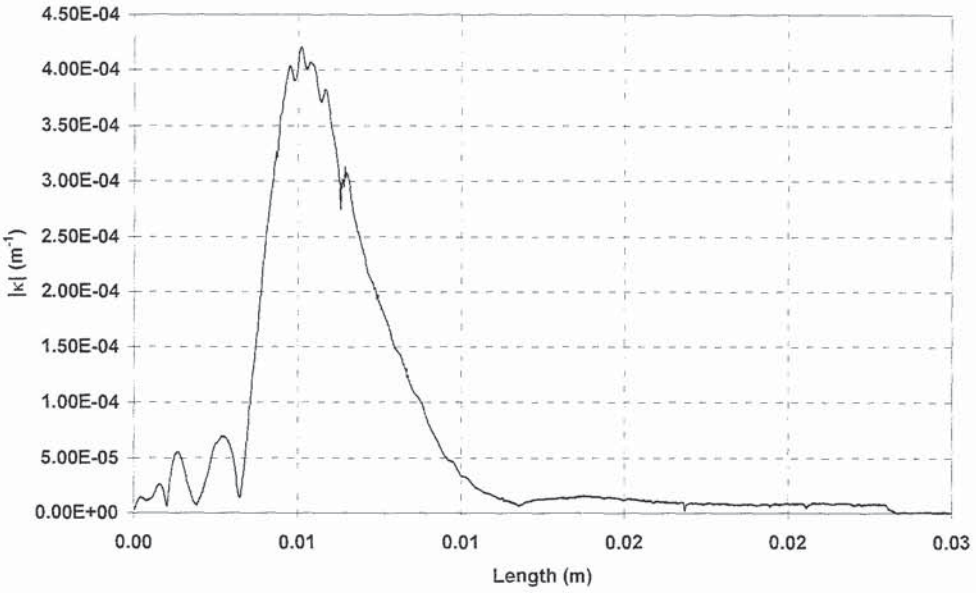

Figure 3-41: Coupling coefficient for the ADC grating.

Once again, Figure 3-41 shows a non-zero return of the phase shifts, another point to note is that the large amplitude section shows some small amplitude drops, which have a width of about 100μm. It is the author's belief that these drops are due to localised inhomogeneities in the fibre. The widths are indicative that the problems may have been caused by fibre pressing on those regions during storage or hydrogenation. In particular, if this was the case during the hydrogen loading process, a lower hydrogen absorption in the local area could be expected causing a reduction in the maximum coupling coefficient possible after exposure to UV light.

The fabrication system's ability to detune the operating wavelength allows arrays of gratings to be fabricated very easily. Figure 3-42 demonstrates nine 5mm long Gaussian apodised FBGs written with 6mm spacing between them. As previously mentioned with the chirp roll-off, the array also displays a roll-off due to dephasing. Such arrays can be useful for sensing applications, where a distributed system is required but the spectra shows a high level of cross-talk between the gratings due to the relatively wide bandwidth, limited ultimately by the short length of the gratings.

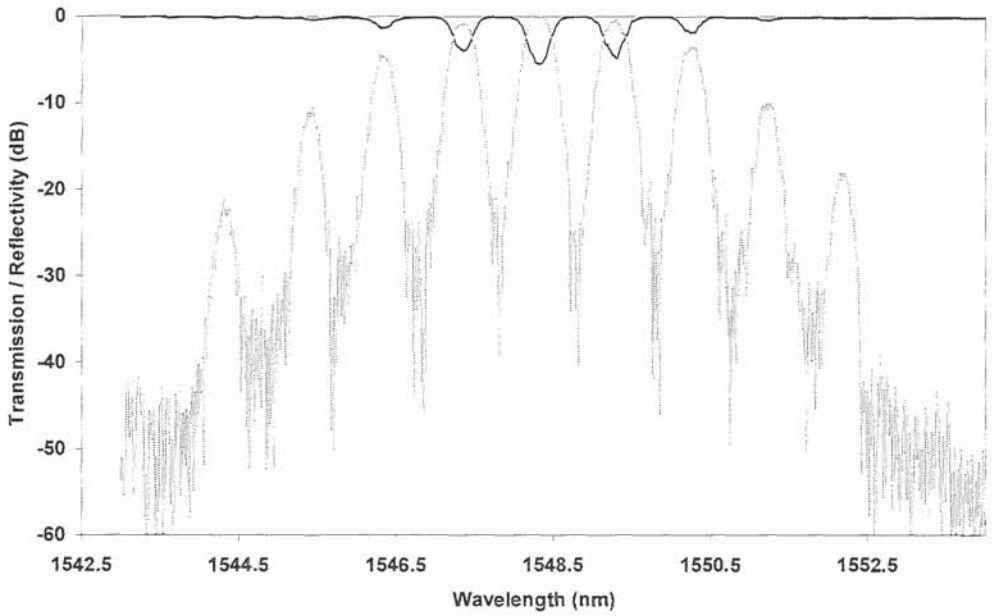

Figure 3-42: Array of nine 5mm long Gaussian apodised FBGs, equally spaced by 6mm apart.

The apodisation profiles are limited by the zero amplitude visibility, thus giving non-perfect zero visibility sections. The beam size also means that the sharpness of the edge of a profile will be blurred by the direct write method.

Superstructured Gratings

For filtering applications this cross talk is not acceptable, instead a better method is to use a superstructured FBG, as shown in Figure 3-43 where the individual gratings can be made much narrower. A superstructure grating is one where the overall spectral content is formed by a number of sub-gratings. These gratings typically display numerous wavelength peaks which are defined by the uniform period of each of the sub gratings, Λ_g, and the period of the overall envelope, Λ_e. The spacing between the reflected wavelengths is given by

$$\Lambda\lambda = 2n_{av}\frac{\Lambda_g^2}{\Lambda_e} \tag{3-7}$$

Where n_{av} is the average index of the mode. The profile for this grating was supplied by Dr Wei Zhang from the Photonics Research Group.

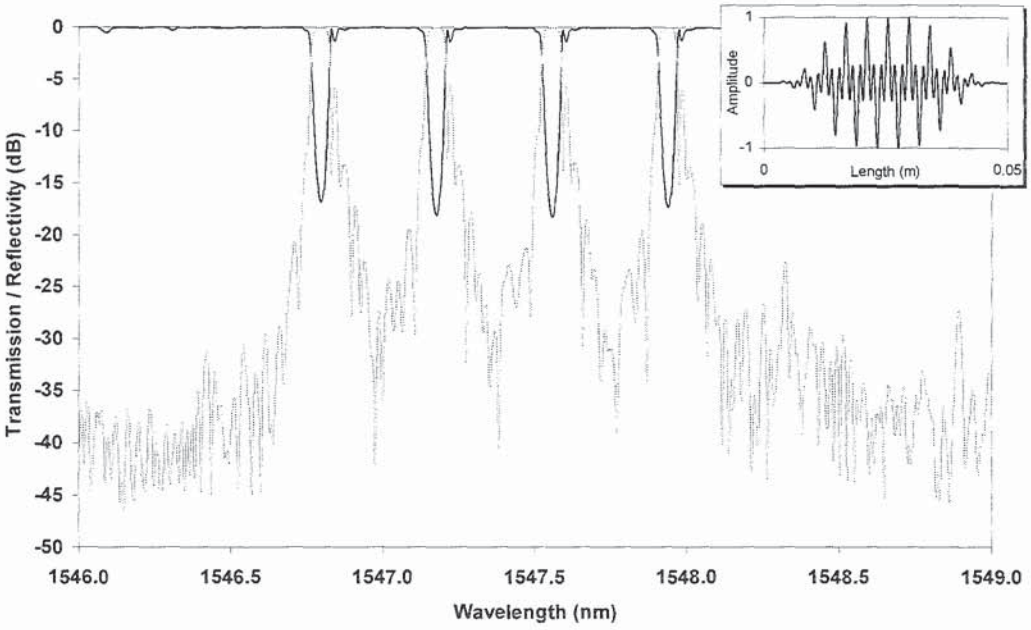

Figure 3-43: 50mm long superstructured FBG. The apodisation profile is shown in the top right-hand corner.

3.2.5 Future Work

A number of further improvements could be made to the direct write system:

- A telescope can be implemented within the beam line to give a smaller spot size, allowing a lower level of roll-off on chirped gratings.
- The roll-off can be compensated for by reducing the scan speed of the translation stage at the edges of a chirped grating.
- The beam path can be full enclosed in tubing to stop convection currents from changing the beam pointing.

These improvements would undoubtedly add to the quality of the system, however commercial time constraints limited the amount of work that could be conducted on the system.

3.3 Conclusion

The fundamental problems behind FBG fabrication are common to all types of fabrication systems. The presence of random amplitude and noise have been shown to have detrimental effects on grating quality but through iterative engineering, these effects can be eliminated to allow higher quality gratings to be produced. In a commercial environment it is imperative to provide a high quality product, not only to supply the customer with suitable FBGs but also to gain a competitive edge in a high cost, low revenue market. The burst of the telecoms "bubble" saw the closure of almost all FBG fabricating companies, leaving only those that could provide world beating gratings or companies that had diversified to expand their product portfolio away from telecoms.

4

WEAR SENSOR

Research work into FBGs took a drastic change of direction during the late 1990's, the commercial telecommunications market slumped and demand for high performance dispersion compensators and multiplexing FBGs vanished. Many research groups and a few companies realigned their direction towards using the intrinsic properties of FBGs as high-resolution sensors. This chapter presents the design and testing of a completely novel use for FBGs, as wear sensors. Such a wear sensor allows the amount of material removed from a surface to be directly measured. A typical application could include measuring change in thickness of a brake pad as it wears out over a period of time. Uniform, apodised and chirped FBGs are examined and compared with reference to each other and their commercial viability.

4.1 Background

Wear sensors that measure the removal of material from a surface exist utilising a variety of technological methods. They find applications on unmanned

machining systems, such as milling machines, and present the opportunity of expansion to further fields including vehicle braking systems and the drilling industry. These current technologies include thin-film techniques [47-48], machine vision systems [49] and discrete level sensors [50]. The different methods of monitoring wear have particular problems associated with them. The thin-film and discrete level sensors both require electrical current to pass through the sensing device, this can cause operational problems such as short circuits or open circuits to occur as a consequence of the wear, thus giving spurious results. The machine vision method requires a camera to have direct visual access to the area being worn, so is not applicable to compact or dirty applications. The aim of creating an optical wear sensor was to overcome some of the current shortfalls that inhibit the performance of the methods already available.

A chirped fibre Bragg grating (CFBG) [51] is made up of a sinusoidal variation of the refractive index within the core of an optic fibre. The period of this sinusoid, $\Lambda(z)$, changes continuously with position along the length of the grating, z, depending on the chirp rate of refractive index sinusoid which forms the grating, C. The period of the sinusoid at any point along the fibre is given by

$$\Lambda(z) = \Lambda_0 + Cz \tag{4-1}$$

where Λ_0 is the period of the grating at position zero. The refractive index of any point within the core, $n(z)$ is given by

$$n(z) = n_0 + \Delta n \cos\left(\frac{2\pi z}{\Lambda(z)}\right) \tag{4-2}$$

where n_0 is the refractive index of the fibre core and Δn is the change in refractive index due to illumination by an ultraviolet laser light. Using the Bragg wavelength equation

$$\lambda_B(z) = 2n_{eff}\Lambda(z) \tag{4-3}$$

where, n_{eff} is the effective refractive index of the grating, the approximate bandwidth of a chirped grating may be given by [8]

$$\Delta\lambda \approx 2n_{eff}\ \ \Lambda(z_{\max}) - \Lambda(z_{\min}) \tag{4-4}$$

where $z_{\max}$ and $z_{\min}$ are the maximum and minimum positions of the grating, respectively. This approximation has been chosen as other methods [1] measure the bandwidth from the zeros on either side of the main reflected signal. Such minima are not accurately measurable for a non-apodised CFBG in an experimental environment due to expected high level of back reflections. The difference between the bandwidth results from (4-4) and [1] is insignificant to the total bandwidth of the CFBG thus it is fair to use this approximation. Equation (4-4) may be rewritten as:

$$\Delta\lambda = \Delta\lambda_0 - \Delta\lambda_t \tag{4-5}$$

Where $\Delta\lambda_0$ is the initial bandwidth of the grating and $\Delta\lambda_t$ is the bandwidth at any later time. As, by definition, the chirp rate is the spectral bandwidth per unit length and considering the fact that the grating is written into a medium of a non-unitary refractive index, equation (4-5) therefore becomes

$$\Delta\lambda = n_{eff}CL \tag{4-6}$$

Where L is the length of the grating. In the situation where a grating is wearing down due to abrasion, equations (4-5) and (4-6) may be rearranged to give

$$W = \frac{\lambda_0 - \lambda_t}{n_{eff}C} = \frac{\Delta\lambda}{n_{eff}C} \tag{4-7}$$

L has been replaced by the letter W to give a measure of the amount of wear taken place on the grating. This therefore sets up a method of very accurately measuring the wear on a CFBG in relation to its decaying bandwidth.

4.2 Chirped FBG Wear Sensor

Non-apodised CFBGs of 97% reflectivity and a length of 20mm were written in hydrogenated SMF-28 using a 244nm frequency doubled CW FreD laser and a scanning beam phase mask fabrication technique. In order to prevent hydrogen out-diffusion from affecting the results the CFBGs were annealed at 90°C for 48 hours before any measurements were taken. A non-apodised design was chosen as when the grating starts to wear down the apodisation profile would effectively be destroyed.

To simulate a real-life situation, the CFBGs were super-glued onto a carbon fibre rod and the end of the rod worn away via abrasion with a file. As the rod wore away, the subsequent length of the CFBG reduced. Two separate experiments were conducted to measure this wear. In one experiment, the wear of the CFBG was measured by fusion splicing the grating to a 50/50 coupler that was connected to an Agilent 8164A Lightwave measurement system, which was used to record the reflection spectrum of the grating as it was worn away. In order to gain a high resolution measurement of the physical amount of the grating that remained, an Ando AQ7410 High Resolution Reflectometer was used. The measurement method is shown in Figure 4-1(a). An initial reflection spectrum was recorded then a length measurement taken using the reflectometer, this was followed by a small amount of wear to the rod. The process was repeated until no grating was left. Two different chirped phase masks were used to give two different chirp rate gratings. The chirp rates which these phase masks wrote were quoted as 1.6nm/mm and 2.8nm/mm.

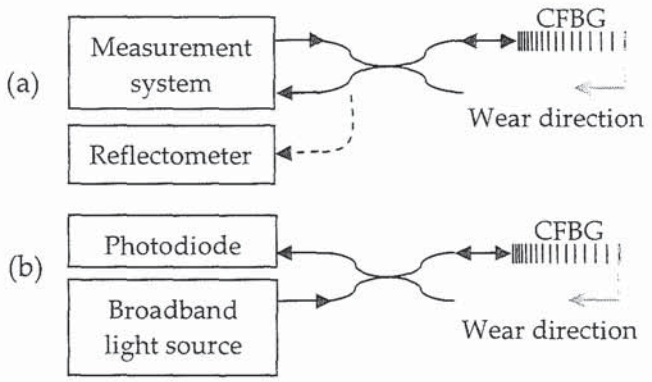

Figure 4-1(a) Arrangement for measuring the reflection spectrum and length of the CFBG using a reflectometer. (b) Set-up utilising a broadband light source and a photodiode.

A similar process was repeated for the second experiment. Instead of taking a reflection spectrum the voltage response of a photodiode was used to indicate the total power of light reflected by the CFBG, shown in Figure 4-1(b), and the length of the grating remaining was measured using a ruler. Due to time constraints the experiment was conducted with only the gratings of a 2.8nm/mm chirp rate.

4.2.1 Wear Detection Using Spectral Measurement System and Reflectometer

As the wear sensors underwent abrasion the physical length of the CFBG reduced. This caused a reduction in the bandwidth of the reflected spectrum due to the longer period fringes within the CFBG being destroyed, as shown in Figure 4-2.

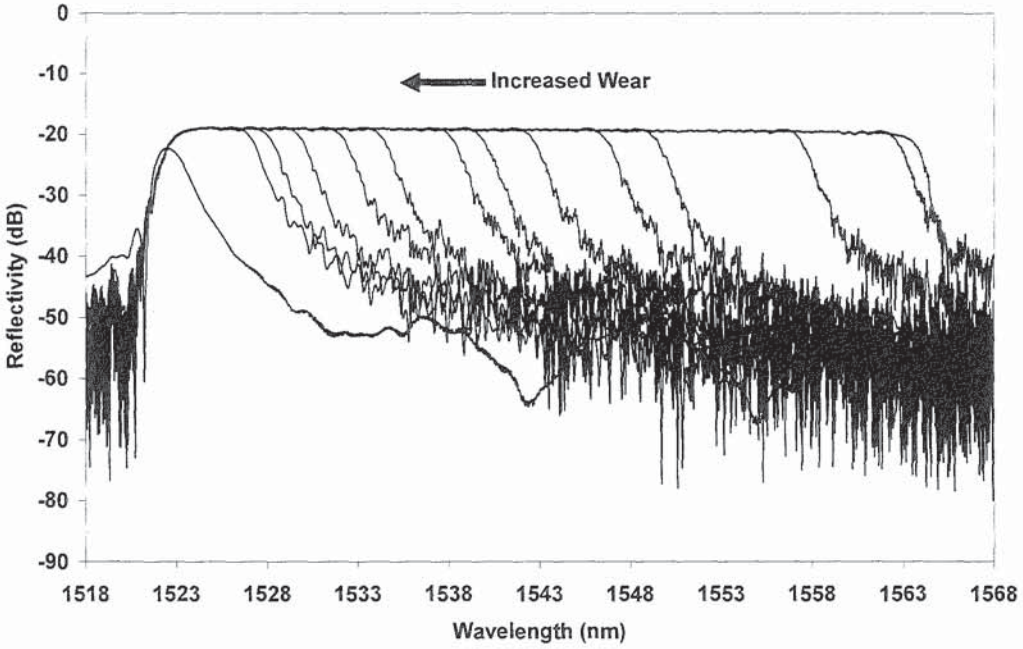

Figure 4-2: CFBG reflection spectrum reducing as the sensor wore down, measured on the Agilent measurement system. This grating was 20mm long, written with the 1.6nm/mm chirp rate phase mask.

A similar set of results were obtained by swapping over the patch-chords to gain a measurement of the length of the grating remaining using the reflectometer, as shown in Figure 4-3.

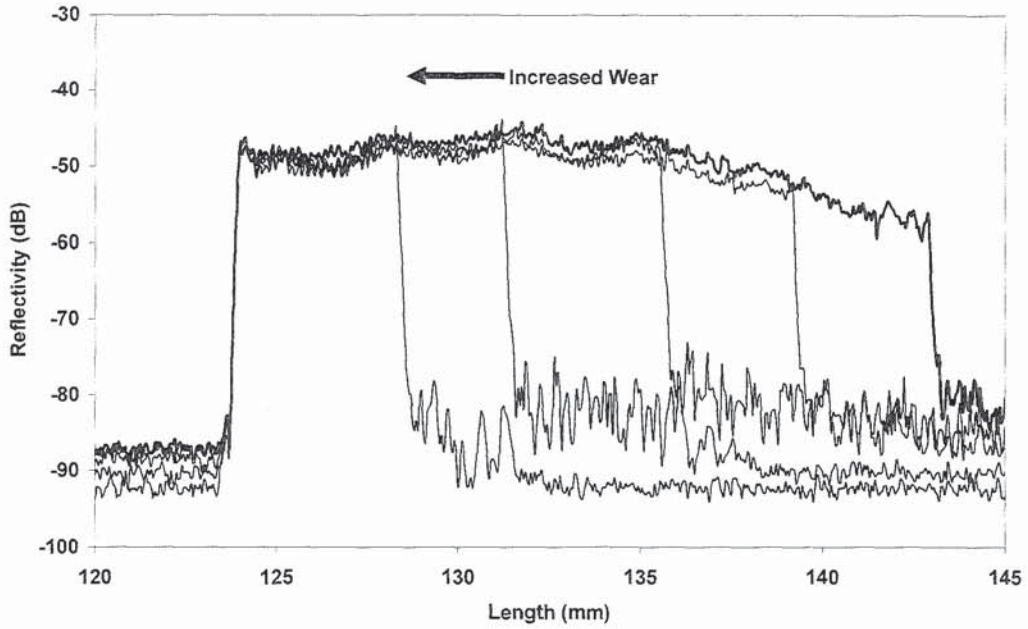

Figure 4-3: Reflectometer measurements for different wear states.

The roll off of the reflection amplitude at higher fibre lengths in Figure 4-3 was due to the spectral response of the light source within the reflectometer not being uniform across the spectral bandwidth of the CFBG. It is clear from Figure 4-2 that the reflection level of the CFBG was extremely constant across the full bandwidth when measured with the high quality tuneable light source within the Agilent measurement system.

The theoretical resolution of the wear sensor is dependant on the resolution of the 3dB bandwidth measurement device, the chirp rate and the refractive index. This is given by

$$Resolution = \frac{d\Delta\lambda}{n_{eff}C} \tag{4-8}$$

Where $d\Delta\lambda$ is the resolution of the measurement system. For a chirp rate of 2.8nm/mm and a 3dB bandwidth measurement resolution of 5pm, a theoretical wear measurement could be made to a resolution of ~2μm. In practice, it is unlikely that this resolution would be achieved due to random and systematic

errors associated with the measurement devices. To gain an accurate measurement of the length of the grating a scanning microscope could be used thus giving a highly accurate length measurement to compare the calculated lengths against.

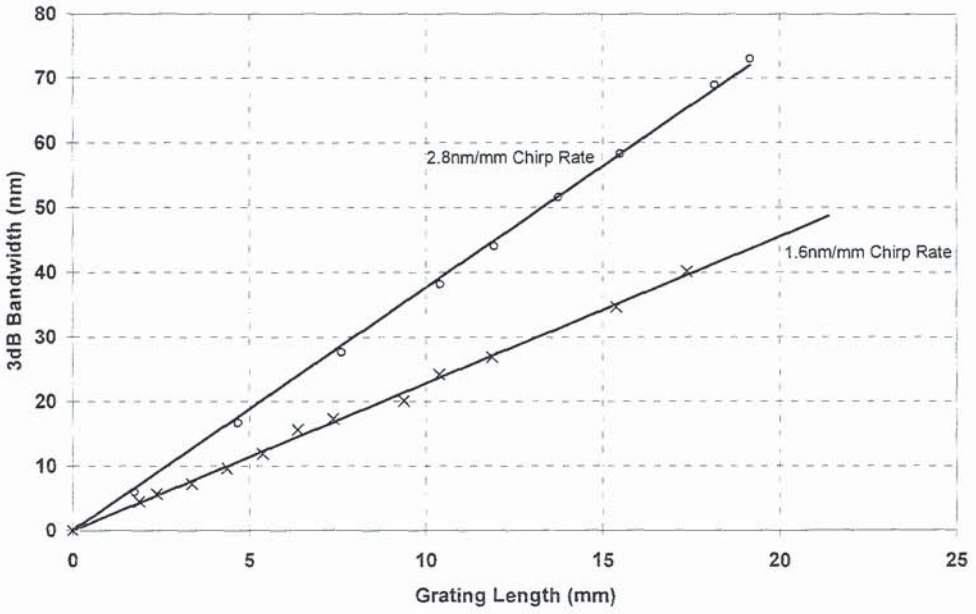

Figure 4-4: Linear decay of spectral bandwidth with reducing grating length, showing the response from two differently chirped gratings: 2.8nm/mm and 1.6nm/mm with the grating length measured using a reflectometer.

As the CFBGs were fabricated using a linearly chirped phase mask, the bandwidth responded linearly to the grating length. Using a phase mask with a higher chirp rate gives a steeper gradient of response as shown in Figure 4-4. The gradient of the wear response is given by substituting (4-1) into (4-4) and differentiating with respect to z. For the case where z_{min} is equal to zero this gradient is given by:

$$\frac{d\Delta\lambda}{dz} = n_{eff}C \tag{4-9}$$

The standard deviations, σ, of the results for the CFBGs using the reflectometer were measured. The standard deviation for the 1.6nm/mm CFBG was 270μm and the standard deviation for the 2.8nm/mm CFBG was 120μm.

4.2.2 Wear Detection Using a Broadband Light Source and a Photodiode

The experiment using a broadband light source and a photodiode showed similar results to the reflectometer measurements, as shown in Figure 4-5. These results yielded σ as 200μm. This standard deviation is significant since it is less than the error incurred in reading the length of the grating with a ruler which is estimated at ±250μm. This would imply a strong correlation towards the mean value along the slope. A higher resolution method would have been to measure the length using a travelling microscope.

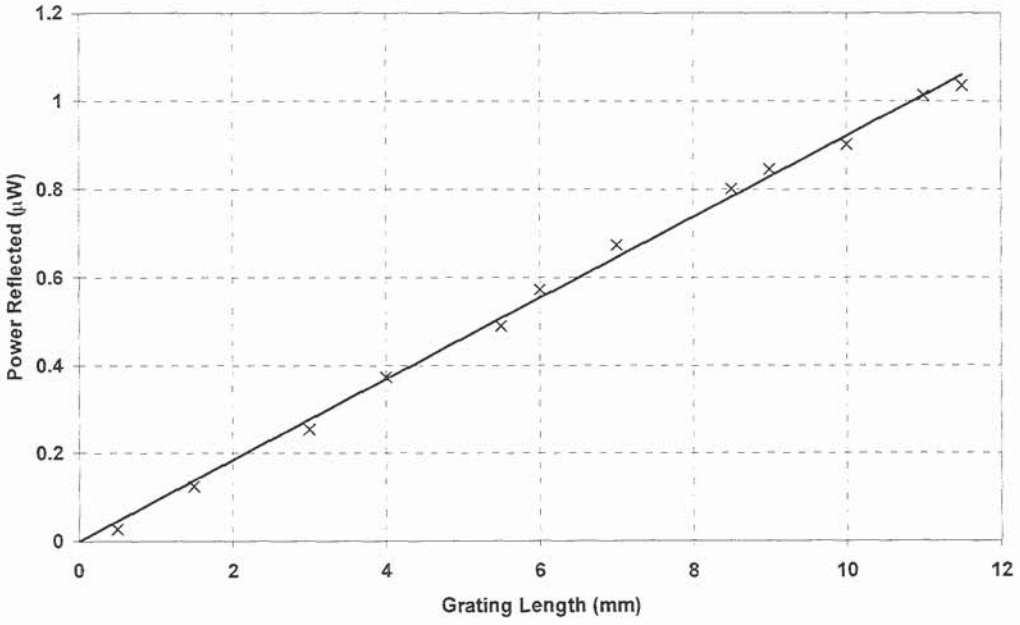

Figure 4-5: Response of a 2.8nm/mm CFBG sensor using a broadband light source and photodiode, grating length measured with a ruler.

4.2.3 Input Power Insensitive Measurements

The measurements using the photodiode have a dependency on the stability of the light source. A variation in the output power of the light source will cause a non-constant wear measurement. It is therefore appropriate to create a system

which would not give a variable wear measurement with fluctuating light source emission. To combat this, a system incorporating an identical chirped FBG and an extra power meter was created, as show in Figure 4-6.

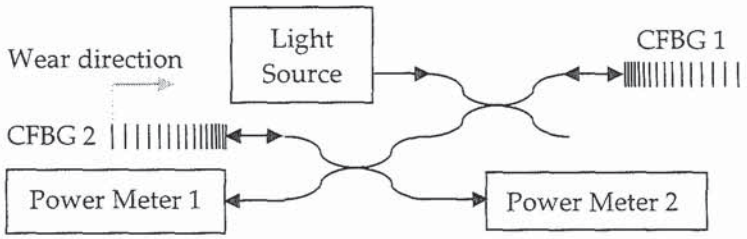

Figure 4-6: Power invariable arrangement.

The reflected signal from CFBG 1 passes back through the original 50/50 coupler and half of the signal is transferred to a second 50/50 coupler. At the newly introduced coupler, the signal is split between the CFBG 2 wich acts as the wear sensor and power meter 1. The reflected signal from the CFBG wear sensor passes back through the coupler and half the signal is passed to power meter 2. With such a set up the ratio of the signals from power meter 2 to power meter 1 will give you a constant value even if the power output from the light source fluctuates. This is shown in Figure 4-7.

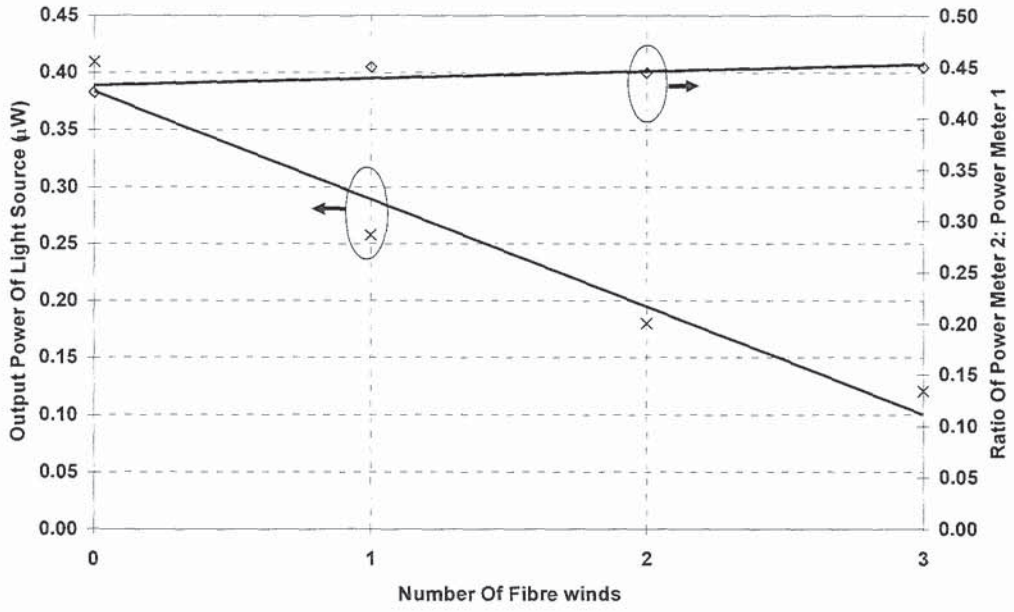

Figure 4-7: Invariable response of the wear sensor to a reduction in the output power of the light source. Showing the decaying power of the light source with the crosses and the relatively constant value of the ratio of power meter 2 : power meter 1 with diamonds.

The results for Figure 4-7 were obtained by wrapping the output patch chord from the light source around a 1.5cm diameter mandrel, thus creating loss in the fibre by causing out-coupling of light from the core into the cladding. This effectively acted as a method of reducing the optical output of the light source. Each time the patch chord was wrapped around the mandrel the power readings from power meter 2 and 1 were taken and the ratio of the two calculated. It is clear to see that as the reflected light from the first CFBG reduced, measured on power meter 1, the ratio of the power readings from power meter 1 and 2 remained roughly constant. In order to check that the system still worked as a wear sensor in this configuration, another CFBG 2 was worn and the ratios of power from the two power meters measured, as shown in Figure 4-8.

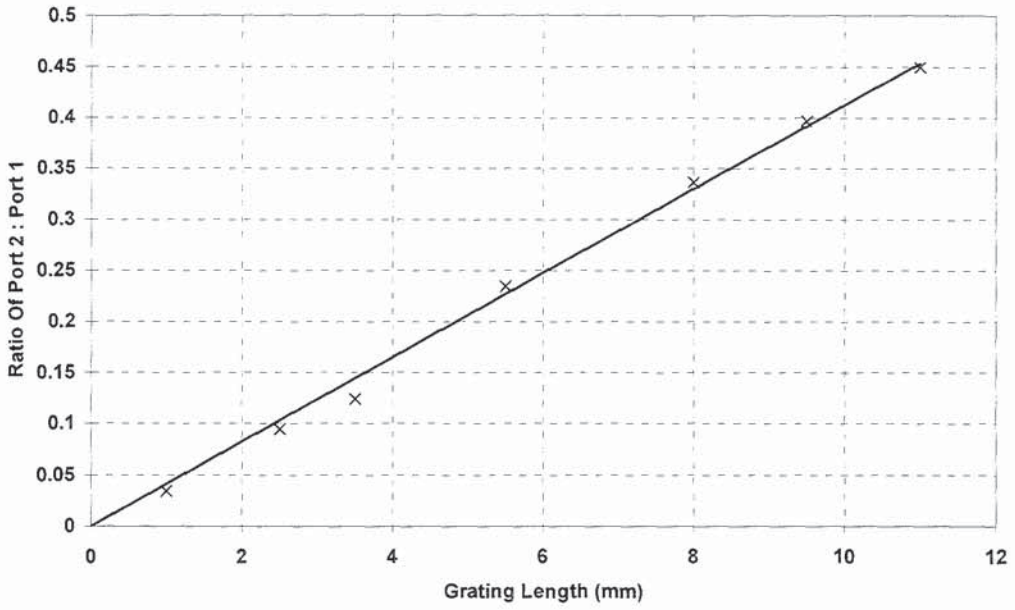

Figure 4-8: Decay of the ratio of power measured at port 2 : port 1 as the grating length reduces.

The power insensitive method may be regarded as overly complex when a simpler self-normalisation method could be implemented. Such a system would consist of the setup shown in Figure 4-1 but with a power meter at the open arm of the coupler. In such a situation the throughput power can be monitored and the reflection response of the CFBG adjusted accordingly. This method was not implemented as the bandwidth of the light source is spectrally broader than the CFBG. Thus any wavelength dependant losses occurring beyond the bandwidth of the CFBG would be misinterpreted as a loss of power within the reflected signal from the CFBG. Therefore the method would incorrectly self-normalise.

4.2.2 Back Reflections

As the wear sensor operates in the reflection regime the back reflections from the end of the fibre need to be considered. The actual application of the sensor will vary the level of the back reflections. If the sensor is embedded into a system where the tip is worn away by a smooth surface (such as in a vehicle braking system) and at a perpendicular angle to the fibre axis then a flat fibre end will

effectively be polished, giving high back reflections. In the situation where the end of the fibre is broken more abruptly the fibre will fracture so causing a non flat end which ultimately lowers the back reflections. Figure 4-9 shows microscope images of two such situations.

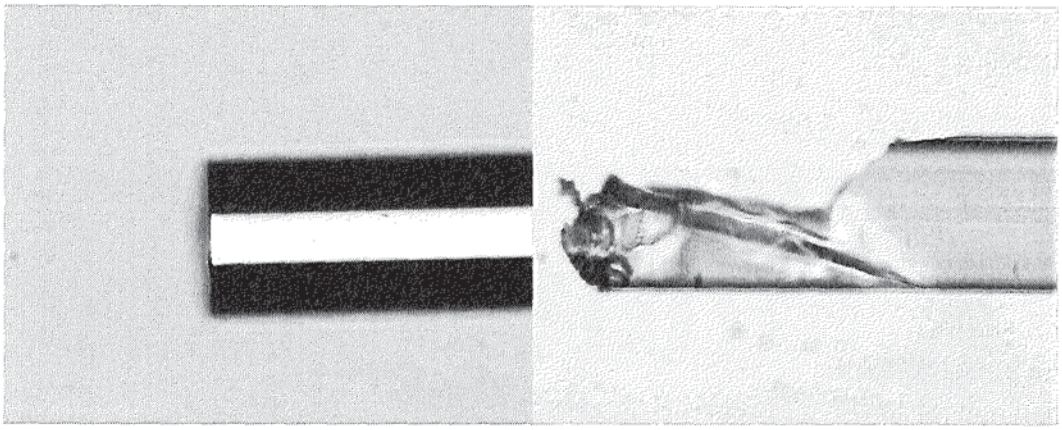

Figure 4-9: Microscope images of a perfectly cleaved (left) and fractured with wire cutters (right) fibre ends at 20x magnification.

For these two situations the reflected spectra were measured, shown in Figure 4-10. The highest wavelength trace is the original CFBG followed by three lower wavelength traces which were taken when the grating was reduced in length by cutting the fibre with wire cutters, simulating a rough fracture. Here you can see that the background noise is reduced below the -40dB level. The final and lowest wavelength trace was taken after the end of the fibre was cleaved with a fibre cleaver. It is clear to see that the background noise level increases to -33dB due to the flat end giving a ~3% back reflection. In both situations the noise level is low enough to still measure the 3dB bandwidth. In the power measurement method the higher level of back reflection would create a slight pedestal in the power reflected measurements, thus making it less accurate.

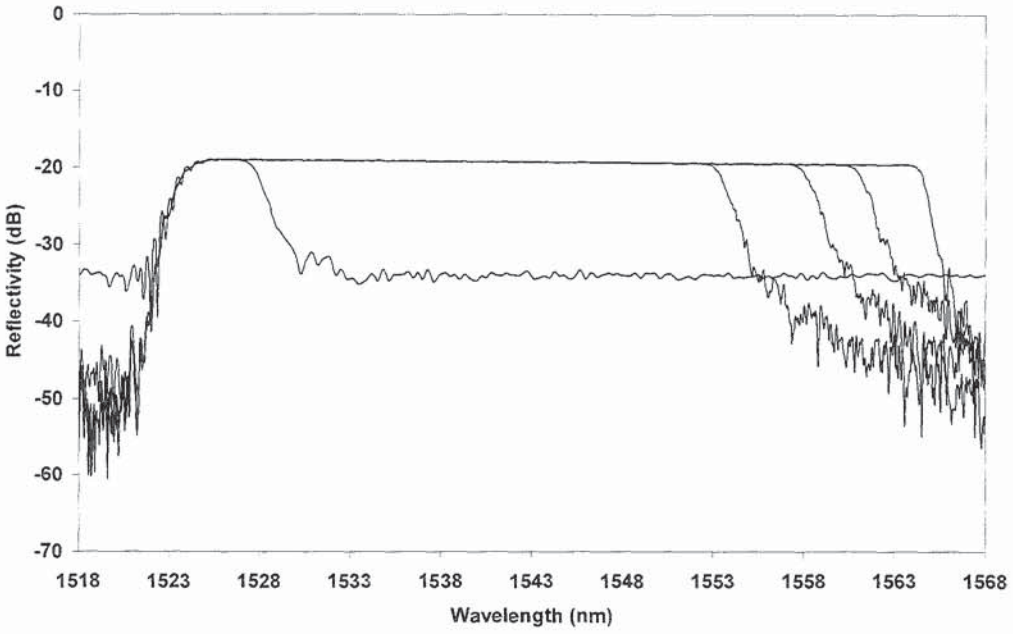

Figure 4-10: Showing the wear of a chirped FBG with the final wear being inflicted by a cleaver. The black trace is the original CFBG spectra with the grey traces representing different wear states. The smallest bandwidth trace was shortened with a cleaver rather than with abrasion.

In applications where the sensor would be worn away smoothly, the CFBG could be embedded at ~5° to the perpendicular. This would cause any back reflection, from the end face, to be coupled into the cladding rather than the core. The wear calculation would therefore require a minor trigonometric adjustment.

4.2 Uniform Period FBG Wear Sensor

Having investigated the use of CFBGs as wear sensors, non-chirped FBGs were then used as the sensing element. The motivation behind initiating this work was that the CFBGs were difficult and time consuming to make with would therefore be costly to manufacture at high quality. Uniform and apodised FBGs are far easier and cheaper to manufacture than CFBGs. So if accurate wear sensors could be created using FBGs then the potential fabrication cost of such a sensor could be drastically reduced.

A variety of different FBGs were made, both uniform and apodised. The uniform FBG was written with an 18dB transmission strength and the apodised gratings had transmission strengths of 12, 24 and 32dB. All of the gratings were written with a scanning phase mask technique at Indigo Photonics.

The theoretical and experimental results for the uniform FBG wear sensor are shown in Figure 4-11 and Figure 4-12. The theoretical spectra show the grating as it decays by 2mm per trace. The relationship between the length of the FBG and the bandwidth is described by the equation [7]:

$$\Delta\lambda = \frac{\lambda^2}{\pi n_{eff} L}\sqrt{(\kappa_{ac}L)^2 + \pi^2} \tag{4-10}$$

Where $\Delta\lambda$ is the bandwidth, κ_{ac} is the coupling coefficient and L the length of the grating. The equation implies that for a weak grating the bandwidth is proportional to the inverse of the length. This inverse proportionality is obvious from Figure 4-11 during the final four traces, where the bandwidth can be seen to grow rapidly.

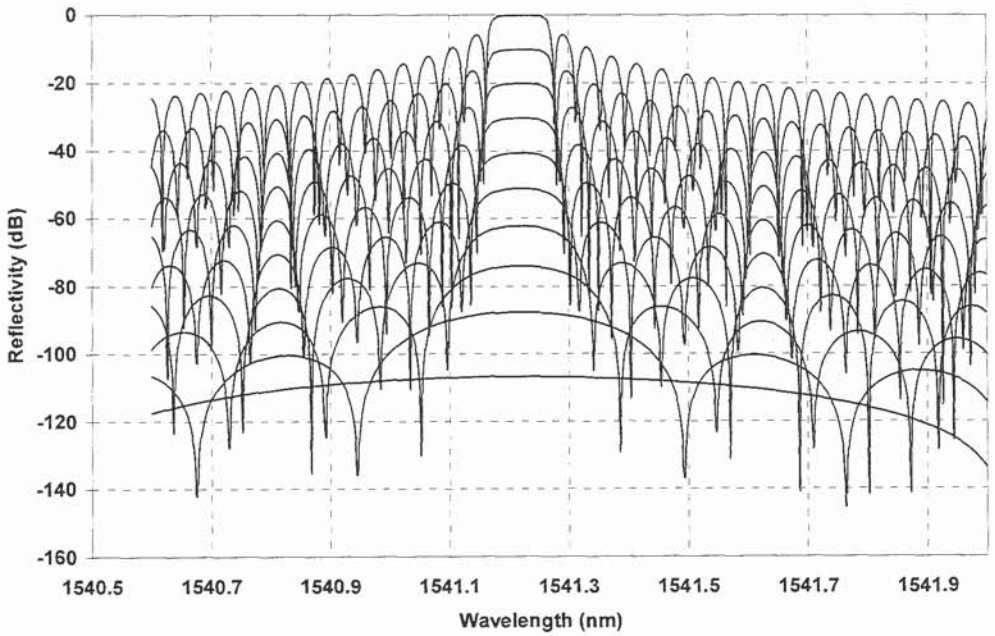

Figure 4-11: Theoretical reflection spectra of an 18dB, 20mm long uniform FBG as the length of the grating is reduced (longest grating at the top). Each subsequent spectrum is offset by -10dB.

The experimental spectra shown in Figure 4-12 shows the grating being shortened by non-uniform lengths. This is due to the wear being difficult to control. Spectrally, the theoretical and experimental traces are very similar apart from a slight asymmetry in the sidelobes and some irregularity at ±6nm. These deviations are due to inaccuracies encoded during the fabrication process of the FBG.

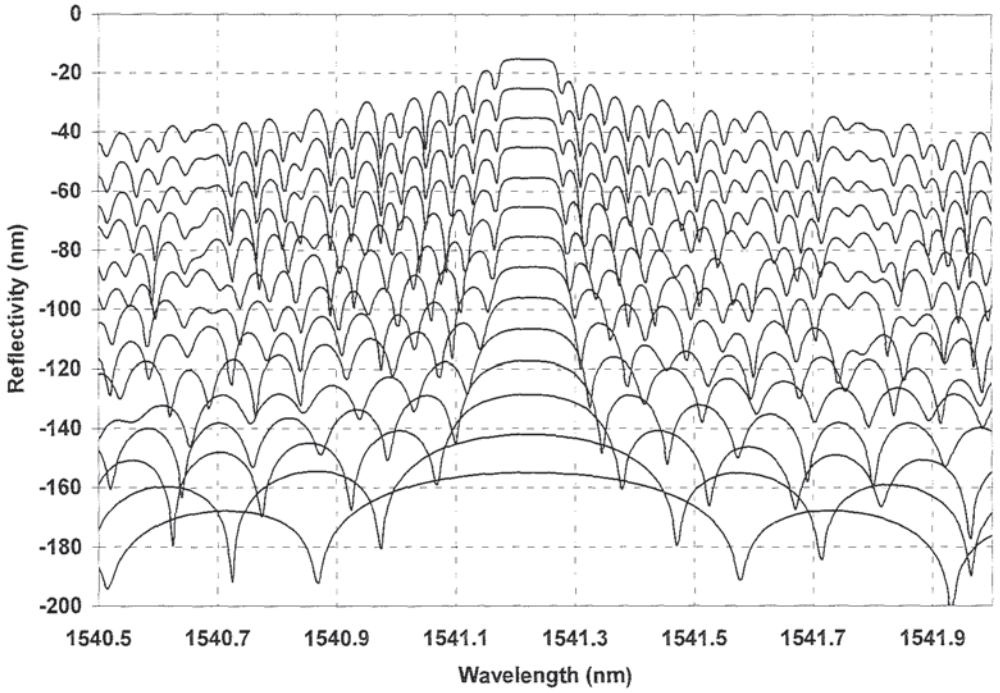

Figure 4-12: Reflection profile of 18dB uniform non-apodised FBG undergoing wear (longer grating towards the top). Each subsequent spectra is offset by -10dB. Each subsequent spectrum is offset by -10dB.

As a comparison, apodised FBGs were also investigated. The high sidelobes of the FBGs made it difficult to write a program to automatically detect the -3dB bandwidth of the grating. So apodised gratings, with good sidelobe suppression, were tested for their application in a wear sensing system. By applying a Gaussian apodisation the sidelobes were suppressed to about 20dB below the

main peak, allowing easy automatic detection of the 3dB bandwidth. The bandwidth was measured by finding the nearest data points above and below the 3dB line, on either side of the Bragg wavelength, and extrapolating the data to the 3dB point. This technique works well as long as the grating is apodised so that the Bragg peak is not confused with a sidelobe. The theoretical and experimental responses of the apodised wear sensor are shown in Figure 4-13 and Figure 4-14. The theoretical and experimental results have a worse fit than for the uniform grating. Once again, this is due to inaccuracies in the grating inscription since high resolution control of the apodisation profile is difficult to obtain experimentally. The behaviour of the bandwidth is more complex than in the uniform FBG. There is a growth in the bandwidth, followed by decay and then a further growth in the bandwidth as shown in Figure 4-15.

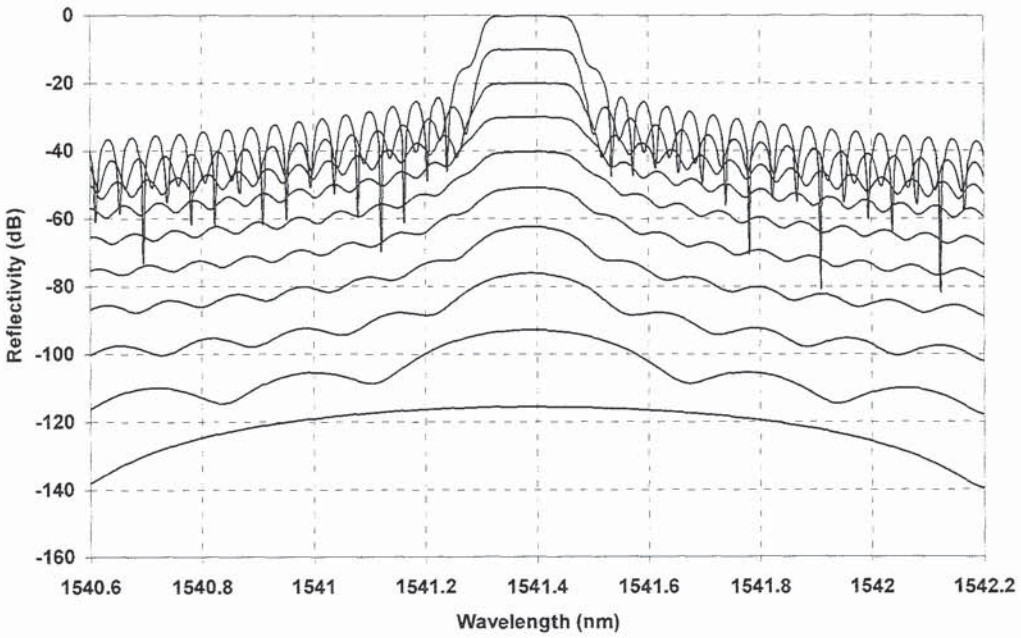

Figure 4-13: Theoretical spectral response of a 24dB Gaussian apodised FBG as a wear sensor. Each subsequent spectra is offset by -10dB.

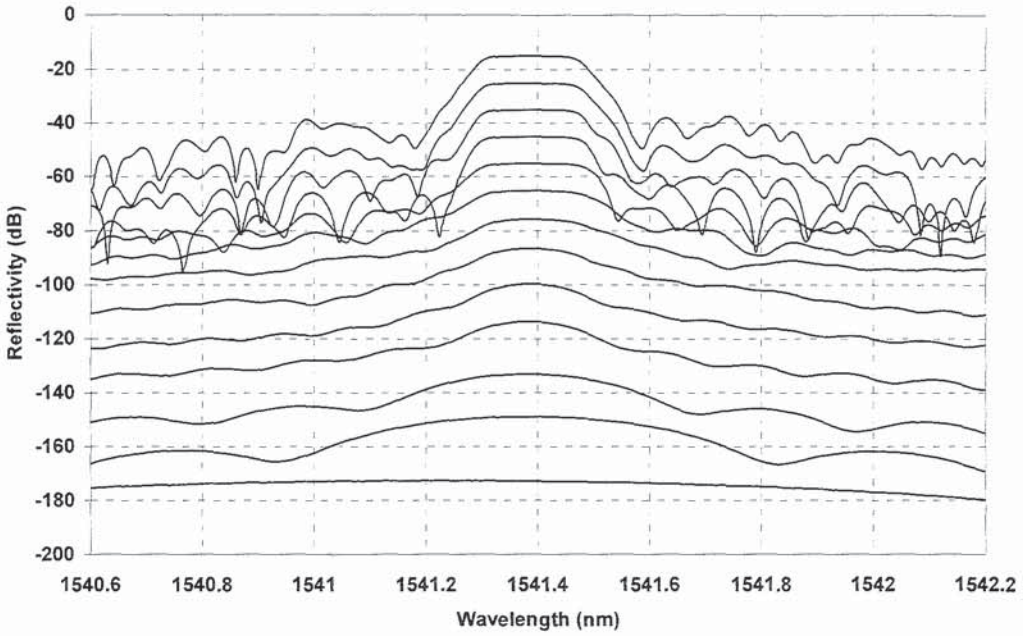

Figure 4-14: Experimental reflection profile of 24dB apodised FBG undergoing wear. Each subsequent spectra is offset by -10dB.

All of the 3dB bandwidth data is summarised in Figure 4-15. The 3dB bandwidth was measured by a LabVIEW program written by the author, taking the data points straddling the 3dB level, either side of the Bragg wavelength, and extrapolating the x- and y-coordinates to give a bandwidth value at 3dB. This technique was not the most accurate possible as the noise on the short wavelength edge can create spurious results. A shape fitting technique would be more suitable. Figure 4-15 shows the comparison of data for the experimental 18dB uniform FBG and the 12, 24 and 32dB apodised gratings along with the modelled 3dB bandwidths for each of these cases.

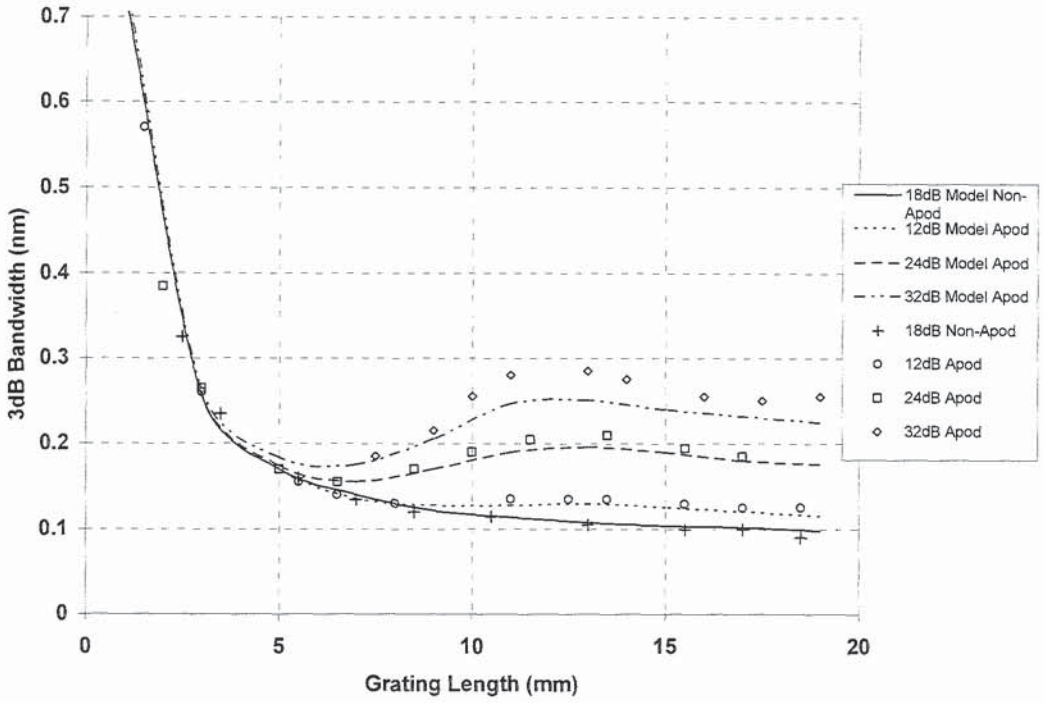

Figure 4-15: Summary of modelled and experimental data using the -3dB bandwidth of wearing apodised and non-apodised FBGs.

The results show that it would be possible to use a uniform non-apodised FBG as a wear sensor, however the non-linear bandwidth response of the grating would make it difficult to calibrate. The apodised gratings could not be used as accurate wear sensors, the bandwidth increases and decreases with reducing grating length. The possibility arises where the same bandwidth can occur for two different lengths of the same grating, this would therefore give rise to incorrect wear measurements. The modelling results in Figure 4-15 were obtained from the commercially available IFO Gratings package by calculating the bandwidth of the FBGs using the profiles shown in Figure 4-16. The Gaussian apodisation profile was shortened by returning the profile to zero at the point where the physical wear of the grating had occurred. The 3dB bandwidth results for the uniform FBGs show the expected growth shape as given by equation (4-10). However, for the apodised FBGs the longer grating length results deviate away from this inverse relationship. The effect also becomes more prominent as the apodised gratings become stronger. It is clear from Figure 4-15 that there are at least two

effects and possibly three occurring simultaneously. For the case where the grating length, L < 5cm the inverse relationship is the dominant factor and around 12cm the drop in bandwidth with reducing length indicates a change from one factor to another.

The bandwidth behaviour of the gratingcan be understood my considering the physical changes that occur to the grating as it is worn down. Firstly, the grating is becoming shorter therefore some form of the inverse relationship must exist. Secondly, as the grating is apodised, the strength of the grating comes mainly from the centre section and not from the edges. Therefore you would expect a greater change in the bandwidth where the central section of the grating is worn away rather than wear occurring at the edges of the grating. Thirdly, the apodisation shape has an effect on the bandwidth. As the grating wears away the grating becomes more asymmetric, an effect that needs to be considered.

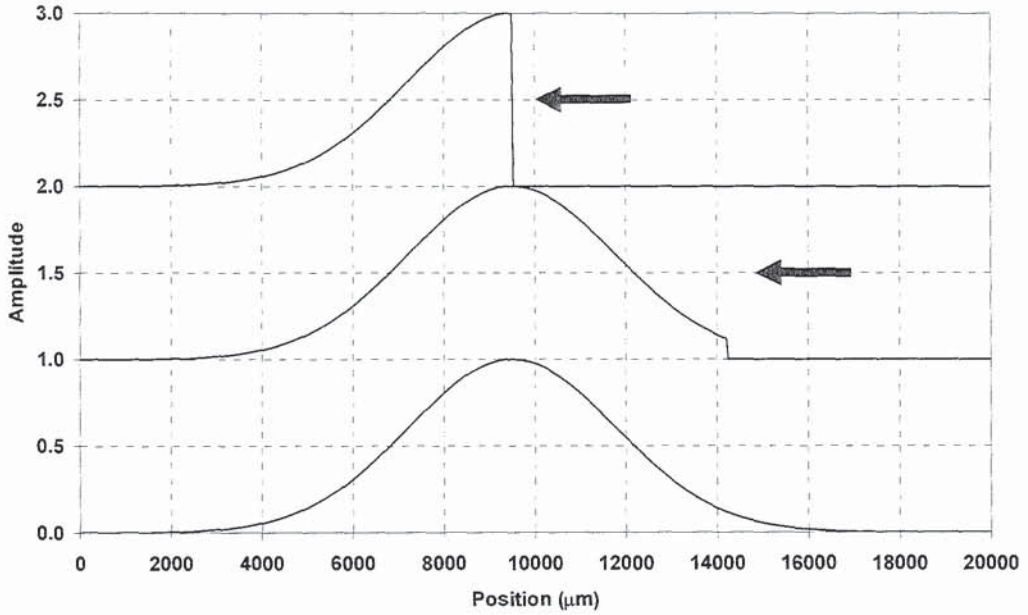

Figure 4-16: Apodisation shape used to model the wearing FBGs.

The three individual effects may be modelled individually to show how they would each affect a grating. Firstly, the effect due to the reducing grating length was simply modelled by using a uniform grating profile and reducing the length,

giving the inverse relationship between the length and the bandwidth. Secondly, to account for the aspect that each segment of the FBG provides a different weight to the overall strength of the grating, the decay in strength of the experimental gratings were noted, then 20mm Gaussian apodised gratings were modelled with strengths equal to those of the decaying experimental gratings. Thirdly, in order to give some indication as to how asymmetry affects the bandwidth the Gaussian apodisation shape was made less symmetric by increasing the high length end of the grating but the strength of the gratings were maintained at the same level. The apodisation profiles used for these three effects are shown in Figure 4-17.

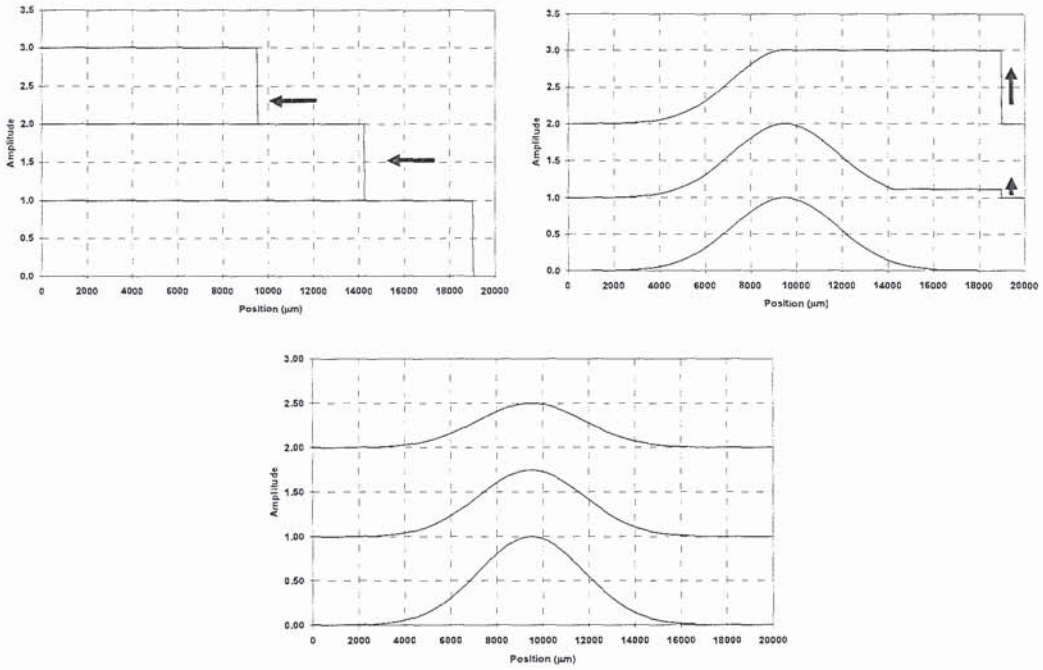

Figure 4-17: Three grating profiles to explain the bandwidth behaviour as an apodised FBG reduces in length. Reducing length (top left), increasing asymmetry (top right) and reducing strength (bottom).

By plotting the three different models separately in Figure 4-18 it becomes clear how each become dominant at different grating lengths. At long grating lengths the increase in bandwidth due to the asymmetry of the grating causes the rise in bandwidth since both the length and strength bandwidths are relatively flat.

Towards the middle of the grating the drop formed by the strength model becomes dominant as the asymmetry bandwidth levels off and the length model still remains flat. At short wavelengths the length becomes dominant partly due to the asymmetry and the strength effects flattening off and mostly due to the huge growth in the bandwidth of the length model.

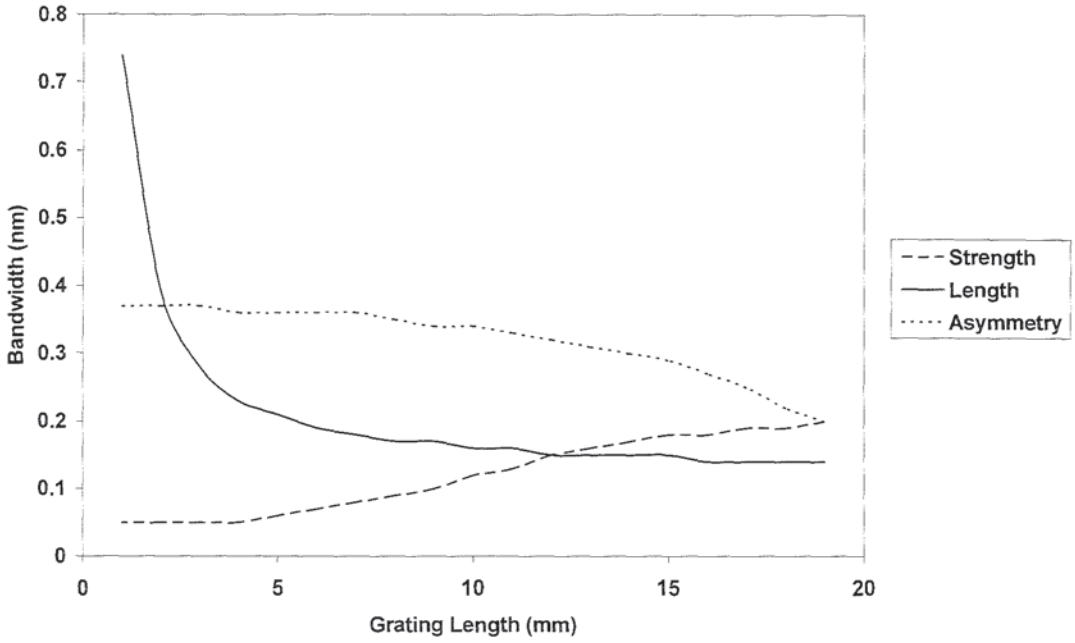

Figure 4-18: Bandwidths of the three different models as the gratings reduce in length.

It is noted in Figure 4-18 that the starting bandwidth of the three traces do not all align equally. The reason for this is that the gratings representing the strength and asymmetry traces were apodised gratings, with a shorter effective length, giving rise to a higher bandwidth than the non-apodised grating used for the length trace.

Each of the three effects has been represented as its own individual grating. For a rigorous quantitative model, it would be required that each of the effects were described by an equation, such as equation (4-10). This would be possible with weak gratings where the grating may be approximated as a low reflectivity

gaussian but such a technique would break down for strong gratings. Therefore, these three effects can only really give a qualitative insight to what effects the bandwidth as an apodised grating decays. The overall quantitative result may be calculated by using one of many modelling methods but they will not give any physical understanding as to how the structure of the grating directly effects the bandwidth. The three models may be combined to give an overall picture to how the bandwidth would change when considering all three aspects, as shown in Figure 4-19.

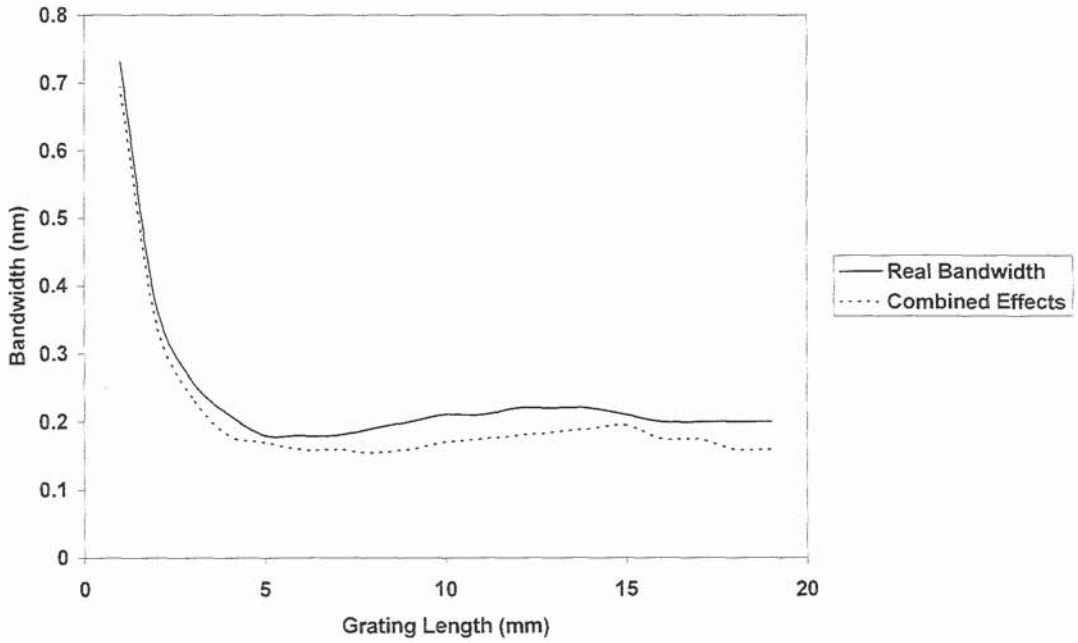

Figure 4-19: Real experimental data plotted with the bandwidth data from combining the three different theoretical bandwidth factors.

The factors are combined with arbitrary amplitudes as it is difficult to gauge the amplitude response of each effect when all three are operating simultaneously. By optimising the amplitudes of the three aspects a shape very similar to the real bandwidth data can be achieved.

4.3 Damage Detection System

The wear sensor may be utilised in another form, one where the damage to the sensor occurs towards the centre of the CFBG rather than at the end. When such a sensor is measured from both ends, the size and position of the damage may be recovered in exactly the same way as for calculating the amount of wear. For a damage detection system (4-7) can be rewritten as

$$D = \frac{\lambda_2 - \lambda_1}{n_{eff} C} \tag{4-11}$$

where D is the size of the damaged hole, λ_2 the high wavelength where the edge of the hole occurs and λ_1 the low wavelength edge of the hole.

A CFBG was broken so that the centre section of the grating had about 10mm removed. The aim of this break was to simulate damage occurring on a bulk material where a hole is punctured through the material. By measuring the CFBG from both the low and high wavelength ends, Figure 4-20, the size of the hole can be calculated using equation (4-11).

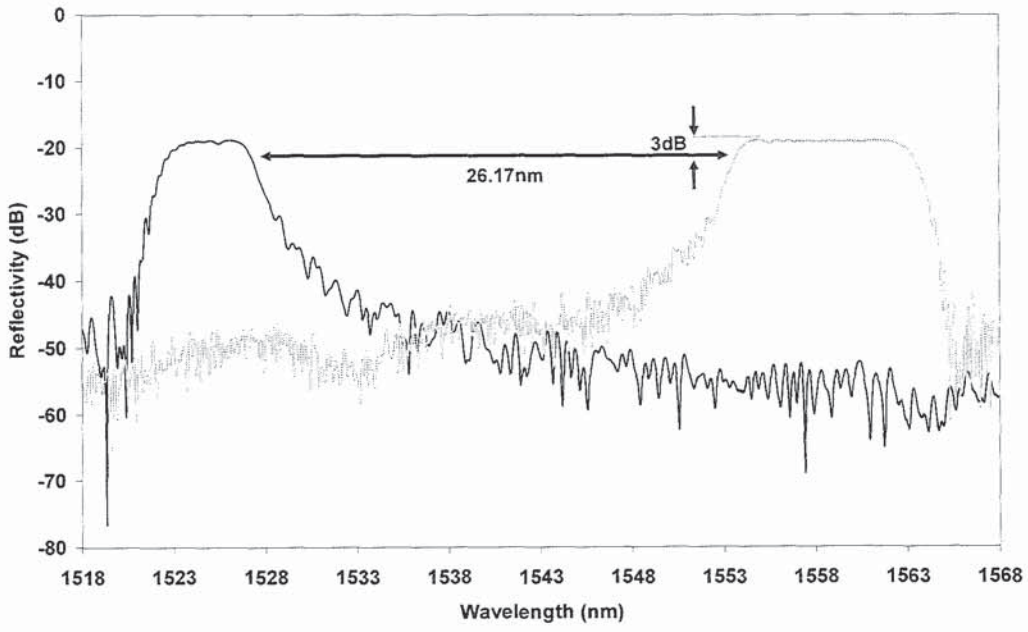

Figure 4-20: CFBG measured from both the long (grey) and short (black) wavelength ends.

The measurement of the CFBG from both ends shows that 26.17nm of bandwidth from the centre of the grating is missing. This equates to a loss of 11.28mm from the centre of the grating. Furthermore, information about the position as well as the size of the hole may be obtained. By knowing the exact start point of the grating, the position of damage along the length of the CFBG may also be calculated using the same method as applied in equations (4-7) and (4-11). The hole is calculated to start 2.04mm from the low wavelength end of the CFBG.

The method presented utilises a 20mm long CFBG, which would tend to be unsuitable for a practical application due to the short length. However, there are few physical limits to the maximum length of grating that can be written. Gratings over 1 meter long have been previously demonstrated [4]. Such devices could find themselves embedded within aircraft wings or ship's hulls in order to detect small fractures or even holes within the structure if they can be accurately made with lengths greater than 1 meter.

4.4 Summary

Two methods of using CFBGs as optical wear sensors have been presented, one utilising a spectral measurement system and the other a photodiode. The experimental results have show that CFBGs may be used as a wear sensor with accuracies in the order of 120μm. It has also been shown that the standard deviation of the results dropped as the chirp rate increased. This resolution is not a fair reflection of the resolution that would be realised within a real device. In order to gain length measurements, certain random and systematic errors will be present. For a real-life application only one measurement; 3dB bandwidth or reflected power would be measured, so increasing the resolution of the device by cutting out the random and systematic errors from the length measurements.

Depending on the application, the wear sensor can be designed to suit the needs of the required measurement. For example, if a cheap sensor is required then the photodiode variation may be used, though, sacrificing resolution. If high-resolution measurements are needed then a high quality measurement system and an extremely highly chirped grating could be used.

With the advancement of studies into embedding fibre optics into metals [52] the CFBG wear sensors present themselves with a unique opportunity. They are currently the only wear sensors that can be embedded within an object to give real-time measurements of the wear taking place. Other environments where an optical sensor, rather than an electrical sensor, comes to the front is within combustible environments such as the oil and gas industries. These advantages coupled together present the CFBG wear sensor as a versatile device for a wide range of applications.

The use of uniform and apodised FBGs were investigated and shown not to be as useful as a CFBG wear sensor. Despite their failure as wear sensors, interesting behaviour was observed as the apodised gratings decayed. This behaviour was shown to be most likely due to a changes in the length, strength and the symmetry of the grating.

By adapting the concept of a wear sensor, a damage detector was also demonstrated. Such a sensor is capable of rapidly detecting the location and size of damage to sub-millimetre precision.

Despite the relatively high cost of CFBGs as individual devices they can return invaluable information on the condition of a material which they are embedded in. This information could be used as a way of maximising the use of an unacceptable wearing material, such as a drill bit or simply as an early warning system for when a level of risk is encountered. The wear sensor could easily pay

for itself by allowing longer running time on a drilling rig or more importantly by increasing safety. Implementation within oil drilling style drill bit would require the entire sensing system to be housed within the drill bit, a concept currently used in the hub of wind turbines to sense the strain on the blades. A dill bit would not require as high a resolution as has been presented, probably requiring 0.5mm resolution.

5

Chirped Moiré FBG Sensors

As optical interrogation technology has progressed, the ability and complexity of FBG sensor systems has equally followed track. Many limitations behind older sensing devices were due to an inability to rapidly interrogate the sensor or array of sensors. With modern day technology, it is possible to retrieve signals from huge arrays of FBG sensors or to give very high resolution results from a single sensor. With this higher resolution, sensors with an extremely high finesse can be measured, such as a highly chirped Moiré FBG (CMFBG). This chapter demonstrates the use of such a CMFBG as a distributed load, temperature and strain sensor.

5.1 Background

A Moiré structure is one where two sinusoidal periods with different frequencies are superimposed upon each other. This superposition causes a beat effect due to

the sinusoids passing in and out of phase with one another, as shown in Figure 5-1.

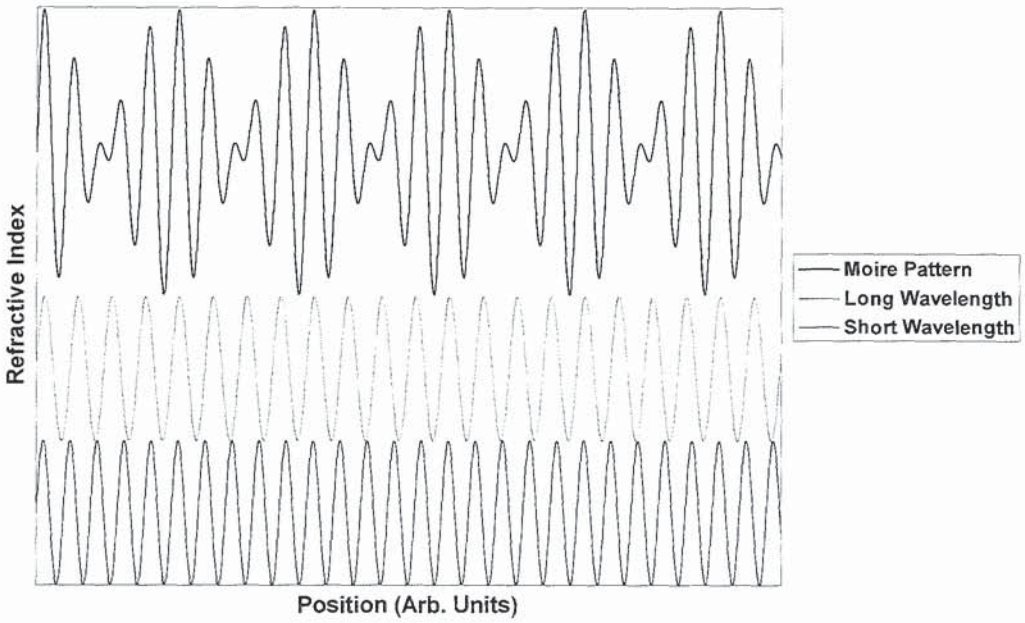

Figure 5-1: Two different period sinusoids creating a Moiré pattern.

Such structures have been investigated with FBGs where two identical FBGs were overwritten but the second grating inscribed with the fibre under a higher strain [53]. Consequently, this forced the wavelength of the second FBG to be written at a lower wavelength than the first FBG. Hence the Moiré pattern was written into the core of the fibre. At the points where the beat effect causes a null point, a phase shift was created. These phase shifts create sub-gratings which are π out of phase with one another, which act as wavelength selective Fabry-Perot resonators.

Although these Moiré FBGs were an interesting academic activity, little application could be found for such devices. They showed little promise beyond that already demonstrated by multiple FBGs or phase shifted FBGs and proved slightly more difficult to accurately make. As the two gratings are overwritten, the amount of hydrogen available to facilitate the refractive index change of the second FBG is difficult to control. This ultimately led to lower quality gratings being written, with little advantage over other available techniques. Aston

University's Photonics Research Group demonstrated a number of potentially useful applications by advancing the idea of the Moiré FBGs by introducing a chirp factor, producing chirped Moiré FBGs [54]. The principle used was identical to the fabrication of standard Moiré FBGs; inscribing a chirped FBG over another chirped FBG under strain. Therefore a chirped Moiré pattern is written, shown in Figure 5-2.

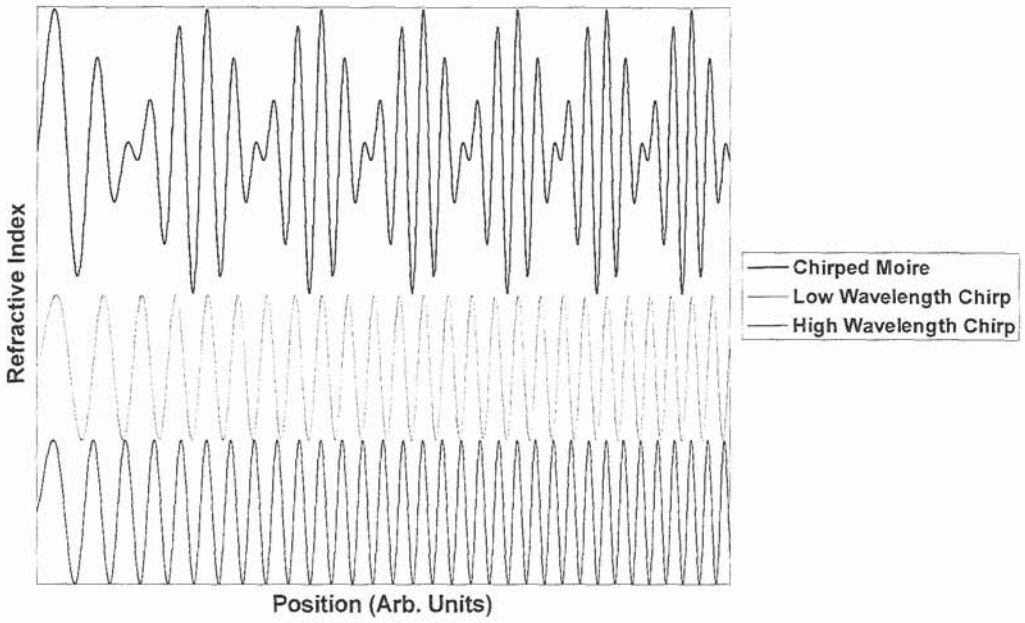

Figure 5-2: Two differently chirped sinusoids creating a chirped Moiré pattern.

As with the standard Moiré pattern, a beat effect is created with the superposition of the two chirped gratings giving localised π-phase shifts. However, the spectral location of these phase shifts depends on their physical location within the grating due to the chirp, unlike a standard phase shifted grating. The spectral phase shift will occur at the wavelength which is supported by the surrounding fringes. The refractive index profile of a Moiré grating is defined by [7]:

$$\Delta n(z) = 2\delta n\left[1+\cos\left(\frac{2\pi z}{\Lambda_a}\right)\cos\left(\frac{2\pi z}{\Lambda_b}\right)\right] \tag{5-1}$$

Where δn is the dc offset of the refractive index, z is the position along the fibre axis, Λ_a and Λ_b are defined by equations (5-2) and (5-3) respectively.

$$\Lambda_a = \frac{2\Lambda_1\Lambda_2}{(\Lambda_1 + \Lambda_2)} \tag{5-2}$$

and,

$$\Lambda_b = \frac{2\Lambda_1\Lambda_2}{(\Lambda_1 - \Lambda_2)} \tag{5-3}$$

Λ_1 and Λ_2 are the periods of the two superimposed gratings, for a chirped grating they are expressed as a function of z. Λ_b is the period of the slowly varying envelope, from this the spatial separation of each phase shift of the device is given by

$$\Delta z = \frac{\Lambda_b}{2} \tag{5-4}$$

It is then possible to calculate the number of phase shifts formed in the CMFBG using

$$N = \frac{L}{\Delta z} \tag{5-5}$$

Since the grating is chirped, the spacing between the phase shift, Δz, varies slightly with position.

5.2 Fabrication Of CMFBGs

A CMFBG was fabricated using a 244nm frequency doubled CW FreD laser with a phase mask fabrication technique. The 25mm long grating was inscribed into hydrogenated SMF-28 using a double scan technique [53]. The phase mask had a chirp rate of 1.6nm/mm.

An initial chirped grating was written, the fibre strained and then a second chirped grating written directly over the first grating. The straining gave a 5nm difference in the central wavelength of the two gratings. The resulting grating had a transmission loss of -7dB and a bandwidth of 50nm, as shown in Figure 5-3.

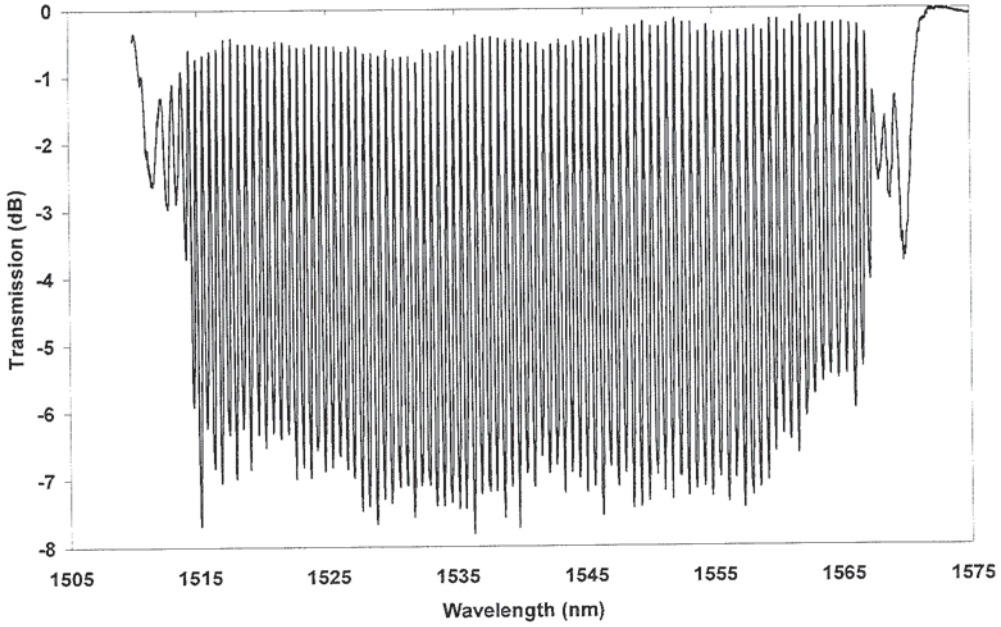

Figure 5-3: Transmission profile of the 25mm long CMFBG.

5.3 Load Sensor

To date, no work has been conducted on the use of CMFBGs as distributed load sensors. Load sensors have been studied using a number of different fibre grating structures, including: uniform FBGs [55], pi-phase shifted FBGs [56], chirped fibre gratings [57], sampled FBGs [58] and long period gratings (LPGs) [59,60]. Most of these techniques allow either the applied load or the position of the load to be measured, but never both simultaneously. The method proposed theoretically by Torres *et al* [55] and demonstrated experimentally by Tjin *et al* [57] allows both load and position to be measured but it proves difficult to define the footprint accurately. This section presents a distributed load sensor capable of accurately retrieving the magnitude, position and footprint of the load being applied transverse to the fibre.

5.3.1 Position and Footprint Sensing

A loading device was used to apply a transverse load to the optical fibre's longitudinal axis. The device consisted of two parallel metallic plates with the CMFBG between them. To maintain an even load distribution, a second piece of fibre was placed along side the grating. This ensured that any load was applied through the vertical plane with no horizontal component. The CMFBG was connected to an Agilent 8164A Lightwave Measurement System and a circulator to allow transmission and reflection measurements, as shown in Figure 5-4.

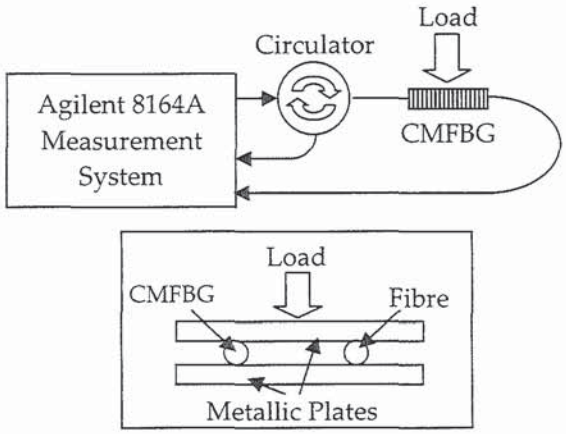

Figure 5-4: Experimental setup to apply a load to a CMFBG.

When load is applied to the CMFBG a red shift in wavelength and a change in amplitude occurs around the point where the load is applied, as shown by Figure 5-5. For this demonstration the length of the loading element was only a fraction of the length of the CMFBG.

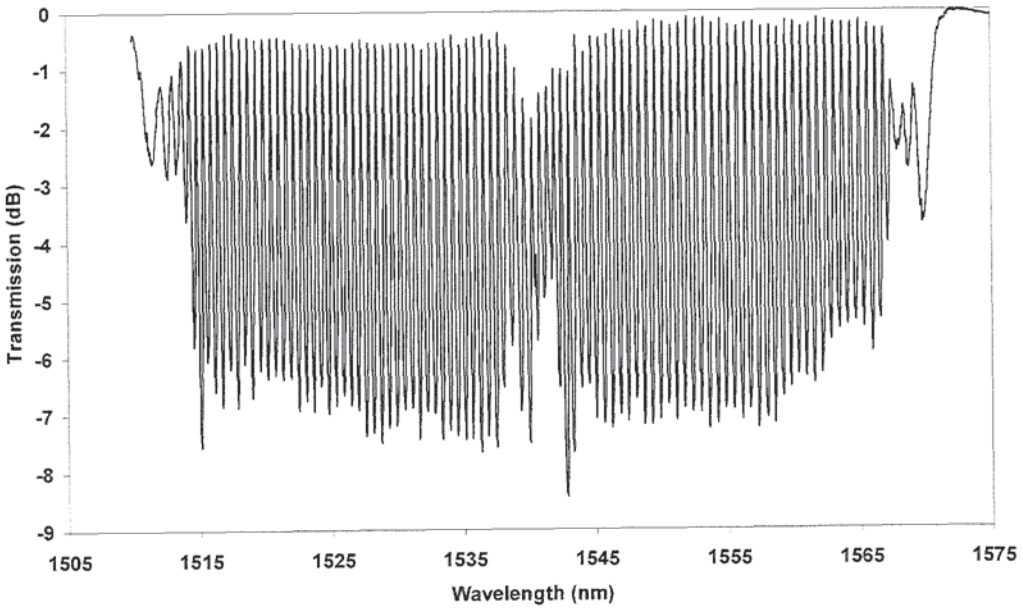

Figure 5-5: CMFBG spectrum as a load is applied to the centre.

Looking more closely at the central section of the loaded CMFBG, Figure 5-6 clearly shows the red shift and the reduction in the amplitude of the phase shifts. The wavelength shift and amplitude reduction are due to the phase shifts starting to split as the birefringence of the fibre increases, this will be explained in detail in section 5.4.

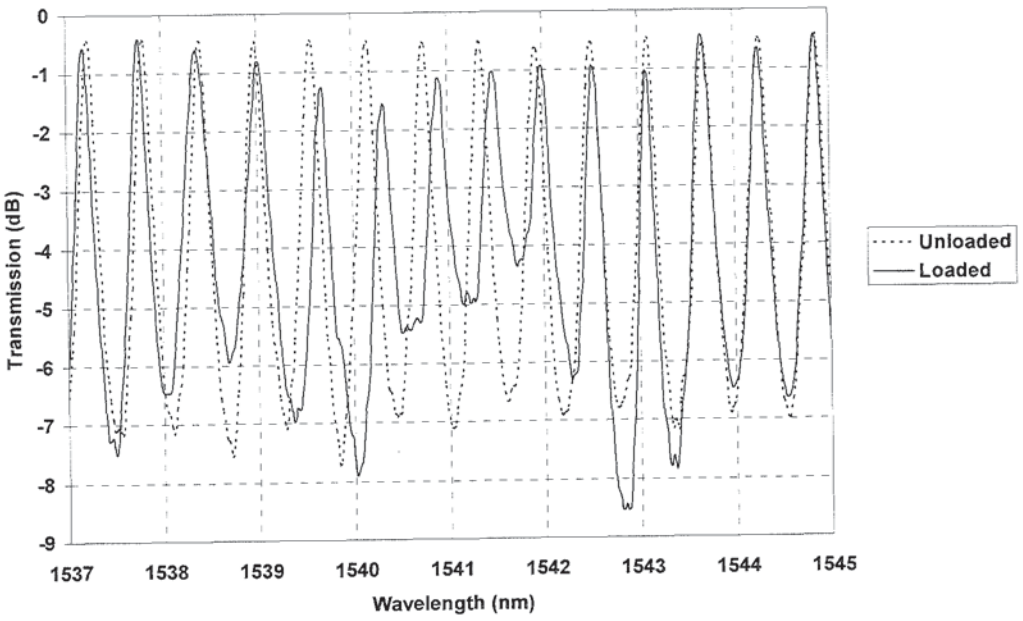

Figure 5-6: Close-up view of the spectral change as a load is applied.

Due to the grating being chirped, each wavelength corresponds to a physical position along the grating. Since the phase shifts occur at discrete wavelengths within the fibre, their physical position may be calculated. The wavelength of the grating can be converted to position using (4-7). By measuring the position of the phase shifts for which this red shift occurs, the position and footprint of the load on the grating may be found, Figure 5-7. The graph was produced by measuring the transmission spectrum using the Agilent 8164A Lightwave measurement system before and after load was applied to grating. The wavelength range and the number of data points was identical for both measurements. Each data point was then compared before and after to identify the wavelength shift that each point had undergone.

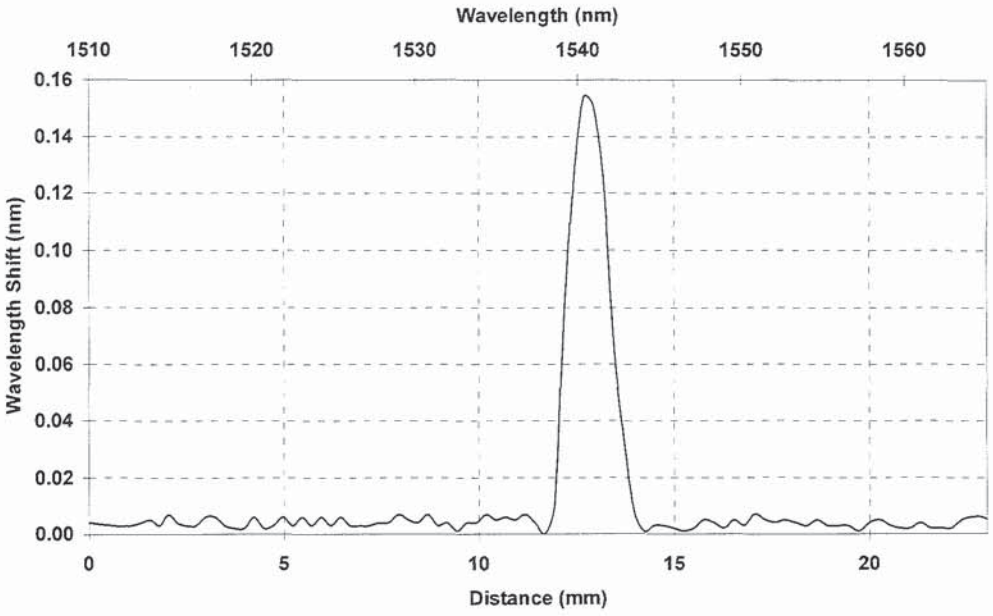

Figure 5-7: The wavelength shift of the pass bands as load is applied. Shown both as a function of wavelength and distance along the CMFBG.

For the CMFBG shown in Figure 5-3, the spacing at 1515nm is 158μm and at 1565nm the spacing is 169μm. This implies that the spatial resolution of the device is different for each point along the grating length. Practically, this is not a problem since the difference is insignificant to the size of any loading element. The mean spatial resolution, purely from the spectrum of the device, is 164μm. To

date, this is the highest spatially resolved chirped Moiré grating. Previously, the highest reported value was by Doucet *et al* [61] with a spatial resolution value of 500μm.

Using (4-7) the footprint of the loading element is calculated as 2.54±0.16mm, which is in excellent agreement with the direct measurement of 2.50±0.25mm, measured using a ruler.

An important point to note is that this technique of measuring the wavelength shift is not capable of detecting the load magnitude accurately; due to unresolved peak splitting that occurs. The next section will explain this peak splitting and present an accurate way of measuring the amplitude of the load using this splitting.

5.4 Load Sensing

When a transverse load is applied to a waveguide the refractive index changes by an effect known as the photoelastic phenomenon [62]. As the load is not applied isotropically the waveguide is deformed, causing refractive index changes and consequently creating birefringence. The magnitude of a transverse load on a waveguide may be calculated using the effect of birefringence, as demonstrated by LeBlanc *et al* [56]. They showed that as a load was applied to a phase-shifted FBG, the phase shift spectral peaks would split into two peaks corresponding to the induced fast and slow axes of the grating. These fast and slow axes refer to x- and y-polarised light respectively. This peak splitting is demonstrated using the CMFBG from Figure 5-3 and applying a load to the centre of the grating. Figure 5-8 shows the transmission profile of the loaded CMFBG, zoomed in around the region where load was applied.

Figure 5-8: Pass bands splitting due to induced birefringence whilst under load.

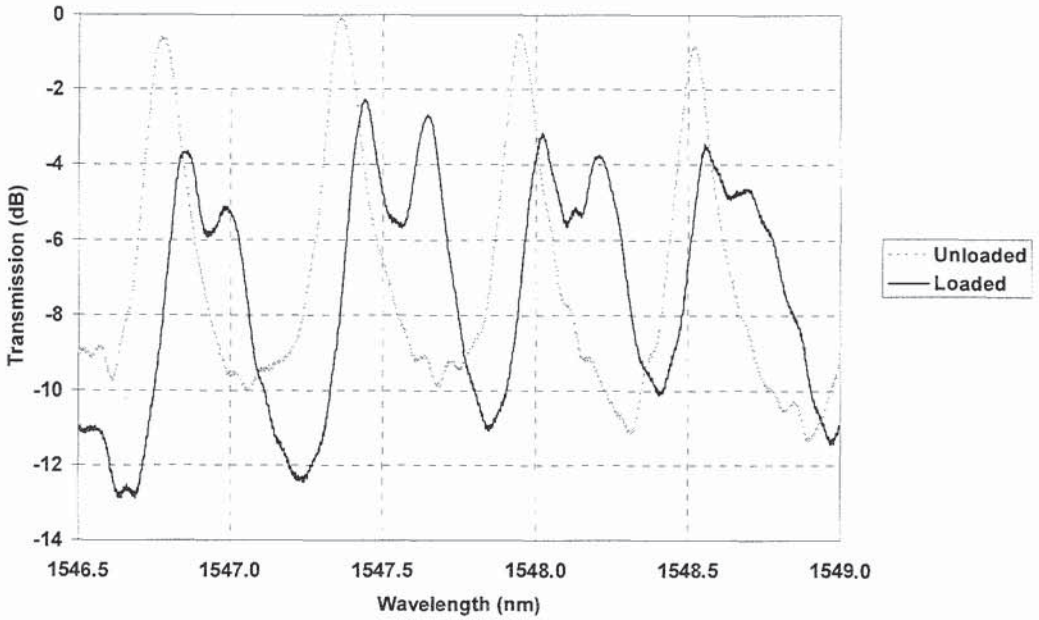

The birefringence, B, causing the phase shift splitting can be calculated from the equation [56]

$$B = \frac{\Delta n}{\overline{n}} = \frac{\Delta \lambda}{\overline{\lambda}} \tag{5-6}$$

Where $\Delta\lambda$ is the spectral separation of the two peaks and

$$\Delta n = n_1 - n_2 \tag{5-7}$$

is the difference of the index of refraction between the slow and fast axes of the grating, $\overline{n}$ is the average index of refraction of the grating core and

$$\overline{\lambda} = \frac{\lambda_1 + \lambda_2}{2} \tag{5-8}$$

is the average wavelength of the grating with λ_1 and λ_2 being the wavelengths of the two split peaks. As the applied load was increased the peak separation increased and both the peaks shifted towards higher wavelengths, as shown by Figure 5-9.

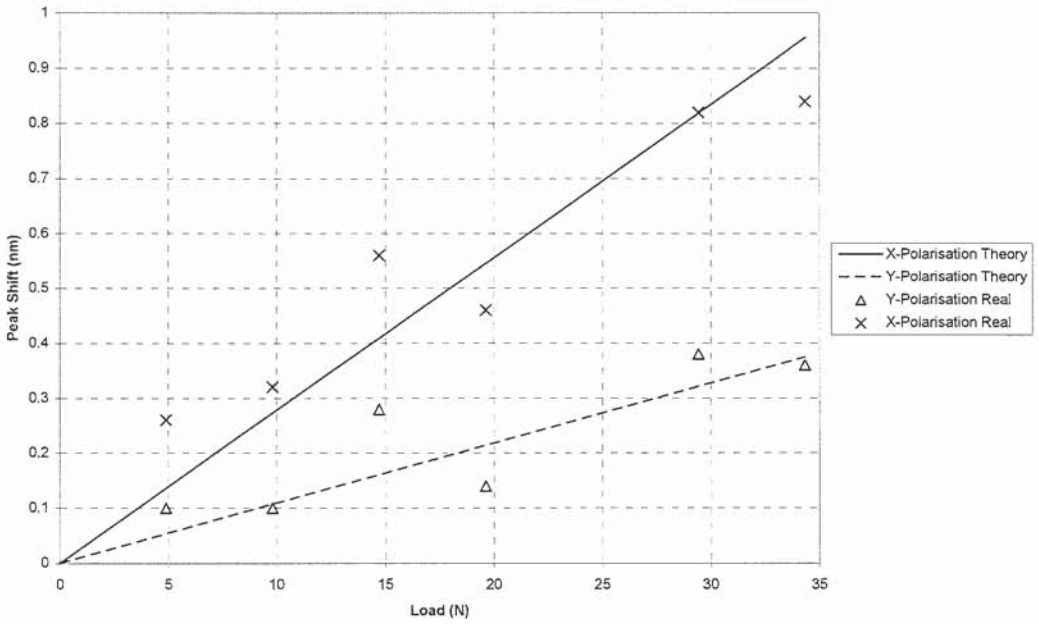

Figure 5-9: Experimental and theoretical results showing the peak shift as increasing load was applied.

The experimental shift measurements agree well with the theoretical calculations. In order to calculate the wavelength shift for both the x- and the y-polarised states, the stress fields in the x- and y-axes need to be calculated. The limits of this are defined by the fibre geometry; a cylindrical object with a radius of 62.5μm and a length equal to the loading element. These stress fields are given by [62]

$$\sigma_x(x,y)=\frac{-2F}{\pi L}\left\{\frac{x^2(b+y)}{\left[x^2+(b+y)^2\right]^2}+\frac{x^2(b-y)}{\left[x^2+(b-y)^2\right]^2}-\frac{1}{2b}\right\} \tag{5-9}$$

And

$$\sigma_y(x,y)=\frac{-2F}{\pi L}\left\{\frac{x^2(b+y)^3}{\left[x^2+(b+y)^2\right]^2}+\frac{x^2(b-y)^3}{\left[x^2+(b-y)^2\right]^2}-\frac{1}{2b}\right\} \tag{5-10}$$

Where x is the position along the fibre in the x-axis, y the position along the fibre in the y-axis, F the applied force, L the length for which the force is

applied over and b the radius of the fibre. These calculated stress fields are shown in Figure 5-10 and Figure 5-11.

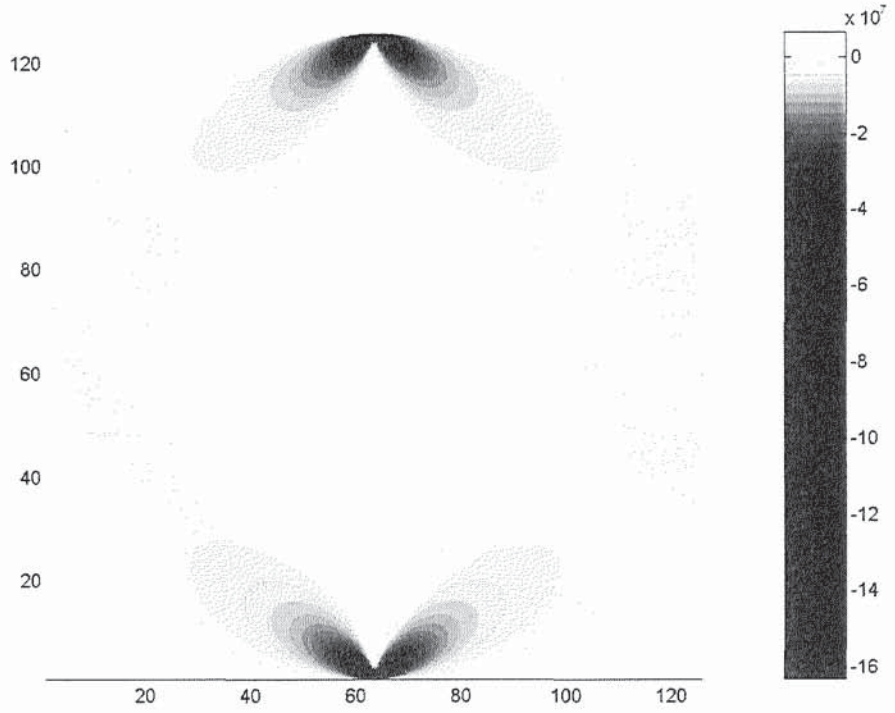

Figure 5-10: Stress field in the x-axis. The x- and y- axes are the x- and y-dimensions of the cross section of the grating. The z-axis represents the stress field along the x-axis.

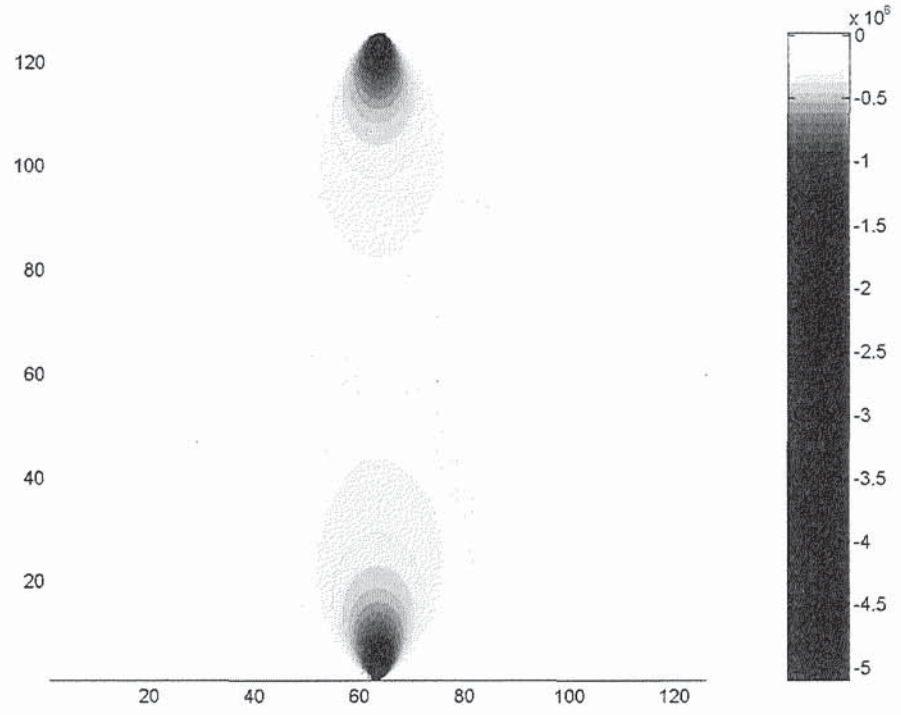

Figure 5-11: Stress field in the y-axis. The x- and y- axes are the x- and y-dimensions of the cross section of the grating. The z-axis represents the stress field along the y-axis.

From knowing the stress fields the shift in the Bragg wavelength for each polarisation state may then be calculated using

$$\begin{aligned}\left(\Delta\lambda_B\right)_x\left(x,y,z\right) &= -\frac{\left(n_{eff,0}\right)^3\Lambda_{B,0}}{E} \\ &\times\left\{\left(p_{11}-2\nu p_{12}\right)\sigma_x\left(x,y,z\right)+\left[\left(1-\nu\right)p_{12}-\nu p_{11}\right]\times\left[\sigma_y\left(x,y,z\right)+\sigma_z\left(x,y,z\right)\right]\right\} \\ &+2\frac{n_{eff,0}\Lambda_{B,0}}{E}\times\left\{\sigma_z\left(x,y,z\right)-\nu\left[\sigma_x\left(x,y,z\right)+\sigma_y\left(x,y,z\right)\right]\right\}\end{aligned} \quad (5\text{-}11)$$

And

$$\left(\Delta\lambda_B\right)_y\left(x,y,z\right)=-\frac{\left(n_{eff.0}\right)^3\Lambda_{B.0}}{E}$$
$$\times\left\{\left(p_{11}-2\nu p_{12}\right)\sigma_y\left(x,y,z\right)+\left[\left(1-\nu\right)p_{12}-\nu p_{11}\right]\times\left[\sigma_x\left(x,y,z\right)+\sigma_z\left(x,y,z\right)\right]\right\} \quad (5\text{-}12)$$
$$+2\frac{n_{eff.0}\Lambda_{B.0}}{E}\times\left\{\sigma_z\left(x,y,z\right)-\nu\left[\sigma_x\left(x,y,z\right)+\sigma_y\left(x,y,z\right)\right]\right\}$$

Where $n_{eff,0}$ is the initial effective refractive index of the undisturbed core, p_{11} and p_{12} the photoelastic coefficients of the undisturbed optical fibre, E the Young's modulus and ν the Poisson's coefficient and

$$\sigma_z=\upsilon\cdot\nu(\sigma_x+\sigma_y) \quad (5\text{-}13)$$

Where υ is a correction coefficient to account for friction between the fibre and the loading surfaces [63], in this case a value of 0.73 was used. A value of υ = 0 implies that there is no friction so in a state of plane stress and a value of υ = 1 means that the fibre is in a state of plane strain or in other words, the ends are fixed. A value of 0.73 was chosen as it allows the theoretical values to closely fit the experimental data. The previously reported value by Zhang *et al* [63] was 0.8. Using equation (5-6) the birefringence induced by the transverse load may be calculated, this is shown in Figure 5-12.

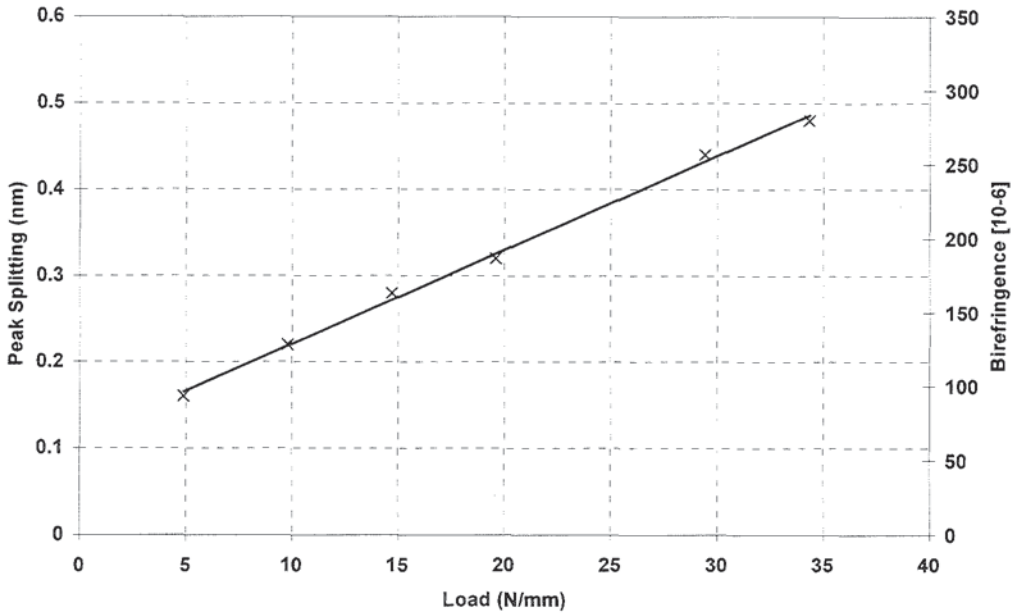

Figure 5-12: Variation of peak splitting and birefringence with applied load, also shown as a function of transverse strain.

The trend of the line in Figure 5-12 suggests that extrapolating the line back to a zero load would give a peak shift value of about 0.1nm. From Figure 5-3 there is no initial peak shift, discounting the idea of the fibre having an intrinsic birefringence due to either fibre design or due to the UV exposure. There may possibly be some non-linear behaviour in the low load regions as the fibre deformation would be more pronounced during these early stages.

The Agilent measurement system is capable of measuring the peak separation to a resolution of 2pm. Since the gradient of the slope is 27.3pm/(N/mm) the resolution of the loading experiment is 0.07N/mm thus giving a transverse strain resolution of 24με. By knowing the gradient of Figure 5-12 the load of an arbitrary object, on top of the CMFBG, may be calculated by measuring the phase shift separation, as shown in Figure 5-13.

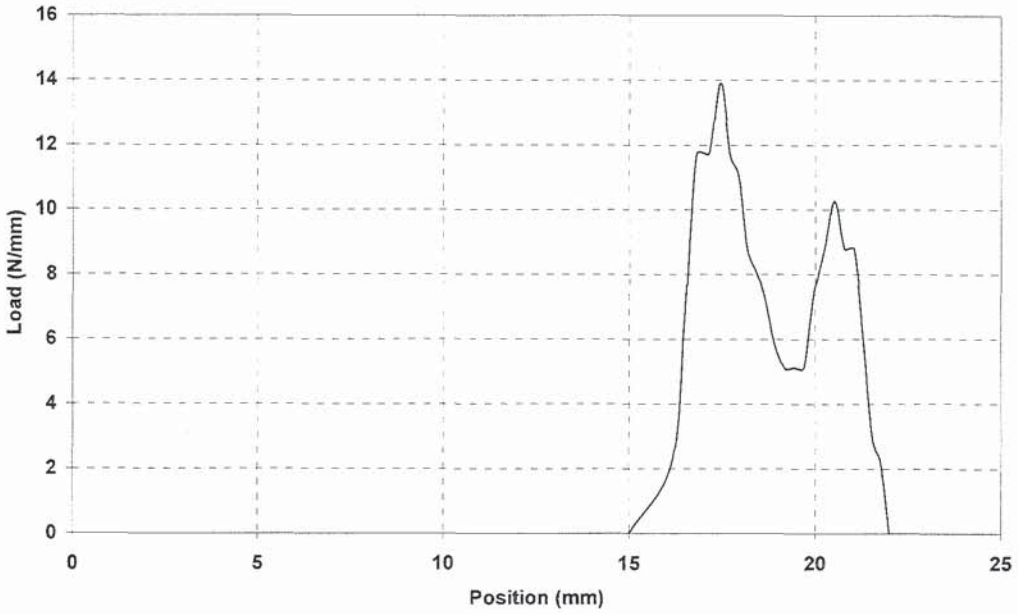

Figure 5-13: Load distribution of an arbitrary object placed on the CMFBG.

The loading element was a 7mm wide piece of aluminium placed at one end of the CMFBG. Figure 5-13 indicates that the maximum load was 14N/mm and that there was not a constant load across the entire length of the aluminium block. This is probably due to the surface of the block not being perfectly flat.

5.5 Load Sensor Summary

A device to give a distributed measurement of the magnitude, position and footprint of a transverse load has been experimentally demonstrated. The CMFBG presented has an extremely high average spatial resolution of 164μm and a loading resolution of 0.15N/mm or 50με. The device presented covers a short spatial range but it is possible to fabricate such gratings over a longer length. Such a grating would lose spatial resolution if fabricated with the same chirp rate. Therefore there is a direct trade off between spatial resolution and length of the grating. However, any application requiring a longer grating would probably not require such a high resolution.

5.6 Temperature Sensor

Fibre optic temperature sensors have been demonstrated using a variety of techniques such as low-coherence reflectometry [64], uniform fibre Bragg gratings [65] and long period gratings [66]. Most of these techniques suffer from an inability to give an accurate distributed temperature measurement. The use of Moiré gratings as sensors has not been widely exploited, the most notable work being conducted by Chisholm *et al* [67,68]. The method presented here utilises a chirped Moiré fibre Bragg grating (CMFBG) where the pass bands are monitored to give an accurate measurement of the temperature distributed across the length of the grating. Two systems are presented allowing the versatility of one- or two-dimensional distributed temperature sensing.

5.6.1 1D Temperature Sensing

The CMFBG was placed entirely on top of a Peltier heater and connected to an Agilent 8164A Lightwave measurement system via a circulator in order to measure the temperature response, Figure 5-14 (top and bottom left).

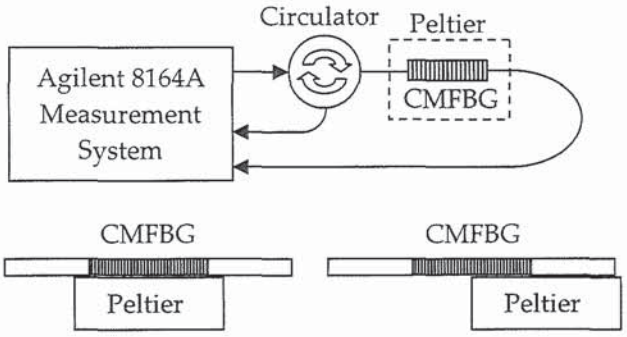

Figure 5-14: Optical setup showing two configurations for the CMFBG on top of the Peltier. The entire CMFBG over the Peltier (bottom left) and only half the CMFBG over the Peltier (bottom right).

The wavelength of each of the pass bands was monitored as the CMFBG was heated between 24°C and 70°C. Each pass band was observed to behave with the

same response to temperature. Figure 5-15 shows the thermal response of one of the peaks, originating at 1541.6nm.

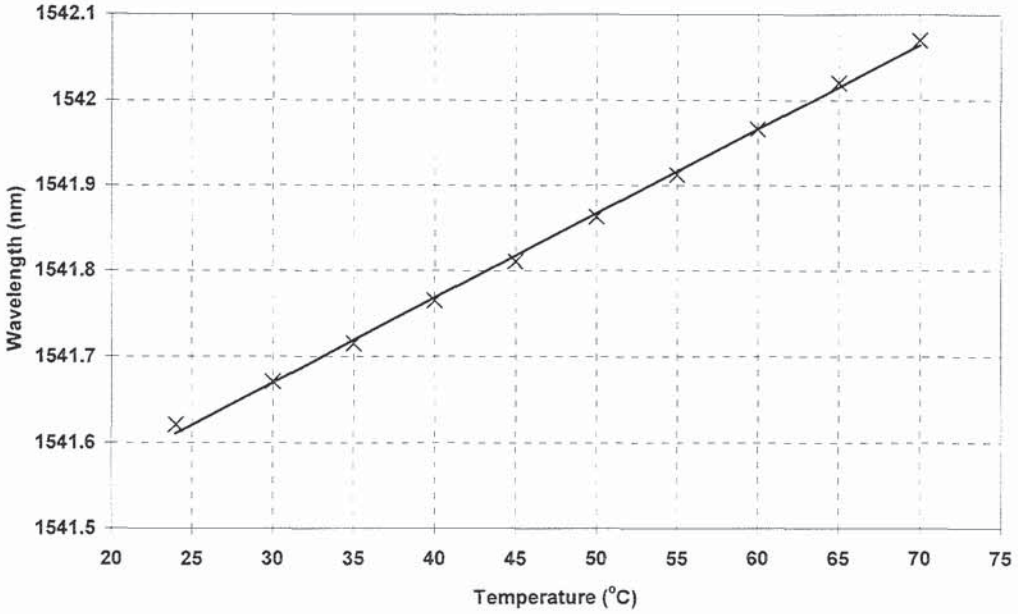

Figure 5-15: Linear response of one pass band with temperature.

The phase shifts move with temperature in an identical manner as the central wavelength of an FBG. This shift is partly due to the thermal expansion of the fibre, causing an increase in the grating's fringe spacing, and partly due to a change in the refractive index of the fibre. The relation between the wavelength shift, λ_B, and the change in temperature, ΔT, is given by [69]

$$\Delta\lambda_B = \lambda_B(\alpha_\Lambda + \alpha_n)\Delta T \tag{5-14}$$

where α_Λ is the thermal expansion coefficient, α_n is the thermo-optic coefficient.

The gradient of the thermal response is 9.9±0.4pm/°C, which is in good agreement with previous work on FBGs [70,71] that quote values of between 8.9pm/°C and 13.7pm/°C, respectively. These values vary due to the use of different types of fibres, which have varying fibre geometries and dopant concentrations. The

Agilent measurement system has a maximum scan resolution of 2pm which gives a temperature resolution of 0.2°C.

With the knowledge of the thermal response of the fibre and the wavelength to position conversion, see Chapter 4, the CMFBG may be used as a distributed temperature sensor in one dimension (along the fibre axis). To demonstrate this, the grating was placed half on the Peltier heater and half off as shown in Figure 5-14 (bottom right) and the temperature lowered from +85°C to –12°C. This subsequently gave a variable thermal profile across the length of the CMFBG. Each pass band was monitored and the wavelength shift, away from the initial 25°C spectrum, recorded. This wavelength shift was then converted to temperature using the gradient obtained from Figure 5-15. The results are shown in Figure 5-16.

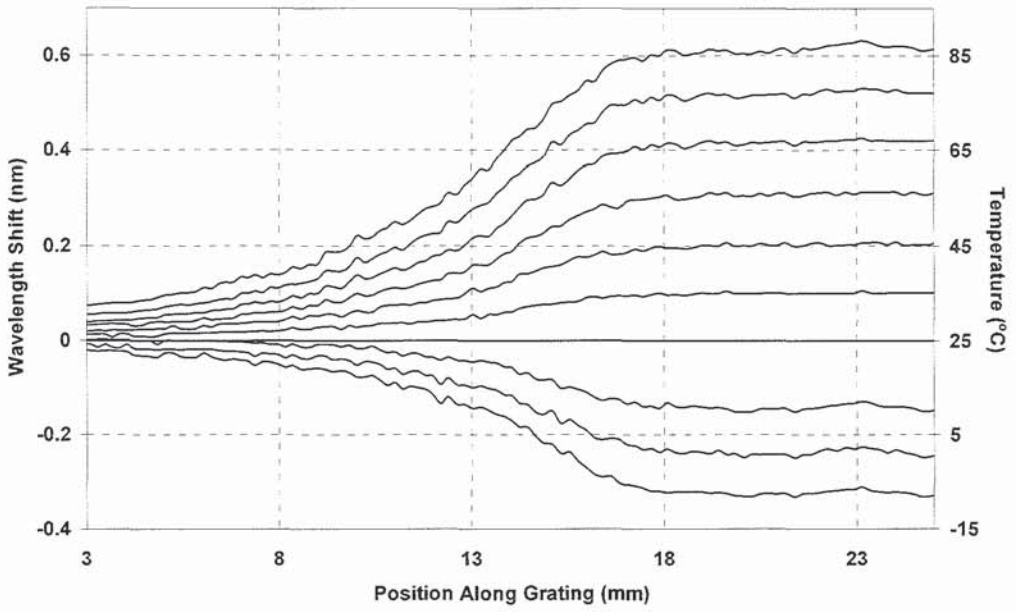

Figure 5-16: Thermal response of each phase shift with temperature when the CMFBG is placed half on the Peltier and tuned between +85°C and –12°C.

It is clear to see that, for any given temperature, the CMFBG is able to record the temperature of the Peltier heater on the right hand-side of the grating and also show the thermal decay of temperature away from the left-hand side of the device.

5.7 2D Temperature Sensor

In order to give a more detailed description of a heating element, a number of CMFBGs may be used in parallel to give a two dimensional thermal profile. Ten CMFBGs were suspended parallel to each other with a spacing of 2mm between them and a temperature controlled soldering iron supported about 5mm above at 180°C, as shown in Figure 5-17.

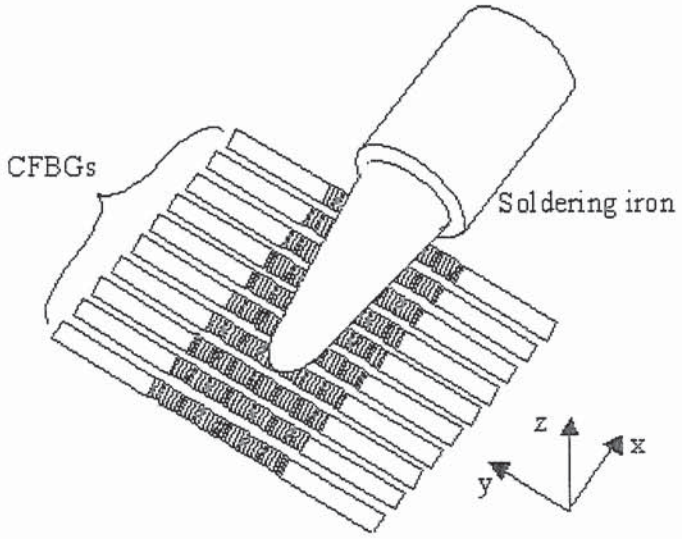

Figure 5-17: Schematic of the experimental lay-out showing the soldering iron above an array of CMFBGs.

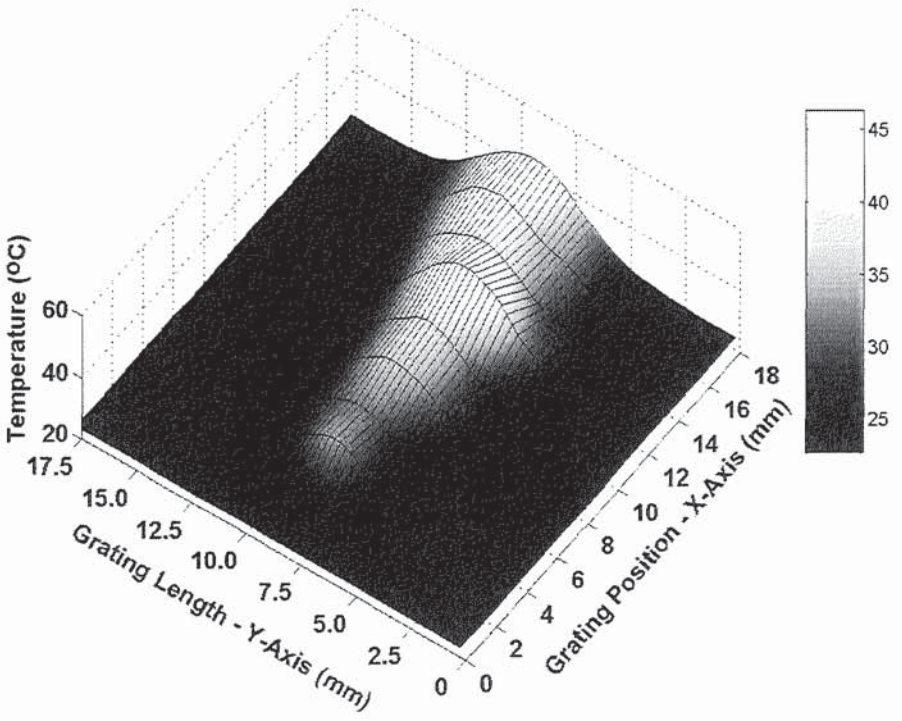

Figure 5-18: Thermal response of the ten CMFBGs with a soldering iron suspended above them.

The thermal profile obtained, Figure 5-18, clearly represents the shape of the soldering iron and shows how the temperature decays away. Each grating was measured in turn to obtain the full 2D profile. The resolution in the x-axis is limited by the spacing between the fibres, in this case 2mm. The minimum separation possible would be achieved by placing bare fibres, with the protective polymer layer removed, next to one another. This would allow the separation to be reduced to 125μm, the diameter of the cladding of the fibre. A second 2D array can be interleaved with the current array at a 90° orientation so that complete mesh would be obtained. The results from the two sets of 2D arrays can then be combined and averaged. However, any method of operation chosen is strongly dependant on the application needs. There is little need to have the fibres spaced by 125μm if the total length to be covered is more than a few centimetres. The gratings were not multiplexed together, instead measured one by one.

At grating length 7mm and grating position 12mm within Figure 5-18, a slight extension of the heating element is present on the y-axis. Upon closer inspection of the soldering iron it was obvious that there was a spot of solder left on the iron. The solder acted as a thermal leakage and hence showed up in the measurement. This could be useful in checking manufacturing quality of heating elements. This technique has a far higher spatial resolution than standard thermal cameras, however it is not capable of measuring the thermal profile from a large distance away unlike the camera technique.

5.8 Temperature Sensor Summary

A CMFBG has been shown to be useful as a distributed temperature sensor with a thermal response of 9.9±4x0.4pm/°C. The use of a single CMFBG is able to retrieve a 1D temperature profile of a heating element. However, it is much more useful to use the same technique in parallel with a number of different gratings to show the 2D thermal profile of a heating element. Such a device may find applications in medical areas, to detect the size and temperatures of inflamed areas within a body [72,73] or within industry to accurately detect non-uniform heating of a miniature device. A possible application would be as an analytical tool to detect heat leakage from prototype computer chips in order to discover microscopic design flaws.

5.9 Strain Sensor

Fibre Bragg gratings (FBGs) have shown their true versatility within the field of sensing. They are capable of measuring a number of different physical characteristics, often simultaneously [74], and can be distributed over a large area. Strain sensing using FBGs has shown a large amount of commercial and academic interest. They are currently embedded within a range of real-life applications ranging from wind turbine blades to high performance jet aircraft wings. These applications utilise FBGs positioned at strategic points along the measured structure to give a strain measurement from individual points along an

array [75,76]. The technique works well for large structures where spatial resolution is not a priority but fails when high spatial resolution is required. The technique presented in this section provides a higher spatial resolution than those previously published.

Due to the inherent nature of the CMFBG, each pass band corresponds to a unique position along the grating. Therefore the strain, which occurs at any point along the grating, can be measured by monitoring the wavelength shift of the pass bands. It is then possible to give a measurement of not only the strain but also the distribution of the strain across the grating. The wavelength displacement of the phase shifts, $\Delta\lambda$, is given by [7]

$$\Delta\lambda = \lambda_B(1-p_e)\varepsilon_z \tag{5-15}$$

where λ_B is the Bragg wavelength (in this case the wavelength of the phase shift in question), p_e the effective strain-optic constant and ε_z the longitudinal strain.

The CMFBG was super-glued to a thin steel plate, to induce a strain across the grating, a four-point bending rig was employed which bent the steel plate causing a longitudinal strain on the fibre. This type of bending rig can be used to apply either a constant strain or a linear strain gradient. Figure 5-19 indicates that if the grating is placed in region 1 the strain applied will be constant across the length. However, if placed in region 2 the strain will have a linear gradient. The strain across region 1, ε_z, is given by the equation [77]

$$\varepsilon_z = -12(h+\Phi)\frac{W}{\left(4a^2-3L^2\right)} \tag{5-16}$$

where h is the thickness of the plate (0.5mm), Φ is the diameter of the fibre (125μm), W the deflection at the centre of the beam (+12mm to –14mm), a the

distance between the support bar and the nearest loading bar (40mm) and L the distance between the support bars (120mm).

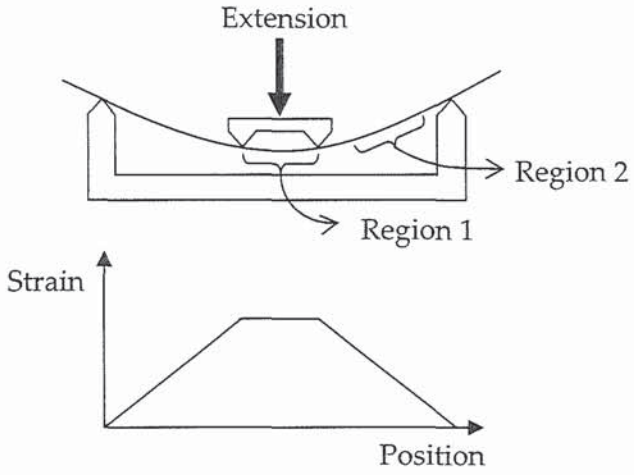

Figure 5-19: Schematic representation of the strain inducing 4-point bending rig.

Placing the CMFBG in region 1 of the four-point bending rig enabled a constant strain to be applied across the grating. To create a positive strain, the plate with the CMFBG secured to it was positioned so that the grating was facing downwards, therefore on the outside of the curvature giving a red wavelength shift. When the plate was deflected, by extending a micron-screw gauge, the pass bands were observed to shift in wavelength linearly with the applied strain, as shown in Figure 5-20.

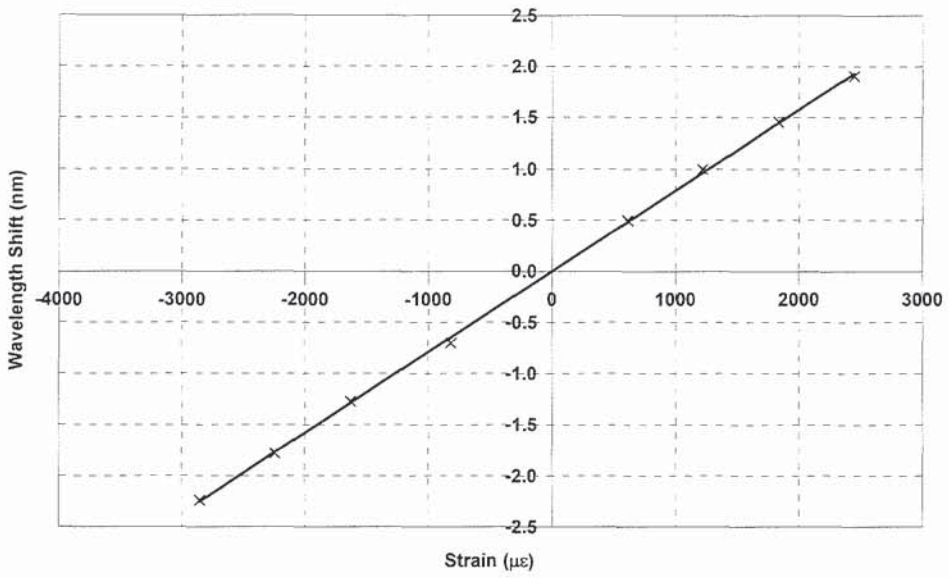

Figure 5-20: Linear strain response of a single pass band within the CMFBG for both positive and negative strains. Only one pass band is shown, each band will respond in approximately the same way.

Turning the plate upside down and repeating the experiment reversed the strain vector giving negative strain, indicating compression, giving a blue wavelength shift. The results show a strong linearity between the shift in wavelength and the strain, as would be expected from (5-15). From the gradient of Figure 5-20, the response of the CMFBG as a strain sensor is given as 0.8±0.01pm/με. Othonos and Kalli [7] quote an anticipated strain sensitivity of 1.2pm/με. The variation in these two values derives from the fact that a drop in the strain sensitivity would be expected when gluing the grating to a metal plate. The combination of the metal, glue and fibre form a more ridged structure than the fibre alone.

The forte of the Moiré method is that it provides a very high spatially resolved distributed sensor. To monitor this distributed strain, each of the pass bands were measured during the straining process. The pass band wavelength information was then converted into position along the grating, x, using (4-7). Therefore the strain at discrete locations along the CMFBG could be monitored. Figure 5-21 shows how the strain increased and decreased across the entire length of the grating as the extension of the screw gauge was altered. Note that there is a small

deviation in the strain towards the central portion of the CMFBG. This is probably due to non-uniform bonding of the fibre to the plate, consequently the fibre is forced further from the plate so creating a higher localized strain gradient.

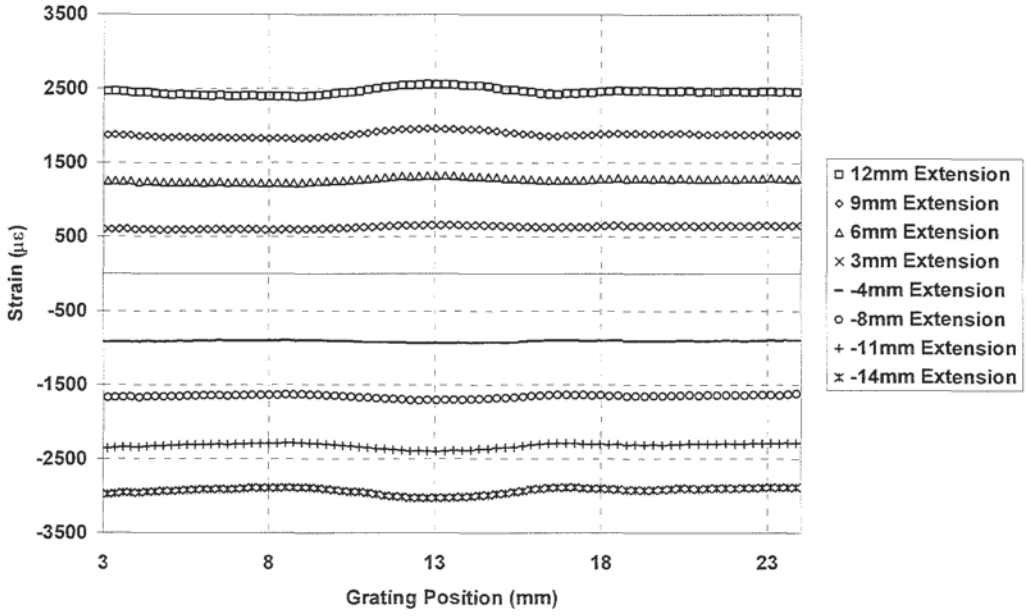

Figure 5-21: Distributed strain measurement across the length of the CMFBG for eight different strain settings when positioned in region 1.

The spatial resolution of the strain measurement is given by the average spacing between the pass bands, which was calculated as 164μm. The pass bands are used as a measure of the resolution as they are points which are simplistic to track. If a curve was fitted to the Moiré pattern then a far higher spatial resolution could be achieved. A higher spatial resolution could be obtained by fitting an expression to the Moiré pattern, though taking longer to analyse the data. By taking the average spacing this is still an extremely high spatial resolution strain sensor; the highest reported value to date. Previously reported values of 3.25mm have been quoted by Gwandu *et al.*

To create a linear strain gradient across the CMFBG the plate was repositioned so that the grating sat within region 2 of the four-point bending rig. The same experiment, as described previously, was repeated in order to create both a negative and positive strain gradient. The grating was placed so that the low

wavelength end was towards the outside of the bending rig and the high wavelength end towards the centre of the rig. The results of which are shown in Figure 5-22.

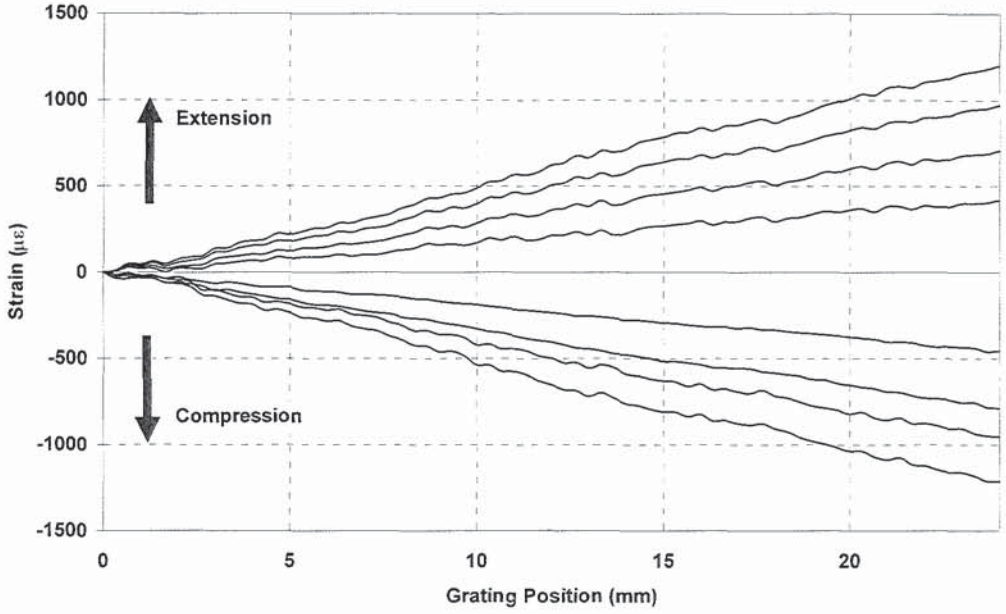

Figure 5-22: Distributed strain measurement for eight different strain settings when positioned in region 2.

It is clear to see, from Figure 5-22, that at the beginning of the grating there was little strain applied. The strain then increased roughly linearly towards the other end of the grating. Any deviations away from a perfect linear relation mainly came from the gluing method. If the glue had a different quantity or density at any point along the CMFBG then that region would have a slightly different strain response. The maximum strain gradient measured was 50με/mm. The maximum strain gradient possible depends on the materials used and the spectral separation of the pass-bands. On a small CMFBG there is little chance that the pass-bands would shift such that two bands overlap. The reason for this is that it is impossible to create a point-source of strain; any force applied near the CMFBG will exert a strain field that will cause all neighbouring pass-bands to shift. For a band to overlap a wavelength shift of 0.36nm, equivalent to ~450με, would be required with no relative shift to the neighbour pass-band. Such a shift

would require a strain gradient of ~2700με/mm, which would probably break the CMFBG and any material that it is bonded to.

5.10 Strain Sensor Summary

A distributed strain sensor has been presented which utilises a chirped Moiré fibre Bragg grating. This CMFBG has a spatial resolution of 164μm and a strain sensitivity of 0.8±0.01pm/με. Such a device is capable of mapping miniature deformations of a surface by monitoring the strain state along the length of the grating. Applying a higher strain to the second overlaid chirped grating can alter the spatial resolution of the CMFBG. The maximum spatial resolution is then physically limited by the strain that can be applied to the second grating. However, practically the limit is governed by the resolution of the measurement device. The Agilent measurement kit used for the spectral measurements had a resolution of 2pm that would allow a maximum spatial resolution in the order of 10μm. This was not implemented, as the scanning time of the tuneable laser source would have increased approximately ten-fold.

5.11 Summary

The CMFBG has been shown to be capable distributed sensor, able to accurately detect small changes in load, temperature and strain applied to it. The spatial resolutions achieved are higher than any work presented before, which opens up new possibilities for such sensors. Yet the resolution has not yet reached its limit, higher resolutions are possible but the time constraint for each measurement is significant. Moiré gratings have largely been ignored by the research world, yet there is still a significant amount of research that may be conducted with them. The advent of high quality and highly chirped phase masks may well see the Moiré gratings become more exploited.

6

High Survivability Sensor Array

6.1 Background

As the use of FBGs as communications and sensing devices has increased, so has the need for more sophisticated methods of transporting the information from these elements. The invention of wavelength and time division multiplexing created a boom in the number of optical elements that could be supported within an optical network. The rapid growth of the communications industry saw huge investments in developing networks to allow more efficient ways to communicate via optic fibre but very little work has been conducted towards improving sensing networks. Sensing arrays generally employ a linear array technique where all of the sensing elements are placed in series along a single piece of fibre [78]. Such a system allows for simplistic deployment in the field and cheap material costs. For an average application, where severe damage is not expected, a linear array is the preferred method. However, in situations where damage is expected to occur, such a technique can fail dramatically. An example

of this could be the hull of a battle ship or the wing of an aircraft. For example, a fibre optic sensor array embedded into the hull of a battle ship or the wing of an aircraft [79] [80] could be destroyed by a relatively small calibre shell piercing the side of the vehicle. Little academic work has been conducted into increasing the survivability of an array, with the notable exception of the work by Peng *et al* [81]. Their approach is to separate the sensing array into a number of smaller arrays, interspersed with optical switches and parallel lines of fibre. When a sub-array is damaged, the technique is to measure the array from both ends by allowing the optical switches to bypass the array, rerouting along the parallel fibre, and then measuring the array from the opposite direction. This then allows the array to be fully recovered as long as only one damage point occurs. However, Peng's approach would be extremely costly to implement as a real-life application due to the cost of having seven optical switches for 40 sensing elements. Therefore a cheaper method needs to be considered.

The work presented in this chapter introduces a relatively low cost array designed to have a low susceptibility to failure when damage is induced. The design is unique in that it does not introduce any level of redundancy in order to increase survivability, so avoiding costly duplication. Three different styles of arrays are compared by looking at their susceptibility to damage and any optical penalties that may occur due to their particular configurations.

6.2 Fabrication Of Array Sensors

Four 20mm long Gaussian apodised FBGs were written into individual pieces of hydrogen loaded SMF-28. Each grating was written using a direct write style fabrication system [82] in conjunction with a 244nm SABRE FReD CW laser. They were then annealed for 48 hours at 90°C to out-diffuse the hydrogen. The resultant FBGs were measured to have around 10dB transmission loss and a spectral spacing of ~2nm between adjacent gratings, as shown in Figure 6-1. The

FBGs at 1547nm, 1549nm, 1551nm and 1553nm shall be referred to as λ_1, λ_2, λ_3 and λ_4 from hereon in.

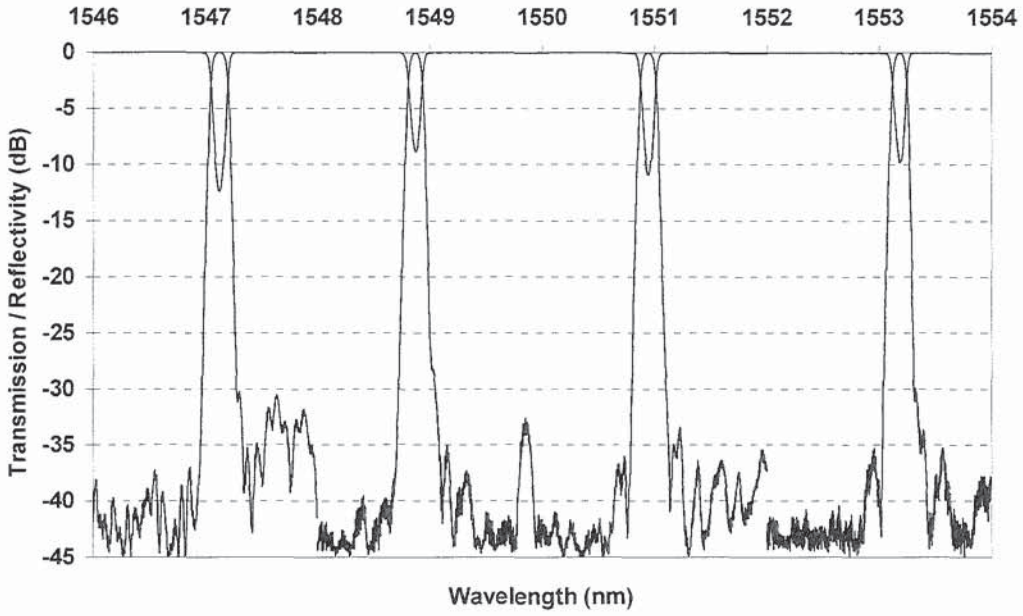

Figure 6-1: Four FBGs used in the sensor arrays, measured in both transmission and reflection.

Due to the relatively low coupling strength of the gratings and the apodisation profile, the side-lobes are suppressed below -30dB. This side lobe suppression was a requirement to reduce the amount of cross-talk between the FBGs.

6.3 Linear Array

A wavelength division multiplexing (WDM) linear array was set up by splicing the gratings together in series and connecting them to a broad band light source and an optical spectrum analyser (OSA) via a circulator, as shown in Figure 6-2. Circulators are typically used as they provide a lower insertion loss than a coupler. The array was set up to replicate the way in which most simple sensor arrays are deployed. To simulate a break in the array a tight bend was induced in the fibre between the gratings at λ_3 and λ_4. Such a bend attenuates any signal propagating along the fibre by out coupling the light to the cladding. This

resulted in the loss of the reflection from the grating at λ_4. The same method was systematically applied to the other positions, between the gratings, along the array. The result was that as the simulated break progressed towards the launch end of the array, the number of grating signals diminished eventually to zero, as shown in Figure 6-3.

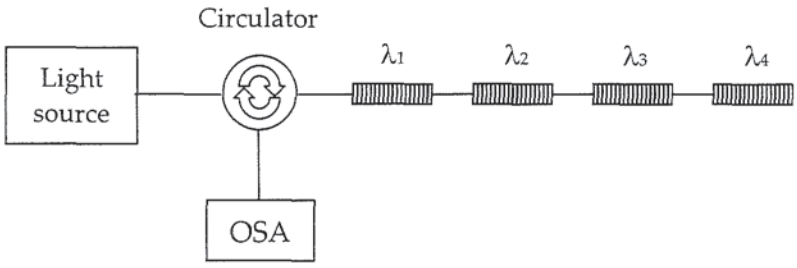

Figure 6-2: Linear array with four FBGs and interrogated with an OSA and a broadband light source.

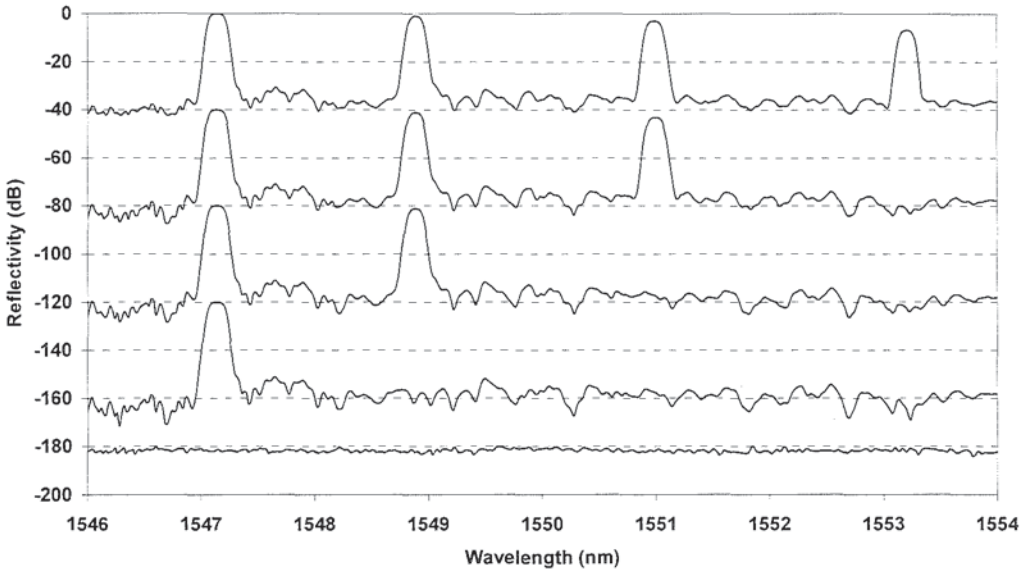

Figure 6-3: Reflection spectra of the linear array as the break is systematically applied along the array.

The implication of this to real life is that if a sensor array has been embedded into a structure then one fracture at the beginning of the array could make the array void. Presently, the technique to combat this is to have the option of measuring

the array from both ends, thus allowing full recovery of data only if there is no more than one break along the array. Two or more breaks would force a loss of data. However, such a technique would require an optical switch to allow fully automated recovery after a break, proving costly, or an access point to allow a manual switch over of where the light is launched and the reflection spectra measured, proving slow and inflexible.

6.4 Multiple Arm Array

Rather than using a single array arm, multiple arms have been previously used where each sensor is located on an arm by itself [83]. This may take the form of a star coupler or an optical switch, as shown in Figure 6-4.

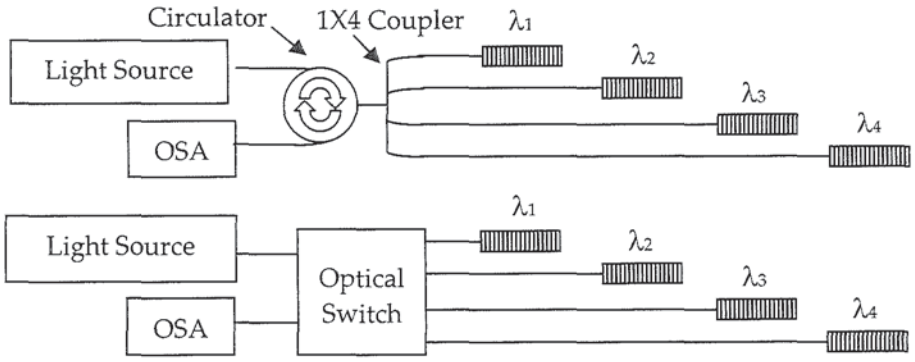

Figure 6-4: Two multiple arm arrays; using a star coupler (top) and an optical switch (bottom).

To show the response of a multiple arm array, a 1x4 coupler was used with a grating spliced onto the end of each of the coupler's arms. Each arm had a break systematically simulated, causing the loss of a single grating, shown in Figure 6-5. The grating lost depended on the position of the break.

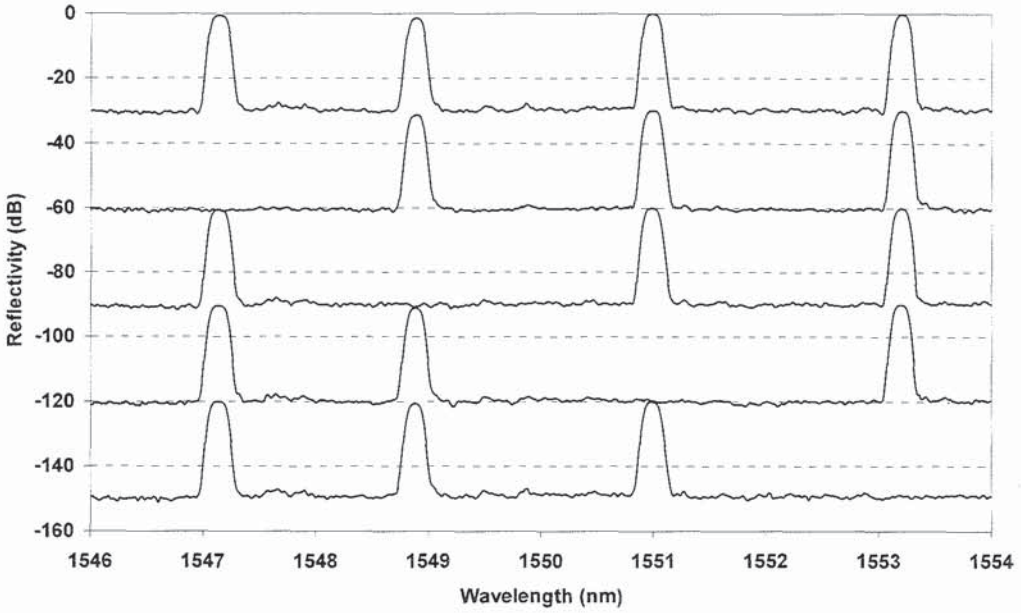

Figure 6-5: Reflection spectrum for the multiple arm array utilising a 1x4 coupler. A single FBG signal disappears as an arm is broken. The top spectra shows the perfect unbroken response with all spectra below displaying one break.

The multiple arm technique has a number of advantages and disadvantages. It is simple and relatively cheap to set up, far cheaper than the alternative approach of using an optical switch. Also a single break will only cause the loss of one grating with no effect to the neighbouring gratings. The disadvantage is that more fibre would be required to form a sensor array, thus not just increasing the chance of a breakage but also decreasing the signal to noise ratio as a low portion of power launched in each fibre. The deployment is also made more complicated since the fibres should not be run in close proximity to one-another since there would be a chance of a single structural failure breaking all of the fibres.

6.5 High Survivability Array

In order to overcome the problem of having too much fibre prone to damage, a new method is proposed. The new methodology employs a series of 50/50 couplers, as shown in Figure 6-6. Placing the couplers between grating pairs not

only reduces the length of fibre needed, in comparison with the multiple arm array, but it also has a surprise advantage.

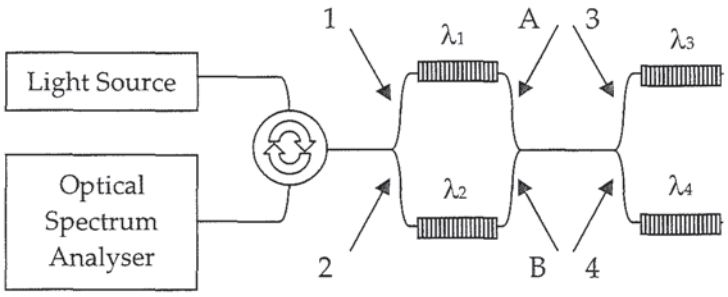

Figure 6-6: Coupler chain design proposed to reduce the susceptibility to damage.

6.5.1 Reflection Regime

If a break occurs at positions 1, 2, 3 or 4 then only one grating reflection signal is lost in an identical manner to the multiple arm technique. However, if a break appears at positions A or B then all reflected signals are still retrieved, shown in Figure 6-7.

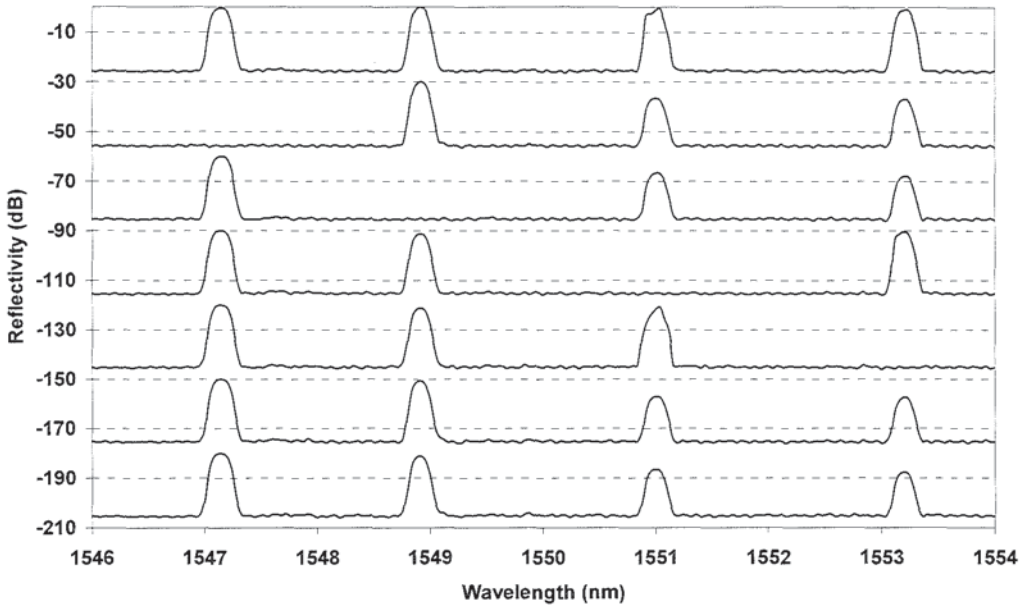

Figure 6-7: Reflection spectrum for the coupler array showing the loss of a signal when breaks occurred at positions 1, 2, 3 and 4 but showing no loss when a breakage occurred in positions A and B. (Top trace is with no break then second from top to bottom breaks at positions 1, 2, 3, 4, A and finally B).

The signals are retained after a break at A or B because the incident light on the final gratings is supplied by both arms of the coupler. Consequently, if one of the coupler's input arms is severed then half of the light is still transmitted to the gratings via the other arm. The resulting power after a break at either A or B is 25% of the strength of the original signal. This is because the 50% power split at the coupler works as a double pass method, 50% of the launched light incident on the FBGs is lost as well as 50% of the reflected signal. In the logarithmic decibel regime this should equate to a 6dB loss of the reflected signal. This prediction is then shown to be experimentally correct as a 6.5dB loss was seen in the gratings beyond the break, as shown in Figure 6-8. The extra 0.5dB loss is probably due to experimental errors such as splicing, fibre handling and coupler efficiency. Although the 6.5dB loss is relatively large, it is still a huge improvement on losing all of the signals beyond the break.

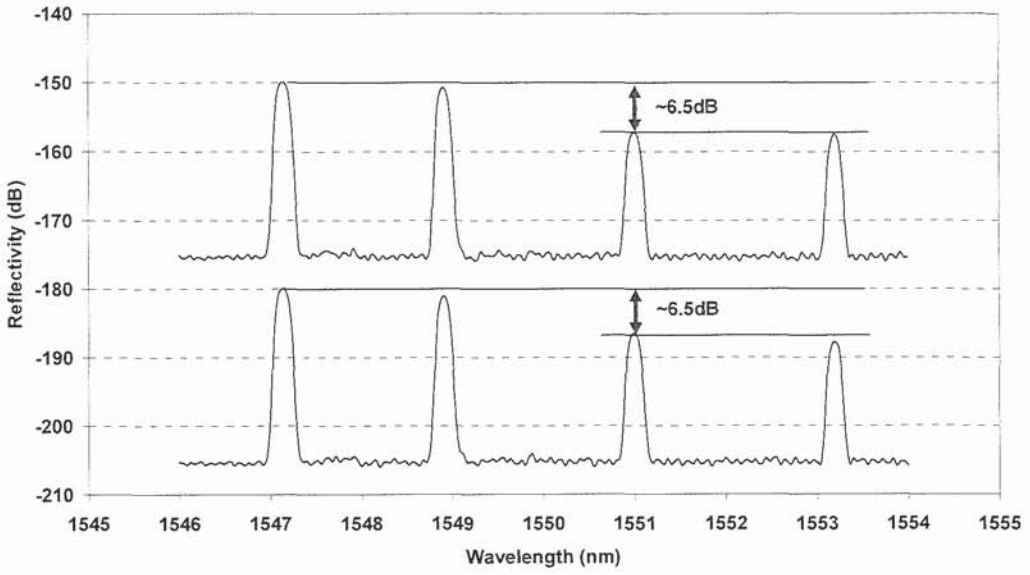

Figure 6-8: Close up of the reflection spectrums for the coupler array when breaks occurred at positions A and B. A 6.5dB loss was observed in the signal strength from the gratings beyond the break.

Although this approach would be the most costly of the described arrays, due to the need for multiple couplers, the advantage of having a lower chance of failure

outweighs the cost disadvantage. In comparison with the technique presented by Peng *et al* the coupler chain array is a fraction of the cost. The main reason for this is that the coupler chain is a completely passive device where the routing of the signal is not influenced by any externally controllable factor, unlike Peng's technique that requires seven optical switches for a similar structure.

6.5.2 Transmission Regime

The transmission spectrum shows an oddity which requires explanation. For this experiment, a different set of gratings were used due to the fibre lengths of the previous set becoming too short to splice. Although the results presented would respond in an identical fashion at any wavelength or strength of grating. Repeating the same coupler chain experiment but looking at the FBGs in transmission shows a similar pattern of one grating being lost in positions 1 to 4 but note that when one grating disappears, the partner grating on the same coupler increases in strength as shown by Figure 6-9 and Figure 6-10. A break in positions A or B creates an identical effect as a break at positions 1 or 2.

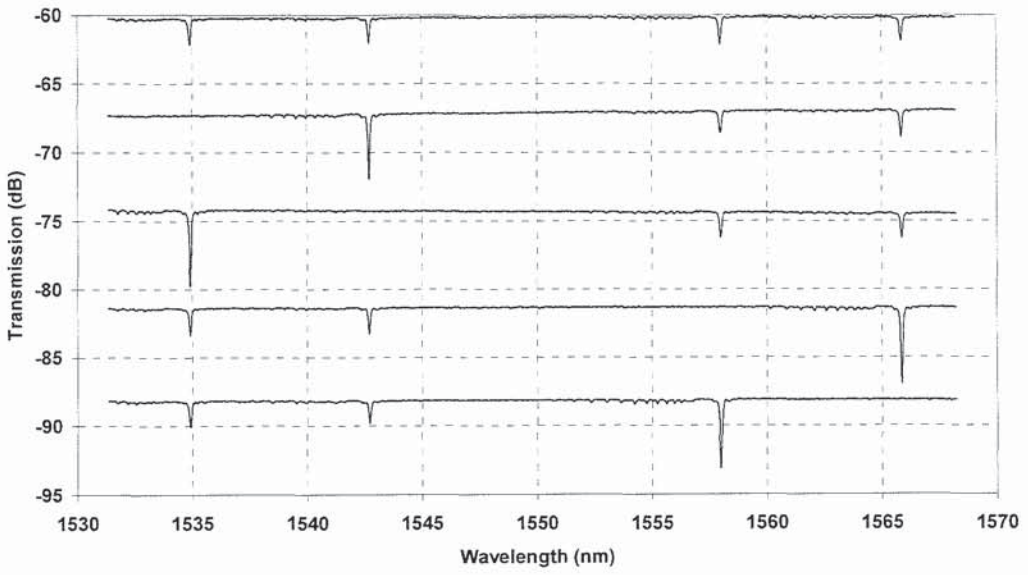

Figure 6-9: Transmission spectrum for the coupler chain when breaks occur at positions 1, 2, 3 and 4 (top trace with no break and the subsequent traces with breaks at positions 1, 2, 3, 4 from top to bottom).

The reasoning for this is that when there is no break, the power from all wavelengths is split equally over the two arms. The FBGs in each arm correspond to two different wavelengths. Consequently, in each arm the wavelength corresponding to that particular FBG will be blocked but in the other arm of the coupler it will be transmitted. Therefore, the gratings appear weaker than they should be since a portion of the FBG wavelength is being transmitted through the opposing arm. When one of the arms is broken the grating appears to grow as its natural strength is observed.

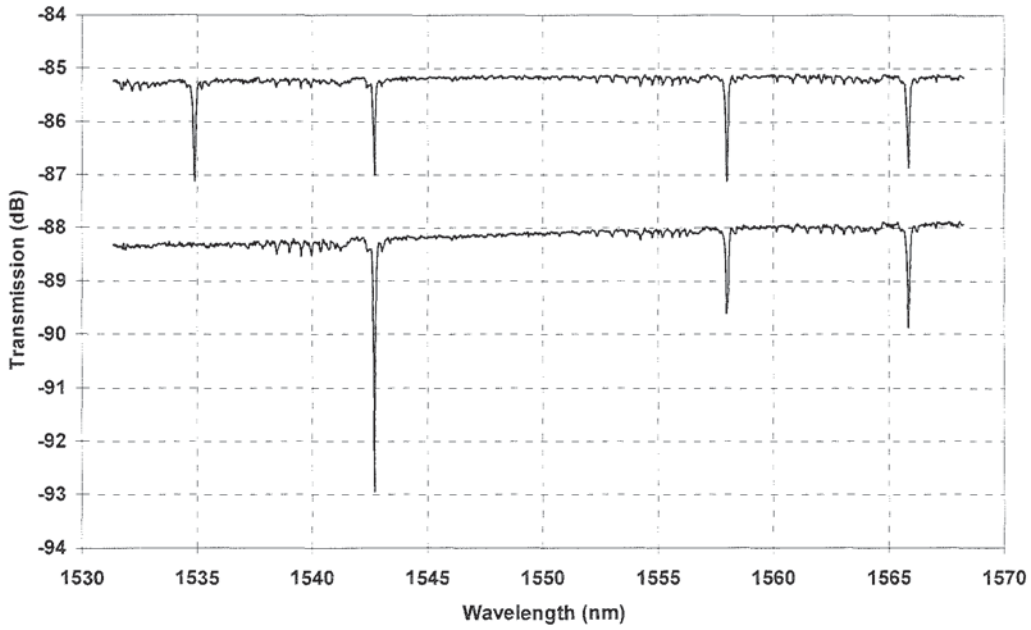

Figure 6-10: Close up of a break at position 1.

These variations in grating strengths can cause problems for measurement systems, possibly causing incorrect wavelength readings. Therefore the coupler chain technique would not be acceptable to be used in a transmission regime.

6.5.3 Interference Issues

For any coupler array with at least two couplers, it would be expected that interference of a reflection signal from an FBG would occur. This expectation derives from the fact that at one coupler the signal is split evenly over the arms and then recombined at some later point by a second coupler. This should therefore create interference as the arms act like a fibre optic Michelson

interferometer, creating a slight mismatch in phases when recombining the two signals. However, no interference is observed in the reflection measurements. The reason for this is that the coherence length of the signals is relatively small. If the arms of the coupler are not equal within one coherence length then no interference is observed. The coherence length of a signal may be calculated using [84]

$$\Delta l_c = \frac{c}{\Delta f} = \frac{\lambda^2}{\Delta \lambda} \tag{6-1}$$

Where c is the speed of light in a vacuum, Δf is the frequency bandwidth of the signal. Since the gratings were written with a spectral bandwidth of about 0.14nm this relates to a coherence length of around 1.7cm. The lack of any interference therefore implies that the parallel arms of the sensor array were mismatched by a length greater than 1.7cm. This therefore needs to be considered if the coupler chain was implemented in an application. Simply ensuring that the path lengths between the couplers are mismatched by more than 1.7cm would suffice.

6.6 Comparison Of Arrays

As a quick way to compare the different arrays, a real-life situation may be simulated. In this case the situation is a sensor array set up to monitor the strain on the leading and trailing edge of an aircraft wing, as shown in Figure 6-11. Such arrays can be used as highly effective health monitors.

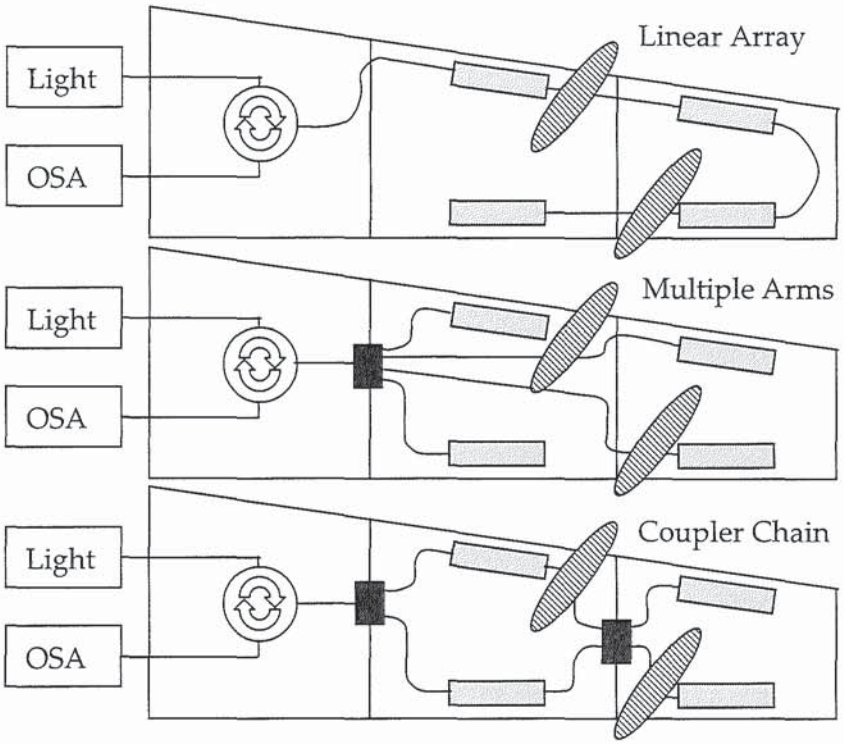

Figure 6-11: Schematic showing how the linear array, multiple arm array and the coupler chain array could be implemented within an aircraft wing which has obtained some damage. The striped ovals indicate areas where damage is applied, the grey rectangles are FBGs and the black enclosure are couplers.

Selection rules were applied for the positioning of the fibres and couplers. The fibres should be laid towards the centre of the wing as there is less chance of damage but the fibres need maximum separation in case there is a structural failure. The couplers are placed along the aircraft wing's struts, regions of high strength and low chance of damage or deformation. In this situation the linear array would return one signal, the multiple arm array two signals and the coupler chain array three signals.

The design and positioning of the array can greatly alter the chances of recovering the signals after damage occurs. The coupler chain array demonstrates that it is less susceptible to signal failure when damage occurs than the other methods presented.

6.7 Coupler Comparison

Depending on the size of the array, there are a variety of coupler combinations that may be used. For instance, in an 8 sensor system one 1x2 and three 2x2 couplers could be used or just a single 1x8. As each different style of coupler has a different loss characteristic, it is worth calculating the total losses for a sensor system with all possible combinations of couplers in order to find the most loss efficient array. Then from this it is possible to calculate how much power would be returned from a particular signal grating. To constrain the calculations, it is assumed that any system would be made from a series of similar couplers, for example one 1x2 and three 2x2, rather than mixing dissimilar couplers, for instance one 1x4 and two 2x2. Shown in Table 6-1 are the loss characteristics of the coupler range provided by Metrotek.

	Coupler Type							
	1x2	*2x2*	*1x3*	*3x3*	*1x4*	*4x4*	*1x8* *8x8*	*1x16* *16x16*
IL (dB) in each arm	3.40	3.40	5.80	6.20	7.00	8.00	10.20	13.60
IL (%) in each arm	54.29	54.29	73.70	76.01	80.05	84.15	90.45	95.63
Fractional signal throughput in an arm (S)	0.45	0.45	0.26	0.23	0.19	0.15	0.09	0.04
Fractional power loss from coupler	0.08	0.08	0.21	0.28	0.20	0.366	0.23	0.30
Total fractional signal throughput of coupler (T)	0.91	0.91	0.78	0.72	0.79	0.634	0.76	0.69

Table 6-1: Metrotek's range of couplers showing the insertion loss (IL) values both in dB and as a percentage. The IL figures are the loss for each output arm of a signal passing from the input port to any one of the output ports.

The insertion loss values are the losses that would be measured by inputting a signal at the input arm of the coupler and then measuring the throughput on one of the output arms. The fractional power loss from the coupler is the loss induced due to inefficient coupling from the input arm to the output arms. The fractional power remaining after the coupler is then just the input signal minus the loss. By summating the losses of a system, the fraction of signal returned from the final sensor in an FBG may be calculated. For a coupler chain array, this may be calculated using the following equation:

$$\text{Reflection Signal} = RS_{1\times n}T_{1\times n}T_{splice}^{4} \qquad N\leq n \tag{6-2}$$

$$\text{Reflection Signal} = RS_{n\times n}T_{1\times n}^{2}T_{n\times n}^{\frac{2N}{n}-3}T_{splice}^{\frac{4N}{n}} \qquad N>n \tag{6-3}$$

Where n is the level of multiplexing in an nxn coupler, S the fractional signal throughput in a single arm of the coupler, T_{1xn} the total signal throughput of a 1xn coupler, T_{splice} the fractional transmission of a signal across a splice, T_{nxn} the total signal throughput of an nxn coupler, R the fractional reflectivity of the FBG sensor and N the total number of sensors in the system. The 'T' values need to be considered as the signal power passing through a coupler is split evenly over the output arms. The calculations are for the final FBGs as they are the ones which will experience the greatest level of loss. These equations were formed by considering how the route of a single signal is affected as it passes along the array. In the situation where N≤n, see Figure 6-12, (where there is only one 1xn coupler and two splices), the input light has to pass across the 1xn coupler and is split equally amongst all of the arms. This means that the signal reaching any one of the FBGs at the end of a single coupler arm is dramatically reduced due to the splitting of the signal, so the first step is to include the term S_{1xn}. The signal is then reflected by the FBG thus needing the term R. Upon reflection the signal is sent back through the coupler and into the original input arm with no splitting occurring, the loss experienced is just the intrinsic loss of the coupler itself so

giving the need for the T_{1xn} term. A term to account for the number of splices is also included; this considers the fact that the coupler is spliced to a light source and to an FBG on each output arm, so for every coupler in an array there are two splices. A reflected signal from an FBG would then have experienced passing through four spliced regions per coupler, hence the factor of four in the splice terms.

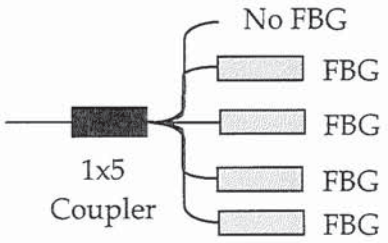

Figure 6-12: Coupler array where N<n.

For the situation where N>n, see Figure 6-13, a similar process was used to form the equation. One point to note is that by adding more than one coupler allows almost all of the optical power, which was split equally over each arm in the first coupler, to be recombined. This implies that the total power loss in a two coupler system is only slightly more than a one coupler system.

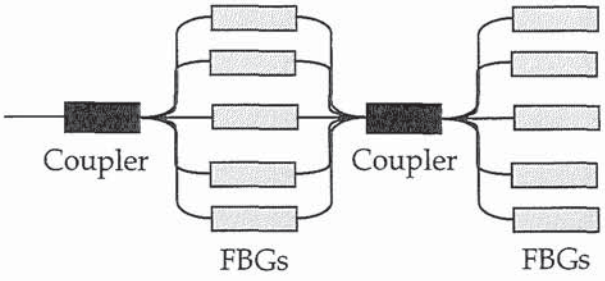

Figure 6-13: Coupler array where N>n.

Unlike a linear array, the losses within a coupler chain array need to be carefully considered due to the induced losses from the couplers. Using the above equations (6-2), (6-3) and Table 6-1 the final signal returned from a variety

coupler chain arrays, 2x2, 3x3, 4x4, 8x8 and 16x16 has been calculated, as shown in Figure 6-14.

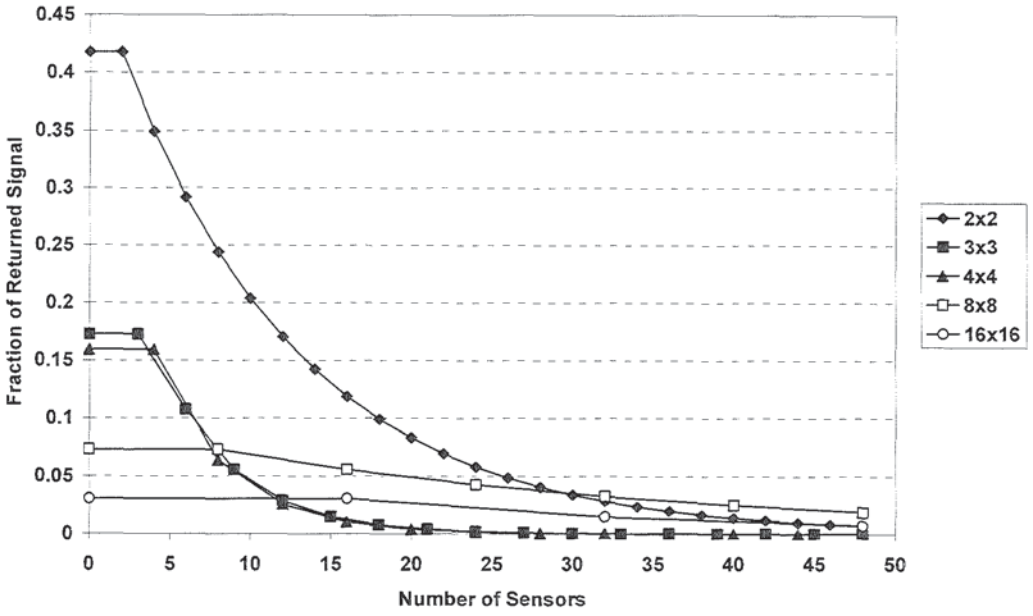

Figure 6-14: Fractional signal power returned from the final sensor in a variety of coupler chains.

In an industrial system the maximum acceptable splice loss is a value of 0.03dB which relates to a fractional transmission of a signal across the splice of 0.9931. This value was used in the calculations for Figure 6-14. By comparing the different types of couplers in this way, the most loss efficient coupler chain may be found. For less than 30 sensors in a coupler chain, a 2x2 styled chain gives the highest fraction of signal return. Above 30 sensors, the 8x8 couplers become more efficient. Part of the reason for this is the splice loss; for a 30 sensor system, a reflected signal from the final FBG would see 60 splices using 2x2 couplers but only 16 splices in a 16x16 coupler system. Also the manufacturing process used to fabricate the 8x8 and 16x16 couplers is different from the other couplers. Low multiplexed level couplers are often created using a twisted pair of fibres that are then fused together, relying on the signal's electric field crossing from one fibre to the other [85]. The higher multiplexed level couplers tend to fuse the input fibres to a silica rod where at the other end of the rod there is an equal amount of

output arms. This technique proves more efficient when combining large numbers of fibres since the twisted fibre method breaks down as the number of combining fibres increases. It becomes increasingly more difficult to twist the fibres together so that they have equal coupling from one arm to any other.

An interesting point to note is that the 3x3 and 4x4 coupler chains have identical curve shapes. The reason for this is that the same technology is used to create a 3x3 coupler as is used for a 4x4 coupler. The only difference is that two of the arms (one from each side) are cut off the 3x3 coupler.

If a coupler chain was implemented as the network architecture for a sensor array then the results show that the most loss effective method would be to use 2x2 couplers for a system with 30 sensors or less or to use 8x8 couplers if there were more than 30 sensors. However, practically a fractional return of at least 0.1 of the original signal would be required to allow enough light back into the measurement system (exact value depending on the light source and sensitivity of the detectors). This would therefore limit the system to 18 sensors and so allowing the 2x2 coupler chain variant to be the most loss efficient.

6.8 Summary

The three arrays presented all have their particular advantages and disadvantages. The linear array provides a cheap and simple approach but is plagued by its own fragility. The multiple arm array is slightly more expensive than the linear array but provides a lower chance of failure but the extra lengths of fibre can prove difficult to manage when installing the array. The newly proposed coupler chain array presents the lowest chance of losing a signal when a break occurs but it is also the most expensive due to the need for multiple couplers. The coupler chain array design would be highly applicable to large military vehicles, such as battle ships, where cost is of a lower priority than in general commercial activities.

7

Thesis Conclusion

The contents of this thesis have demonstrated the physical requirements to allow high quality fibre Bragg gratings to be manufactured. The different aspects adversely affecting the quality of the gratings have been investigated systematically and their effects eliminated. The negative aspects discovered ranged from air currents around the fibre to vibrations on the optical table caused by cooling water pumped into the laser. A variety of techniques were implemented to eliminate these destructive elements including the utilisation of enclosure to reduce air currents and rubber feet to damp any vibrations. Subsequently higher quality gratings, tailored towards telecoms integration, were able to be fabricated.

A unique fibre sensor has been demonstrated in the form of a chirped fibre Bragg grating wear sensor. This is the first time that fibre optics have been used to directly measure the amount of wear or erosion an object undergoes. Such a system benefits from an extremely high resolution, exceeding most other techniques currently available. By operating the wear sensor in an alternative

fashion, it has been shown that it is capable of accurately detecting the position and size of damage inflicted on an object. The sensor can be operated in a relatively simple and cheap form by using an amplitude detection system, giving the technique extra commercial impetus. The work was subsequently patented by Insensys Ltd.

The use of chirped Moiré fibre Bragg gratings has been investigated further. The spatial resolution of using such gratings as distributed strain and temperature sensors has been drastically improved. A two-dimensional temperature sensor has been demonstrated to give a thermal profile of any suitably sized object. For the first time the use of load induced birefringence has been demonstrated as a distributed load sensor.

As a consequence of thinking about sensors, a novel sensor array has been invented and studied. A high survivability sensor network array has been shown to be capable of absorbing damage yet maintaining operational capability. Such a system operates in a passive manner, by-passing the need for expensive electronic detecting and rerouting equipment. This network is directly relevant to the damage detection sensor which may be operated within harsh environments where damage is expected to occur. Different manifestations of the array have been shown to have different optical loss efficiencies. A general equation has been formed to give the loss efficiency, allowing simple optimisation of the network.

7.1 Future Work

The shut-down of Indigo Photonics saw the transfer of the direct write system to Aston University. Such a system can only be equalled, in quality, by a small handful of commercial systems worldwide. This leaves the photonics research group in a hugely privileged position with the ability to fabricate almost any grating profile imaginable. Work started, in collaboration with Dr E. Turitsyna

began to exploit the ability of the direct write system to fabricate complex profile gratings. The possibility of creating cutting-edge gratings has been made available but requires the theoretical backing to produce the complex profiles. Improvements can be made to the system; a telescope can be installed to expand the beam, clean it and then reduce the spot size and a velocity compensation scheme can be introduced to write stronger sections towards the edge of a grating where the chirp roll off occurs. The system can also act as a test bed for increasing the understanding of system isolation, something that is not only relevant to FBG fabrication but also computer chip lithography and other highly sensitive production techniques.

The use of highly chirped Moiré sensors highlighted a current difficulty of extending the range of optical sensing. The scan time required to measure the gratings was long, due to the large spectral bandwidth. There is an obvious opening for novel methods of sensor detection and demodulation, something which G. Lloyd has successfully studied and commercialised during his time at Aston University as a PhD student and an Indigo Photonics and Insensys employee. With the development of better detection systems, Moiré sensors can be measured more rapidly or arrays such as the high survivability sensor array can be taken to higher multiplexing levels, allowing more points to be sensed simultaneously.

8

Publications

1. E. Turitsyna, R. Bhamber, V.K. Mezentsev, **A. Gillooly**, J. Mitchell, S.K. Turitsyn, "Design of FBG-based ultra-narrow asymmetric filter for transmission with 0.8 bit/s/Hz spectral efficiency without polarization multiplexing," *Optical Fiber Technology*, **11**(2), 202-208, 2005.

2. **A.M. Gillooly**, "Quasi-Distributed Strain Sensor Incorporating A Chirped Moiré Fiber Bragg Grating," *IEEE Photonics Technology Letters*, **17**(2), 444-446, 2005.

3. **A.M. Gillooly**, L. Zhang and I. Bennion, "Implementation Of A Distributed Temperature Sensor Utilising A Chirped Moiré Fibre Bragg Grating," *Optics Communications*, **242**(4-6), 511-515, 2005.

4. **A.M. Gillooly**, H. Dobb, L. Zhang and I. Bennion, "Distributed Load Sensor By Use Of A Chirped Moiré Fiber Bragg Grating," *Applied Optics*, **43**(35), 6454-6457, 2004.

5. D.J. Webb, T. Allsop, H. Dobb, K. Kalli, T. Earthrowl, V. Mezentsev, **A. Gillooly**, R. Neal and I. Bennion, "Sensing applications of long-period gratings in various fibre types," *Proceedings- SPIE The International Society For Optical Engineering*, **5502**, 2004, pp. 104-107.

6. **A. Gillooly**, L. Zhang, I. Bennion, "High Survivability Fibre Sensor Network For Smart Structures" *Photon04*, Glasgow, UK 6-9 September 2004, pp12-13.

7. **A. Gillooly**, L. Zhang, I. Bennion, "High Survivability Fiber Sensor Network For Smart Structures" *SPIE – Photonics North*, Ottawa, Canada, 26-29 September 2004, pp80.

8. E.G. Turitsyna, **A. Gillooly**, V.K. Mezentsev and S.K. Turitsyn, "FBG-based asymmetrical off-centred VSB filters for transmission with 0.8 bit/s/Hz spectral efficiency" *POWAG*, Bath, UK, 12-16 July 2004.

9. T. Allsop, T. Earthgrowl, H. Dobb, V. Mezentsev, **A. Gillooly**, D.J. Webb, I. Bennion, "The spectral sensitivity of long-period gratings fabricated in elliptical core D-shaped optical fiber," *Proceedings of SPIE The International Society For Optical Engineering*, **5589**, 266-277, 2004.

10. D. J. Webb, T. Allsop, H. Dobb, K. Kalli, T. Eathrowl, V. Mezentsev, **A. Gillooly**, R. Neal and I. Bennion, "Sensing Application of Long-Period Gratings in Various Fibre Types", *Second European Workshop on Optical Fibre Sensors*, Santander, Spain, 9-11 June 2004.

11. T. Allsop, **A. Gillooly**, V. Mezentsev, T. Earthgrowl-Gould, R. Neal, D.J. Webb and I. Bennion, "Bending and Orientational Characteristics of Long Period Gratings Written in D-Shaped Optical Fiber", *IEEE Transactions On Instrumentation And Measurement – Joint Issue With The IEEE/OSA Journal Of Lightwave Technology*, **53**(1), 2004.

12. T. Allsop, **A. Gillooly**, V. K. Mezentsev, T. Earthgrowl-Gould, R. Neal, D. J. Webb and I. Bennion, "The Spectral Characteristics of Long Period Gratings Written in D-Shaped Optical Fiber as Bending Sensors", *Proceedings of the 16th International Conference on Optical Fibre Sensors (OFS 2003)*, IEICE, Japan, pp. 88-91, 2003.

13. **A.M. Gillooly**, K.E. Chisholm, L. Zhang and I. Bennion, "Chirped fibre Bragg Grating Optical Wear Sensor", *Measurement Science and Technology*, **15**, 885-888, 2004.

14. X. Shu, J. Mitchell, **A. Gillooly**, K. Chisholm, K. Sugden and I. Bennion, "Tunable dispersion slope compensator using novel tailored Gires-Tournois etalons," *Conference on Optical Fibre Communications (OFC2004)*, Los Angeles, CA, USA, February 2004.

15. **A.M. Gillooly**, K.E. Chisholm, L. Zhang and I. Bennion, "Implementation Of Chirped Fiber Bragg Gratings (CFBG) As Optical Wear Sensors", *16th Annual Meeting of the IEEE Laser and Electro-Optic Society (LEOS)*, 27th October 2003.

16. **A.M. Gillooly**, K.E. Chisholm, L. Zhang and I. Bennion, "Optical Wear Sensor By Utilisation Of A Chirped fibre Bragg Grating", *Photonex03*, 8th October 2003.

17. X. Shu, K. Chisholm, I. Felmeri, K. Sugden, **A. Gillooly**, L. Zhang, I. Bennion, "Highly sensitive transverse load sensing with reversible sampled fiber Bragg gratings", *Applied Physics Letters*, **83**(15), 2003.

18. X. Shu, K. Chisholm, I. Felmeri, L. Everall, K. Sugden, **A. Gillooly**, L. Zhang, I. Bennion, "Novel optical load sensors based on mechanically induced sampled fiber Bragg gratings", *16th International Conference On Optical Fiber Sensors (OFS)*, 13th October 2003.

19. X. Shu, K. Chishol., J. Mitchell, I. Felmeri, P. Rhead, **A. Gillooly**, K. Byron, K. Sugden, "Tunable dispersion compensator based on three distributed Gires-Tournois etalons", *Bragg Gratings, Photosensitivity and Poling in Glass (BGPP) Topical Meeting*, 3rd September 2003.

20. F. Floreani, **A. Gillooly**, L. Zhang, I. Bennion, X. Shu and K. Sugden, "A simple method for the fabrication of intrinsically apodised chirped fibre Bragg gratings", *Journal of Optics A: Pure and Applied Optics*, **5**(2003) S59-62.

21. F. Floreani, **A. Gillooly**, X. Shu, K. Sugden, L.Zhang and I. Bennion, "Effects of intrinsic Apodisation in Chirped Fibre Bragg Gratings fabricated using Scanning Holographic Set-up", *Photon02*, 2nd September 2002.

22. F Floreani, **A Gillooly**, D Zhao, L Zhang, I Bennion, X Shu and K Sugden, "Investigation of intrinsically apodised chirped fibre Bragg gratings fabricated using scanning holographic set up", *Proceedings of IEEE/LEOS Workshop on Fibre and Optical Passive Components* , Glasgow, UK , pp. 80-85 (jun 2002).

23. F Floreani, **A Gillooly**, L Zhang, I Bennion, X Shu and K Sugden, "Fabrication of chirped gratings of arbitrary wavelength and intrinsic apodisation profile using scanning holographic set-up", *White Nights' Summer School on Photosensitivity in Optical Waveguides and Glasses*, St Petersburg, Russia (jun 2002).

Patents

1. A.M. Gillooly and Insensys, "Wear Sensor", Patent filed 7th October 2003, Patent Application No. GB0323430.9.

Media Articles

1. "Detecting Wear In Heavy Duty Applications Using Optical Sensing", Technical Insights Alert, April 2004.

2. "Fiber gratings give abrasion alert", Optics.org, 24 June 2004. http://optics.org/articles/news/10/6/16/1

3. "Fibre gratings give abrasion alert", Optics and Laser Europe, pp. 11, July/August 2004.

9

References

[1] T. Erdogan, "Fiber Grating Spectra," Journal of Lightwave Technology, **15**(8), 1277-1294, 1997.

[2] A. Yariv, "Coupled-mode theory for guided-wave optics," IEEE Journal of Quantum Electronics, **9**, 919-933, 1973.

[3] P. St J. Russell, J.L. Archambault and L. Reekie, *Physics World*, pp 41, Oct 1993.

[4] B. Poumellec, P. Niay, M. Douay and J.F. Bayon, "The UV induced refractive index grating in Ge:SiO_2 preforms: additional CW experiments and the macroscopic origin of the change in index," Journal of Physics D, Applied Physics, **29**, 1842-1856, 1996.

[5] M. Douay *et Al*, "Microscopic investigations of Bragg gratings photowritten in germanosilicate fibers," Photosensitivity and Quadratic Nonlinearity in Waveguides: Fundamentals and Applications, **22**, 48-51, 1995.

[6] L. Dong, T.A. Birks, M.H. Ober and P.S. Russell, "Intermodal coupling by periodic microbending in dual-core fibers – comparison of experiment and theory," Journal of Lightwave Technology, **12**(1), 1994.

[7] A. Othonos A. and K. Kalli, Fibre Bragg Gratings (Artech House, Massachusetts, 1999).

[8] R. Kashayap, Fiber Bragg Gratings (Academic Press, California, 1999).

[9] D.P. Hand and P. St. J. Russell, "Photoinduced refractive-index changes in germanosilicate fibres," Optics Letters, **15**, 102-104, 1990.

[10] C. Fiori and R.A.B. Devine, "Evidence for a wide continuum of polymorphs in a-SiO_2," Physical Review B, **33**, 2972-2974, 1986.

[11] T.E. Tsai, G.M. Willians and E.J. Friebele, "Index structure of fiber Bragg gratings in Ge-SiO_2 fibers," Optics letters, **22**(4), 224-226, 1997.

[12] Y. Hibino and H. Hanafusa, "ESR study on E'-centers induced by optical fiber drawing process," Japanese Journal of Applied Physics, **22**, L766-L768, 1983.

[13] N.M. Lawandy, "Light induced transport and delocalization in transparent and amorphous systems," Optics Communications, **74**, 180-184, 1989.

[14] H. Honso, Y. Abe, D.L. Kinser, R.A. Weeks, K. Muta and H. Kawazoe, "Nature and origin of the 5 eV band in SiO_2:GeO_2 glasses," Physics Review B, **46**(18), 11445 – 11451, 1995.

[15] P. St. J. Russell, D.P. Hand and Y.T. Chow, "Optically-induced creation, transformation and organisation of defects and colour-centres in optical fibres," International Workshop on Photoinduced Self-Organization Effects in Optical Fiber, Quebec City, Quebec, May 10-11, Proceedings SPIE, **1516**, 47-54, 1991.

[16] C.L. Liou, L.A. Wang, M.C. Shin and T.J. Chuang, "Characteristics of hydrogenated fiber Bragg gratings," Applied Physics A, **64**, 191-197, 1997.

[17] D.L. Williams, B.J. Ainslie, J.R. Armitage, R. Kashyap and R. Campbell, "Enhanced UV photosensitivity in boron codoped germanosilicate optical fibres," Electronics Leters, **29**, 45-47, 1993.

[18] T. Erdogan, V. Mizrahi, P.J. Lemaire and D. Monroe, " Decay of ultraviolet induced fiber Bragg gratings," Journal of Aplied Physics, **76**, 73-80, 1994.

[19] S.R. Baker, H.N. Rourke, V. Baker and D. Goodchild, "Thermal decay of fiber Bragg gratings written in boron and germanium codoped silica fiber," Journal of Lightwave Technology, **15**(8), 1470-1477, 1997.

[20] K.O. Hill, Y. Fujii, D.C. Johnson and B.S. Kawasaki, "Photosensitivity in optical fiber waveguides: Application to reflection filter fabrication," *Applied Physics Letters*, **32**, 647-649, 1978.

[21] D.Z. Anderson, V. Mizrahi, T. Erdogan and A.E. White, "Production of in-fibre gratings using a diffractive optical element," Electronics Letters, **29**(6), 566-568, 1993.

[22] J. Martin and F. Ouellette, "Novel writing technique of long and highly reflective in-fibre gratings," Electronics Letters, **30**(10), 811-812, 1994.

[23] W.H. Loh, M.J. Cole, M.N. Zervas, S. Barcelos and R.I. Laming, "Complex grating structures with uniform phase masks based on the moving fiber-scanning beam technique," *Optics Letters*, **20**(20), 2051-2053, 1995.

[24] Z. Xiong, G.D. Peng, B. Wu and P.L. Chu, "Effects of zeroth-order diffraction of a phase mask on Bragg gratings," *IEEE Journal of Lightwave Technology*, **26**, 2361-2365, 1999.

[25] P. Wickramarachi, "Effects of windowing on the spectral content of a signal," Sound and Vibration, January, 10-11, 2003.

[26] Wolfram Research Science World: http://scienceworld.wolfram.com

[27] M. Yamada and K. Sakuda, "Analysis of almost-periodic distributed feedback slab wave-guides via a fundamental matrix approach," Applied Optics, **26**(16), 3474-3478, 1987.

[28] H.G. Frolich and R. Kashyap, "Two methods of apodisation of fibre Bragg gratings," Optics Communications, **157**, 273-281, 1998.

[29] M.C. Wu and R.S. Rogowski, "Fabrication of self-apodized short-length fiber Bragg gratings," Applied Optics, **42**(25), 5017-5023, 2003.

[30] J. Albert, K.O. Hill, B. Malo, S.T. Theriault, F. Bilodeau, D.C. Hohnson and L.E. Erickson, "Apodisation of the spectral response of fibre Bragg gratings using a phase mask with variable diffraction efficiency," Electronics Letters, **31**, 222-223, 1995.

[31] A.M Vengsarkar, W.A. Reed, "Dispersion-compensating single-mode fibers – efficient designs for 1st –order and 2nd-order compensation," Optics Letters, 18(11), 924-926, 1993.

[32] M. Onishi, Y. Koyano, M. Shigematsu, H. Kanamori, M. Nishimura, "Dispersion compensating fibre with a high figure of merit of 250ps/nm/dB," Electronics Letters, 30(2), 116-163, 1994.

[33] L.S. Tamil, Y.S. Li, J.M. Dugan, K.A. Prabhu, " Dispersion compensation for high bit-rate fiber optic communication using a dynamically tunable optical filter," Applied Optics, 33(9), 1697-1706, 1994.

[34] X. Shu, K. Chishol., J. Mitchell, I. Felmeri, P. Rhead, A. Gillooly, K. Byron, K. Sugden, "Tunable dispersion compensator based on three distributed Gires-Tournois etalons", *Bragg Gratings, Photosensitivity and Poling in Glass (BGPP) Topical Meeting*, 3rd September 2003.

[35] X. Shu, J. Mitchell, A. Gillooly, K. Chisholm, K. Sugden and I. Bennion, "Tunable dispersion slope compensator using novel tailored Gires-Tournois etalons," *Conference on Optical Fibre Communications (OFC2004)*, Los Angeles, CA, USA, February 2004.

[36] K. Ennser, M.N. Zervas and R.I. Laming, "Optimization of apodised linearly chirped fiber gratings for optical communications," IEEE Journal of Quantum Electronics, **34**, 770-778, 1998.

[37] R. Feced and M.N. Zervas, "Effects of random phase and amplitude errors in optical fiber Bragg gratings," Journal of Lightwave Technology, **18**(1), 90-101, 2000.

[38] K.O. Hill, B. Malo, F. Bilodeau, D.C. Johnson, J. Albert, "Bragg gratings fabricated in monomode photosensitive optical fiber by UV exposure through a phase mask," Applied Physics Letters, 1035-1037, 1993.

[39] A. Asseh, H. Storoy, B.E. Sahlgren, S. Sandgren, R.A.H. Stubbe, "A writing technique for long fiber Bragg gratings with complex reflectivity profiles," 15(8), 1419-1423, 1997.

[40] T. Allsop, K. Chisholm, I. Bennion, A. Malvern, R. Neal, "A strain sensing system using a novel optical fibre Bragg grating sensor and a synthetic heterodyne interrogatin technique," Measurement Science & Technology, **13**(5), 731-740, 2002.

[41] L.A. Everall, K. Sugden, J.A.R. Williams, I. Bennion, X. Liu, J.S. Aitchison, S. Thoms, K.M. DelaRue, "Fabrication of multipassband moiré resonators in fibers by the dual-phase-mask exposure method," Optics Letters, 22(19), 1473-1475, 1997.

[42] M. Ibsen, M.K. Durkin, M.J. Cole and R.I. Laming, "Optimised square passband fibre Bragg grating filter with in-band flat group delay response," Electronics Letters, **34**(8), 1998.

[43] R. Feced, M.N. Zervas and M.A. Muriel, "An efficient inverse scattering algorithm for the design of nonuniform fiber Bragg grating," IEEE Journal of Quantum Electronics, **35**(8), 1105-1115, 1999.

[44] J. Skaar, L. Wang and T. Erdogan , "On the synthesis of fiber Bragg grating by Layer Peeling," IEEE Journal of Quantum Electronics, **37**, 165-173, 2001.

[45] E.G. Turitsyna, A. Gillooly, V.K. Mezentsev and S.K. Turitsyn, "FBG-based asymmetrical off-centred VSB filters for transmission with 0.8 bit/s/Hz spectral efficiency" *POWAG*, Bath, UK, 12-16 July 2004.

[46] S. Kieckbusch, C. Knothe and E. Brinkmeyer, "Fast and accurate characterization of fiber Bragg gratings with high spatial resolution and spectral resolution," in Optical Fiber Communication (OFC), OSA Technical Digest Series (Optical Society of America, Washington, DC, 2003), paper WK2.

[47] K.G. Kreider and A.W. Ruff, "Materials for thin-film wear sensors," Surface and Coatings Technology, 86-87(1-3), 557-563, 1996.

[48] A.W. Ruff and K.G. Kreider, "Deposited thin-film wear sensors: materials and design," Wear, 203, 187-195, 1997.

[49] M. Sortino, "Application of statistical filtering for optical detection of tool wear," International Journal of Machine Tools & Manufacture, 43(5), 493-497, 2003.

[50] S.J. Yaxley and J.A.G. Knight, "The development and integration of novel sacrificial wear sensors into the quarrying industry," Sensors and Actuators A - Physical, 75(1), 24-34, 1999.

[51] A. Othonos, "Fiber Bragg Gratings," Review of Scientific Instruments, 68(12), 4309-4341, 1997.

[52] X.C. Li, F. Prinz and J. Seim, "Thermal behavior of a metal embedded fiber Bragg grating sensor," Smart Materials and Structures, 10(4), 575-579, 2001.

[53] L.A. Everall, K. Sugden, J.A.R. Williams and I. Bennion, "Fabrication of multipassband Moiré resonators in fibres by the dual-phase-mask exposure method," Optics Letters **22**, 1473-1475 (1997).

[54] L. Zhang, K. Sugden, I. Bennion and A. Molony, "Wide-stopband chirped fibre moiré grating transmission filters," Electronics Letters **31**, 477-479 (1995).

[55] P. Torres and L.G.C. Valente "Spectral response of locally pressed fiber Bragg grating," Optics Communications **208**, 285-291 (2002).

[56] M. LeBlanc, S.T. Vohra, T.E. Tsai and E.J. Friebele, "Transverse load sensing by use of pi-phase-shifted fiber Bragg gratings," Optics Letters **24**, 1091-1093 (1999).

[57] S.C. Tjin, L. Mohanty and N.Q. Ngo, "Pressure sensing with embedded chirped fiber grating," Optics Communications **216**, 115-118 (2003).

[58] X.W. Shu, K. Chisholm, I. Felmeri, K. Sugden, A. Gillooly, L. Zhang and I. Bennion, "Highly sensitive transverse load sensing with reversible sampled fiber Bragg gratings," Applied Physics Letters **83**, 3003-3005 (2003).

[59] Y. Liu, L. Zhang and I. Bennion, " Fibre optic load sensors with high transverse strain sensitivity based on long-period gratings in B/Ge co-doped fibre," Electronics Letters **35**, 661-663 (1999).

[60] L. Zhang " Design and realisation of long-period grating devices in conventional and high birefringence fibers and their novel applications as fibre optic load sensors," IEEE J. Sel. Top. Quantum Electronics **5**, 1371-8 (1999).

[61] S. Doucet, R. Slavik and S. LaRochelle, "High-finesse large band Fabry-Perot fibre filter with superimposed chirped Bragg gratings," Electronics Letters, 38(9), 2002.

[62] R. Gafsi and M.A. El-Sherif, "Analysis of Induced-Birefringence Effects on Fiber Bragg Gratings," Optical Fiber Technology, **6**, 299-323 (2000).

[63] A. Zhang, B. Guan, X. Tao and H. Tam, "Experimental and theoretical analysis of fiber Bragg gratings under lateral compression," Optics Communications, 206, 81-87 2002.

[64] M. Volanthen, H. Geiger and J.P. Dakin, "Distributed grating sensors using low-coherence reflectometry," Journal of Lightwave Technology, 15(11), 2076-2082, 1997.

[65] A.D. Kersey and T.A. Berkoff, "Fiber optic Bragg-grating differential-temperature sensor," IEEE Photonics Technology Letters, 4(10), 1183-1185, 1992.

[66] V. Bhatia "Applications of long-period gratings to single and multi-parameter sensing," Optics Express, 4(11), 457-466 1999.

[67] K.E. Chisholm, K. Sugden, I.J. Murgatroyd, B. Sundström, B. Lindström and L. Zhang, "Application of Chirped Moiré Fibre Bragg Gratings to Quasi-distributed Monitoring of Strains Experienced by Fibres During Processing," OFS 2000 Venice, Italy, 11-13 Oct. 2000.

[68] K.E. Chisholm, K. Sugden, L.Zhang and I. Bennion, "Novel high spatial resolution and temperature sensor using chirped Moiré fibre gratings," in OSA Technical Digest Of Bragg Gratings, Photosensitivity and Poling and Glass Waveguides Florida 1999, pp.183-185.

[69] A. Othonos A. and K. Kalli, Fibre Bragg Gratings (Artech House, Massachusetts, 1999).

[70] W.W. Morey, J.R. Dunphy and G. Meltz, "Multiplexing fibre Bragg grating sensors," Proc SPIE Int. Soc. Opt. Eng, 1991, 1586, 216-224.

[71] G. Meltz and W.W. Morey, "Bragg grating formation and germanosilicate fibre photosensitivity," International Workshop on Photoinduced Self-Organization Effects in Optical Fibre, Quebec City, Quebec, May 10-11, Proceedings SPIE, Vol. 1516, 1991 185-199.

[72] Y.J. Rao, D.J. Webb, D.A. Jackson, L. Zhang and I. Bennion, Optical in-fibre Bragg grating sensor systems for medical applications, Journal of Biomedical Optics, 3(1), 38-44, 1998.

[73] D.J. Webb, M.W. Hathaway, D.A. Jackson, S. Jones, L. Zhang and I. Bennion, First in-vivo trials of a fibre Bragg grating based temperature profiling system, Journal of Biomedical Optics, 5(1), 45-50, 2000.

[74] G.P. Brady, K. Kalli, D.J. Webb, D.A. Jackson, L. Rekie, J.L. Archambault "Simultaneous measurement of strain and temperature using the first and

second-order diffraction wavelengths of Bragg gratings," IEE Proc. – Optoelectron, **144**(3), 156-161, 1997.

[75] A. Quintela, C. Jáuregui, J. Echevarría and J.M. López-Higuera "Embedded temperature-strain fibre Bragg grating sensor system validation for concrete structures," Journal of Optics A: Pure and Applied Optics, **4**, S387-S389, 2002.

[76] B. Gwandu, L. Zhang, K. Chisholm, Y. Liu and I. Bennion, "Compact FBG grating array structure for high spatial resolution distributed strain sensing," *OFS2000*, Venice, Italy, 11-13 October, 2000.

[77] S. Magne, S. Rougeault, M. Vilela and P. Ferdinand "State-of-strain evaluation with fiber Bragg grating rosettes: application to discrimination between strain and temperature effects in fiber sensors," Applied Optics, **36**(36), 9437-9447, 1997.

[78] K.T.V Grattan and T. Sun, "Fiber optic sensor technology: an overview," Sensors and Actuators, **82**, 40-61, 2000.

[79] K. Wood, T. Brown, R. Rogowski and B. Jensen, "Fiber optic sensors for health monitoring of morphing airframes: I. Bragg grating strain and temperature sensor," Smart Materials and Structures, **9**, 163-169, 2000.

[80] G. Wang, K. Pran, G. Sagvolden, G.B. Havsgard, A.E. Jensen, G.A. Johnson and S.T. Vohra, "Ship hull structure monitoring using fibre optic sensors," Smart Materials and Structures, **10**(3), 472-478, 2001.

[81] P. Peng, H. Tseng and S. Chi, "A Novel Fiber-Laser-Based Sensor Network With Self-Healing Function," IEEE Photonics Technology Letters, **15**(2), 275-277, 2003.

[82] A. Asseh, H. Storøy, B.E. Sahlgren, S. Sandgren and R.A.H. Stubbe, "A Writing Technique for Long Fiber Bragg Gratings with Complex Reflectivity Profiles," IEEE Journal of Lightwave Technology, **15**(8), 1419-1423, 1997.

[83] A.D. Kersey, et al, "Fiber grating sensors," IEEE Journal of Lightwave Technology, **15**, 1442-1463, 1997.

[84] E. Hect, "Optics" 4th Edition, Eugene Hect, Addison Wesley, 2003, p.314

[85] W.B. Jones, Introduction to Optical Fiber Communication Systems, 1st Edition, Holt, Rinehart and Winston Inc, 1988, p.112-114